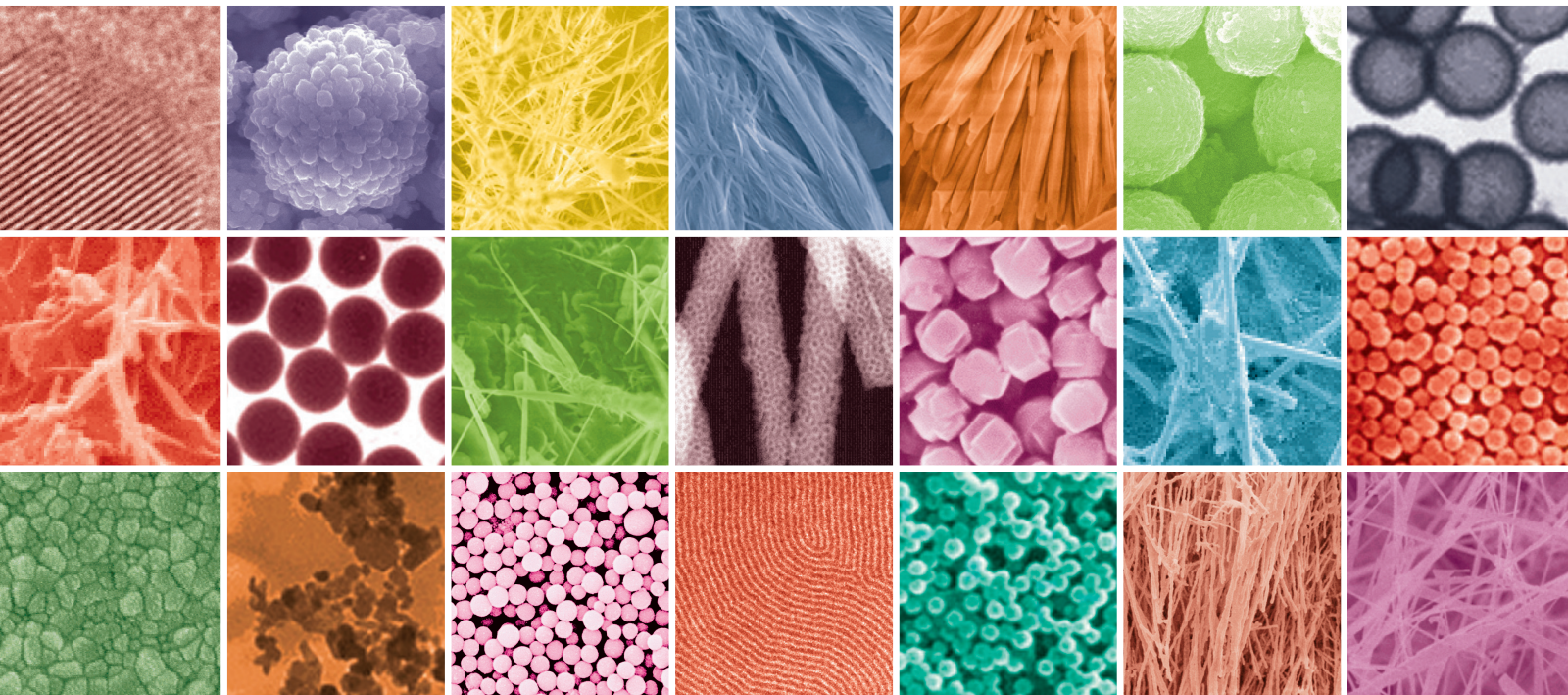


1D Nanostructures: Controlled Fabrication and Energy Applications

Guest Editors: Jian Wei, Xuchun Song, Chunli Yang, and Michael Z. Hu





1D Nanostructures: Controlled Fabrication and Energy Applications

1D Nanostructures: Controlled Fabrication and Energy Applications

Guest Editors: Jian Wei, Xuchun Song, Chunli Yang,
and Michael Z. Hu



Copyright © 2013 Hindawi Publishing Corporation. All rights reserved.

This is a special issue published in "Journal of Nanomaterials." All articles are open access articles distributed under the Creative Commons Attribution License, which permits unrestricted use, distribution, and reproduction in any medium, provided the original work is properly cited.

Editorial Board

- Katerina E. Aifantis, Greece
Nageh K. Allam, USA
Margarida Amaral, Portugal
Xuedong Bai, China
Lavinia Balan, France
Enrico Bergamaschi, Italy
Theodorian Borca-Tasciuc, USA
C. Jeffrey Brinker, USA
Christian Brosseau, France
Xuebo Cao, China
Shafiq Chowdhury, USA
Kwang-Leong Choy, UK
Cui ChunXiang, China
Miguel A. Correa-Duarte, Spain
Shadi A. Dayeh, USA
Claude Estournès, France
Alan Fuchs, USA
Lian Gao, China
Russell E. Gorga, USA
Hongchen Chen Gu, China
Mustafa O. Guler, Turkey
John Zhanhu Guo, USA
Smrati Gupta, Germany
Michael Harris, USA
Zhongkui Hong, China
Michael Z. Hu, USA
David Hui, USA
Y.-K. Jeong, Republic of Korea
Sheng-Rui Jian, Taiwan
Wanqin Jin, China
Rakesh K. Joshi, UK
Zhenhui Kang, China
Fathallah Karimzadeh, Iran
Alireza Khataee, Iran
- Do Kyung Kim, Korea
Alan K. T. Lau, Hong Kong
Burtrand Lee, USA
Jun Li, Singapore
Benxia Li, China
Xing-Jie Liang, China
Shijun Liao, China
Gong Ru Lin, Taiwan
J.-Y. Liu, USA
Tianxi Liu, China
Jue Lu, USA
Songwei Lu, USA
Daniel Lu, China
Ed Ma, USA
Gaurav Mago, USA
Santanu K. Maiti, India
Sanjay R. Mathur, Germany
Vikas Mittal, UAE
Weihai Ni, Germany
Sherine Obare, USA
Atsuto Okamoto, Japan
Abdelwahab Omri, Canada
Edward Andrew Payzant, USA
Kui-Qing Peng, China
Anukorn Phuruangrat, Thailand
Suprakas Sinha Ray, South Africa
Ugur Serincan, Turkey
Huaiyu Shao, Japan
Donglu Shi, USA
Vladimir Sivakov, Germany
Marinella Striccoli, Italy
Bohua Sun, South Africa
Saikat Talapatra, USA
Nairong Tao, China
- Titipun Thongtem, Thailand
Somchai Thongtem, Thailand
Alexander Tolmachev, Ukraine
Valeri P. Tolstoy, Russia
Tsung-Yen Tsai, Taiwan
Takuya Tsuzuki, Australia
Raquel Verdejo, Spain
Mat U. Wahit, Malaysia
Zhenbo Wang, China
Ruiping Wang, Canada
Shiren Wang, USA
Cheng Wang, China
Yong Wang, USA
Jinquan Wei, China
Ching-Ping Wong, Hong Kong
Xingcai Wu, China
Guodong Xia, Hong Kong
Zhi Li Xiao, USA
Ping Xiao, UK
Yangchuan Xing, USA
Shuangxi Xing, China
N. Xu, China
Doron Yadlovker, Israel
Yingkui Yang, China
Khaled Youssef, USA
Kui Yu, Canada
William W. Yu, USA
Haibo Zeng, China
Tianyou Zhai, Japan
Renyun Zhang, Sweden
Bin Zhang, China
Yanbao Zhao, China
Lianxi Zheng, Singapore
Chunyi Zhi, Hong Kong

Contents

ID Nanostructures: Controlled Fabrication and Energy Applications, Jian Wei, Xuchun Song, Chunli Yang, and Michael Z. Hu
Volume 2013, Article ID 674643, 2 pages

One-Step Fabrication of Hierarchically Structured Silicon Surfaces and Modification of Their Morphologies Using Sacrificial Layers, Seong J. Cho, Se Yeong Seok, Jin Young Kim, Geunbae Lim, and Hoon Lim
Volume 2013, Article ID 289256, 8 pages

Rapid and Efficient Synthesis of Silver Nanofluid Using Electrical Discharge Machining, Kuo-Hsiung Tseng, Heng-Lin Lee, Chih-Yu Liao, Kuan-Chih Chen, and Hong-Shiou Lin
Volume 2013, Article ID 174939, 6 pages

Improved Antireflection Properties of an Optical Film Surface with Mixing Conical Subwavelength Structures, Chi-Feng Chen, Yu-Cheng Cheng, and Chia-Jen Ting
Volume 2013, Article ID 459325, 5 pages

Densely Packed Linear Assemblies of Carbon Nanotube Bundles in Polysiloxane-Based Nanocomposite Films, Hong-Baek Cho, Minh Triet Tan Huynh, Tadachika Nakayama, Son Thanh Nguyen, Hisayuki Suematsu, Tsuneo Suzuki, Weihua Jiang, Satoshi Tanaka, Yoshinori Tokoi, Soo Wahn Lee, Tohoru Sekino, and Koichi Niihara
Volume 2013, Article ID 564307, 10 pages

UV-Ozone Treatment on Cs_2CO_3 Interfacial Layer for the Improvement of Inverted Polymer Solar Cells, Yusheng Xin, Zixuan Wang, Lu Xu, Xiaowei Xu, Yang Liu, and Fujun Zhang
Volume 2013, Article ID 104825, 6 pages

Annealing Effect on Photovoltaic Performance of CdSe Quantum-Dots-Sensitized TiO_2 Nanorod Solar Cells, Yitan Li, Lin Wei, Ruizi Zhang, Yanxue Chen, and Jun Jiao
Volume 2012, Article ID 103417, 6 pages

Preparation and Characterization of Alumina Nanoparticles in Deionized Water Using Laser Ablation Technique, Veeradate Piriya Wong, Voranuch Thongpool, Piyapong Asanithi, and Pichet Limsuwan
Volume 2012, Article ID 819403, 6 pages

Editorial

1D Nanostructures: Controlled Fabrication and Energy Applications

Jian Wei,¹ Xuchun Song,² Chunli Yang,¹ and Michael Z. Hu³

¹ College of Materials and Mineral Resources, Xi'an University of Architecture and Technology, Xi'an 710055, China

² Department of Chemistry, Fujian Normal University, Fuzhou 350007, China

³ Energy and Transportation Science Division, Oak Ridge National Laboratory, Oak Ridge, TN 37831, USA

Correspondence should be addressed to Jian Wei; weijian@xauat.edu.cn

Received 25 September 2013; Accepted 25 September 2013

Copyright © 2013 Jian Wei et al. This is an open access article distributed under the Creative Commons Attribution License, which permits unrestricted use, distribution, and reproduction in any medium, provided the original work is properly cited.

One-dimensional (1D) nanostructures possess fascinating physical properties determined by their special shapes and structures and have wide applications in solar energy conversion, thermoelectric devices, energy storage technology, and so forth. To deal with the rising energy and environmental problems, considerable research has been stimulated on preparation technologies of novel 1D nanostructures and exploring their energy applications. The latest progress, including controlled fabrication methods, characterization, composite structure, and ways to enhance the efficiency of energy conversion, needs to be summarized and ideas exchanged need to be in the entire community to accelerate the development of 1D nanostructures.

A total of 7 articles are presented in this current special issue. The issue focuses on the latest progress in fabrication techniques and properties of energy saving and converting of 1D nanomaterials. In addition, nanofluid, antireflection coating, polymer solar cell, and nanoparticle are also reported in this issue.

1D nanomaterials are addressed in three manuscripts. S. J. Cho et al. report a novel one-step process to fabricate patternable hierarchical structures consisting of microstructures and one-dimensional nanostructures using a sacrificial layer. Using their method, they fabricated patterned hierarchical structures with the ability to control the shape and density of the nanostructure. H.-B. Cho et al. report the linear assemblies of carbon nanotubes (CNTs) fabricated by applying DC and switching DC electric fields in polysiloxane-based nanocomposite films. The assembly structure enhances the thermal and electrical conductivities and the optical

transmittance of the polysiloxane/CNTs nanocomposites. Single-crystalline TiO₂ nanorod arrays decorated with CdSe quantum dots were synthesized by Y. Li and his coworkers. A significant improvement of the photovoltaic performance for quantum-dots-sensitized solar cell based on the CdSe-TiO₂ nanostructure was obtained in their work.

Inverted configuration polymer solar cells (IPSCs) were prepared by Y. Xin et al., using Cs₂CO₃ modified indium tin oxide substrates as cathode and MoO₃/Al as anode. The power conversion efficiency of IPSCs was improved to 1% when the interfacial Cs₂CO₃ layers were conducted with 15-minute UV-ozone treatment.

C.-F. Chen et al. used the finite difference time domain method to analyze the antireflection effect of subwavelength structure in a spectral range from 400 nm to 800 nm. It is found that the antireflection function has obviously decreased in different ratios of the added small conical structures. Such antireflection pattern is useful for solar cells, photodetectors, LEDs, and high-end imaging lens.

Two manuscripts deal with the nanofluid and Al₂O₃ nanoparticles, respectively. In one paper, silver nanofluid was prepared by electrical discharge machining system. The relationship of process parameters to the material removal rate of silver electrode and silver ion output rate in the fluid was also quantified. In another one, V. Piriya-wong et al. reported the preparation of Al₂O₃ nanoparticles by laser ablation of an aluminum target in deionized water.

We are much honored to be invited to compile this special issue and pleased to see the latest progress of fabrication and energy applications of 1D nanomaterials and their relative

research fields. We believe that these papers will promote development of 1D nanomaterials and enrich our understanding of the relative key scientific problems.

Acknowledgments

The editors thank the authors as well as the reviewers for their constructive contributions and efforts in the prepared process of this special issue.

*Jian Wei
Xuchun Song
Chunli Yang
Michael Z. Hu*

Research Article

One-Step Fabrication of Hierarchically Structured Silicon Surfaces and Modification of Their Morphologies Using Sacrificial Layers

Seong J. Cho,¹ Se Yeong Seok,¹ Jin Young Kim,¹ Geunbae Lim,^{1,2} and Hoon Lim³

¹ Department of Mechanical Engineering, Pohang University of Science and Technology (POSTECH), Pohang 790-784, Republic of Korea

² Department of Integrative Bioscience and Biotechnology, Pohang University of Science and Technology (POSTECH), Pohang 790-784, Republic of Korea

³ Department of Emergency Medicine, Soon Chun Hyang University Hospital, Bucheon 420-767, Republic of Korea

Correspondence should be addressed to Geunbae Lim; lilmems@postech.ac.kr and Hoon Lim; 43210@schmc.ac.kr

Received 3 December 2012; Revised 29 May 2013; Accepted 8 June 2013

Academic Editor: Jian Wei

Copyright © 2013 Seong J. Cho et al. This is an open access article distributed under the Creative Commons Attribution License, which permits unrestricted use, distribution, and reproduction in any medium, provided the original work is properly cited.

Fabrication of one-dimensional nanostructures is a key issue for optical devices, fluidic devices, and solar cells because of their unique functionalities such as antireflection and superhydrophobicity. Here, we report a novel one-step process to fabricate patternable hierarchical structures consisting of microstructures and one-dimensional nanostructures using a sacrificial layer. The layer plays a role as not only a micromask for producing microstructures but also as a nanomask for nanostructures according to the etching time. Using this method, we fabricated patterned hierarchical structures, with the ability to control the shape and density of the nanostructure. The various architectures provided unique functionalities. For example, our sacrificial-layer etching method allowed nanostructures denser than what would be attainable with conventional processes to form. The dense nanostructure resulted in a very low reflectance of the silicon surface (less than 1%). The nanostructured surface and hierarchically structured surface also exhibited excellent antiwetting properties, with a high contact angle ($>165^\circ$) and low sliding angle ($<1^\circ$). We believe that our fabrication approach will provide new insight into functional surfaces, such as those used for antiwetting and antireflection surface applications.

1. Introduction

One-dimensional nanostructures are of great interest because of their unique properties. Examples found in nature have high surface-to-volume ratios and can impart antireflective and superhydrophobic behaviors [1–4]. Many attempts have been made to incorporate such functional nanostructures into various devices such as optical devices, solar cells, sensors, and biomedical devices to improve their performance or to impart special attributes [5–12]. The special functionalities of the nanostructured surfaces are governed by their architectures. For example, a high-aspect ratio nanostructured silicon surface can generate a graded refractive index and thereby minimize reflectivity over a wide range of wavelengths [13]. Also, by controlling the scale of

a nanostructure, its surface reflectivity can be tuned while maintaining its superhydrophobic properties [5]. Making multiscale architectures is another key issue in the fabrication of functional nanostructures because their special geometries are crucial to their performance [14–17]. For example, the microstructures of a lotus leaf minimize contact area, and their nanostructures allow the surface to withstand very high pressures [14, 16]. However, in general, inefficient approaches, that is, those requiring two or more processes, are usually required to fabricate multiscale architectures.

We report here a simple, one-step fabrication method for multiscale silicon structures and the control of nanostructure morphology using a sacrificial layer. The patterned sacrificial layer protects the etching of silicon, resulting in the production of a micropattern early in the etching

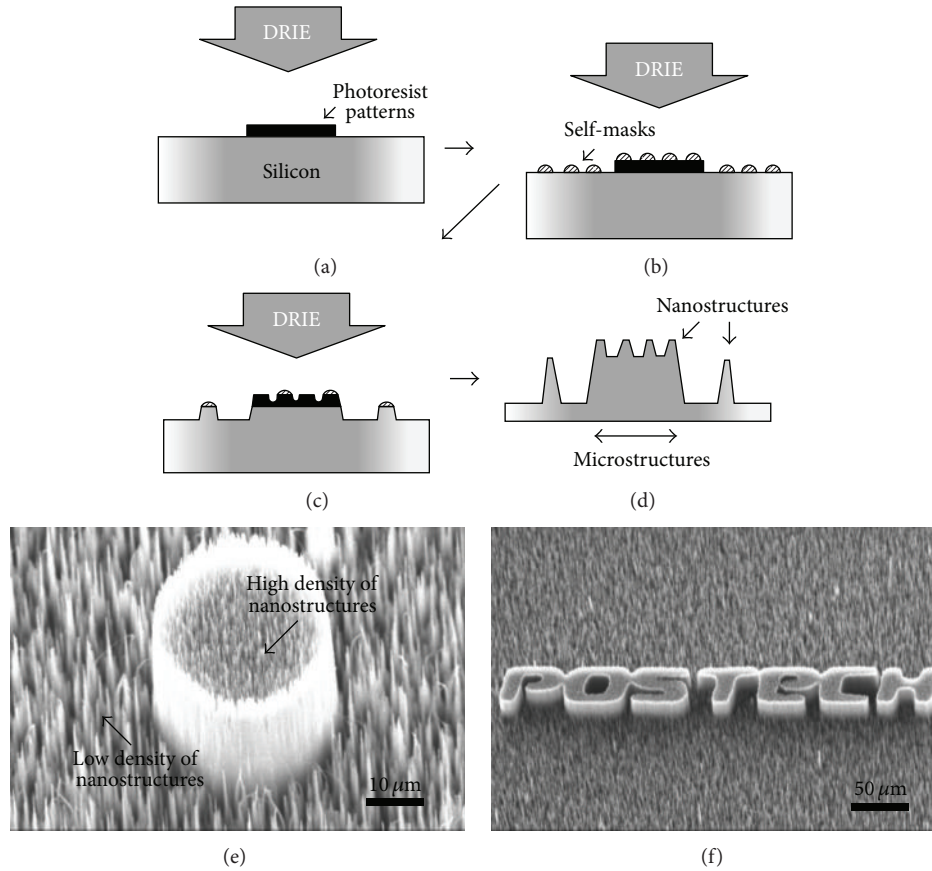


FIGURE 1: ((a)–(d)) Fabrication of patternable hierarchically structured silicon surfaces, using deep reactive-ion etching (DRIE) based on the “black silicon” method and using a sacrificial layer. ((e), (f)) Scanning electron microscopy (SEM) images of the hierarchical structures.

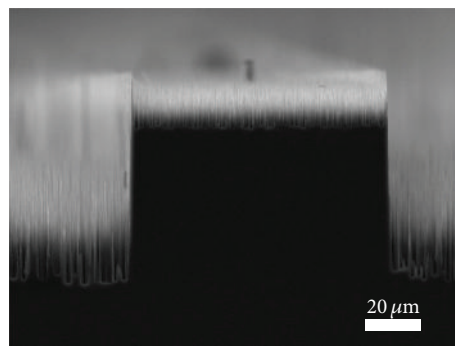


FIGURE 2: Cross-sectional SEM image of the hierarchical silicon structure.

process, whereas residue from the sacrificial layer, remaining after the final etching process, acts as a nanomask which produces the nanostructure. To verify the nanostructure formation, we analyzed the etching process morphologically and chemically using high-resolution scanning electron microscopy (HR-SEM) and energy dispersive spectrometry (EDS), respectively. Based on the method, we fabricated patternable hierarchical structures and controlled the shape

and density of the nanostructure. In particular, a high-density nanostructure, six times denser than that produced using conventional procedures, had excellent antireflection properties (specular reflectance: average ca. 0.1%; hemispherical reflectance: average ca. 1%) over a broad range of wavelengths, compared with a polished silicon surface (specular reflectance: ~40%; hemispherical reflectance: ~50%). The nanostructured surface and micropatterned surface also

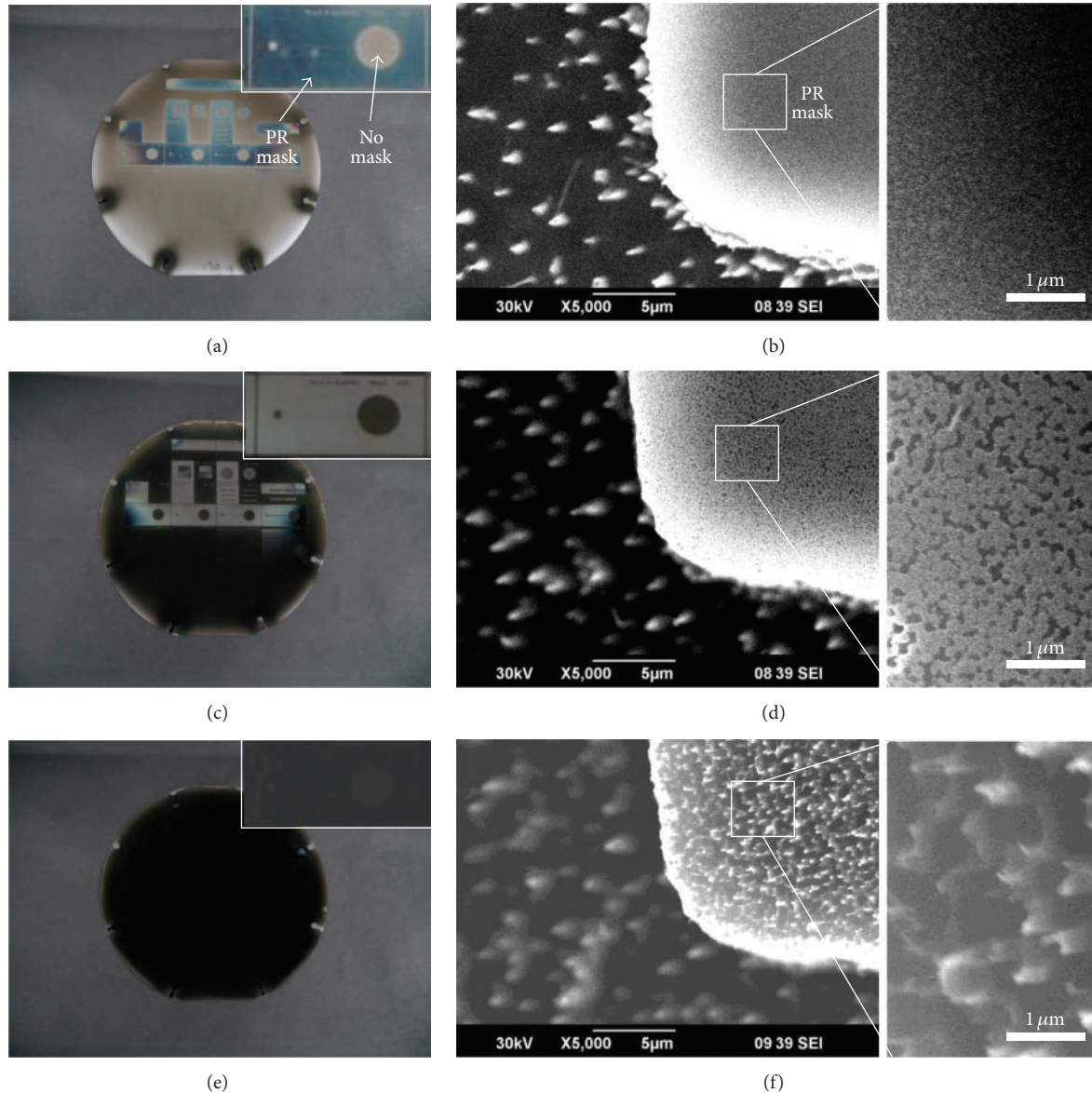


FIGURE 3: Optical images of nanostructured surfaces at various DRIE processing times: (a) 3000 s, (c) 4000 s, and (e) 5000 s. (b), (d), and (f) are SEM images and magnified images of (a), (c), and (e), respectively.

exhibited stable antiwetting properties, with a high contact angle ($>165^\circ$) and low sliding angle ($<1^\circ$), which provided special functionality, such as self-cleaning.

2. Experimental Section

Figures 1(a)–1(d) illustrate the etching process using a sacrificial layer and shows SEM images of each step. First, cleaned and polished 4 in silicon wafers were prepared (P-type $\langle 100 \rangle$), and photoresist (PR) (AZ 1512) patterns were fabricated on a silicon wafer as a sacrificial layer using the common photolithography process. Then, the wafer was etched by a deep reactive-ion etching (DRIE) process based on the “black silicon” method [5, 18–20]. During the black silicon process, micro-self-masks formed automatically on the silicon

surface. The silicon surface was then anisotropically etched to form needle-shaped nanostructures called nanograss [5]. Detailed procedures are as follows: the prepared wafers were subjected to a pulsed etching process by an inductively coupled plasma multiplex system that used alternate cycles of etching and passivation (Surface Technology Systems, Ltd., UK). In the etching cycle, sulfur hexafluoride (SF_6) and oxygen (O_2) gases flowed at 130 sccm and 13 sccm, respectively. In the passivation cycle, the octafluorocyclobutane (C_4F_8) gas flow rate was 85 sccm. Coil power and platen power were 600 W and 30 W, respectively. Switching times for the etching and passivation cycles were 6 s and 4 s, respectively. The bias voltage was 120 V and 0 V for etching and passivation, respectively. Under these conditions, sparse nanograss having high aspect ratios (width: 50–3000 nm and

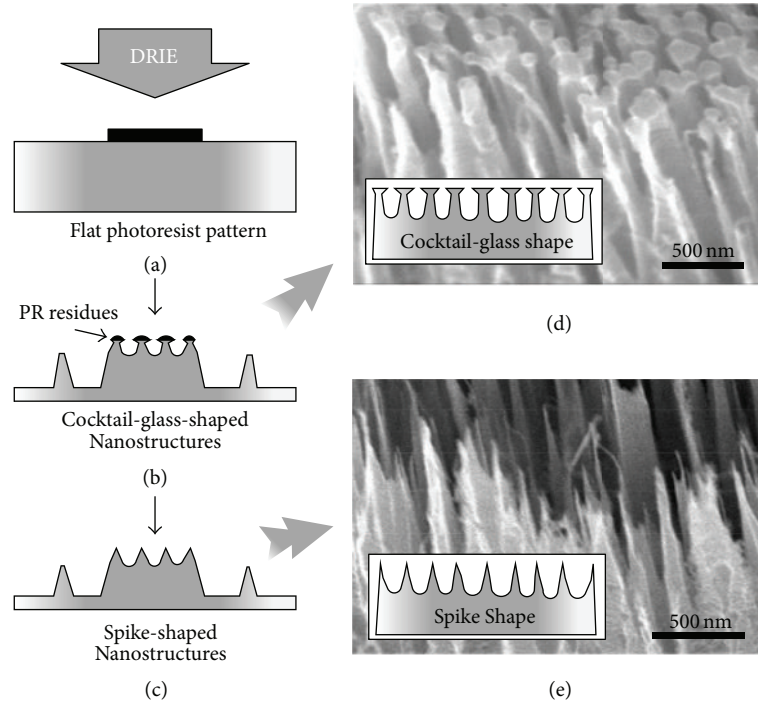


FIGURE 4: ((a)–(c)) The morphology of nanostructures was controlled by depositing a sacrificial layer and varying the process time. (d) Cocktail-glass-shaped nanostructures. (e) Spike-shaped nanostructures.

length: $0.1\text{--}50\ \mu\text{m}$) formed. As the process time lengthened, the PR mask (thickness: $1.2\ \mu\text{m}$) was etched and additional nanoglass formed.

SEM measurements were carried out with a field-emission- (FE-) SEM instrument (SU-6600, Hitachi, Japan). Elemental composition of the nanostructure was analyzed using a Hitachi energy dispersive X-ray analysis (EDAX) energy spectra analyzer. Optical reflectance measurements of the nanostructured surface were conducted using an ultraviolet-visible-infrared (UV-Vis-IR) spectrophotometer (Cary 5000, Varian, USA), equipped with absolute specular and hemispherical reflectance accessories. Reflectance was measured from the UV range (wavelength: $200\ \text{nm}$) to the near-IR range ($1000\ \text{nm}$) to examine the effect of silicon nanostructures on broadband reflectance. Contact angles (CAs) were measured between $5\ \mu\text{L}$ deionized water droplets and the nanostructured surface, using a drop shape analysis system (DSA 100, Kruss, Germany) with the sessile drop method.

3. Results and Discussion

Patternable hierarchical silicon nanoglass was fabricated using the black silicon process with PR patterns as a sacrificial layer, as shown in Figures 1(e) and 1(f). The patterned PR protected the silicon surface during the early stage DRIE process because of its high selectivity over silicon (~ 50) so that the microstructures produced would have the patterned shape. After long etching times (ca. $4000\ \text{s}$ for a thickness of $1.2\ \mu\text{m}$ PR), the bare silicon was slightly etched to expose the bare

silicon surface under the PR layer. At that time, nanoglass began to form on the microstructure. The nanoglass on the microstructure was denser than that on the unmasked surfaces. This phenomenon will be discussed later. Finally, patternable multiscale silicon structures were fabricated by the one-step etching process (etching time: $5000\ \text{s}$). The height of the microstructure was about $57\ \mu\text{m}$, and the height of the nanostructure on the microstructure was about $15\ \mu\text{m}$ (Figure 2). The height of each structure could be controlled by the PR thickness and the etching time. A complex-shaped hierarchical structure was also fabricated (Figure 1(f)).

The shape of the nanoglass on the microstructure changed as the etching process time increased, unlike that of the general nanoglass structure. Figure 3 shows the shape changes that occurred on the silicon surface during the process. Just after the PR layer was removed (process time: ca. $4000\ \text{s}$), partial etching of the silicon began, as evidenced by the formation of fine holes having a diameter of ca. $100\ \text{nm}$ (Figure 3(d)). According to the cross-sectional view, as shown in Figures 4(d) and 4(e), the surface was etched in the form of a cocktail glass. This unique shape and the hierarchical structure are similar to those of gecko foot hair, which has a dry adhesive property (Figure 3(e)) [21, 22]. As the etching time increased, the tips of the silicon nanoglass changed from the cocktail-glass shape to very sharp spikes (tip width: $<10\ \text{nm}$), and the color of the surface turned from silver to black (Figures 3(a), 3(c), and 3(e)).

We assumed that the formation of this unique shape was due to residual PR (Figure 3(d)). This shape formed because intact PR prevented etching of the underlying silicon layer. Because of PR's nonreactive property to etching gas in the

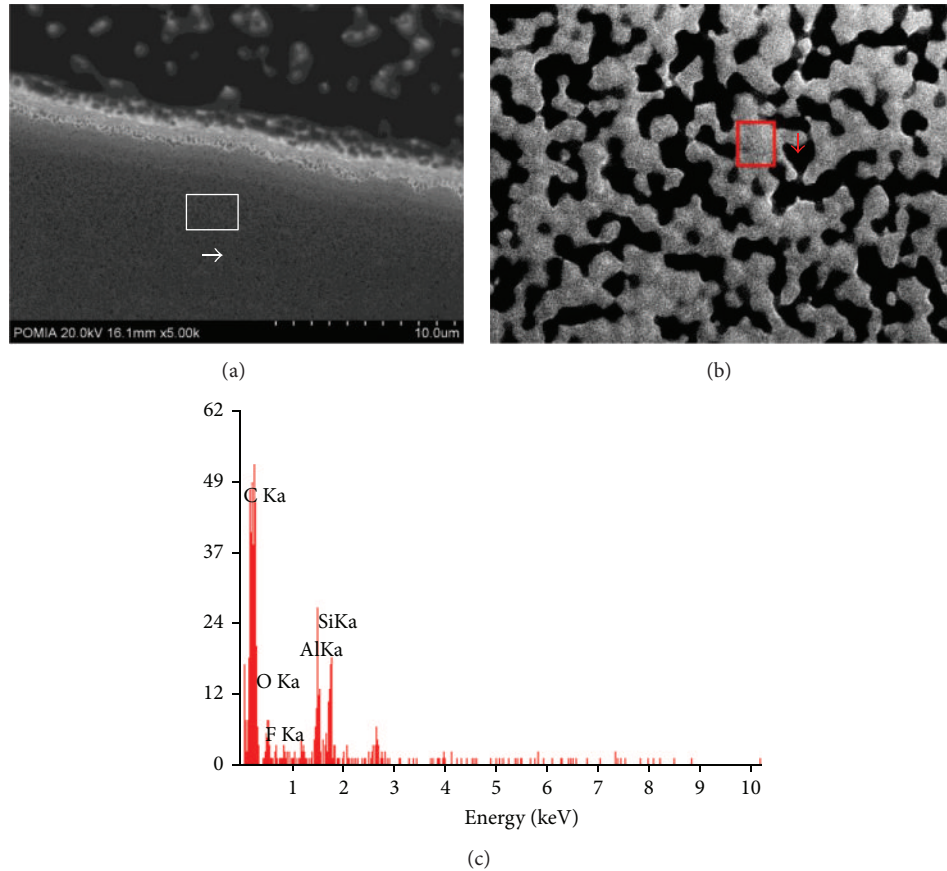


FIGURE 5: Energy dispersive spectrometry (EDS) analysis of the nanostructured surface fabricated by a sacrificial layer. (a) SEM image of the patterned hierarchical structure. (b) Magnified image of the high-density nanostructure on a micropatterned architecture in the early etching state. (c) EDS spectrum of the PR residue on the cocktail-glass-shaped nanostructures.

DRIE process, the PR residues could protect the silicon for a relatively long time to form such a cocktail-glass-shaped structure. To confirm the residual PR on silicon, we analyzed the composition of the cocktail-glass-shaped structure using EDS (Figure 5). As a result, carbon, which is the main element of PR but not present in silicon, existed on the surface of the etched structure.

The residual PR affected not only the shape of the silicon structure but also its density. The density difference can also be explained using a similar formation mechanism as that of the cocktail-glass-shaped structure. Conventional nanograss was formed by nonuniform etching of a thin passivation layer during the plasma etching process. Regarding the nanograss produced using our sacrificial-layer approach, the nonetched residual PR enhanced the passivation process, because it was more solid and thicker than the fluorocarbon polymer that was used as a passivation layer for the conventional plasma etching process. Thus, denser nanomasks could be formed on silicon to increase the density of the nanograss. Consequently, the nanograss density could be modified using a sacrificial layer. Hierarchical structures with various densities were fabricated using this process. Figure 6 shows two kinds of hierarchical structures, one with a high density for the nanostructure (Figure 6(a), nanostructure density:

$19.8 \times 10^7 \text{ cm}^{-2}$) and the other with a low density for the nanostructure (Figure 6(b), $2.9 \times 10^7 \text{ cm}^{-2}$). The high-density nanostructures were fabricated using our sacrificial-layer method. The low-density structure could be easily fabricated: microstructures were made using a PR pattern, and then the PR layer was removed with O_2 plasma (10 min); the nanograss formed on the cleaned microstructure. This suggests that residual PR was responsible for the nanograss density.

The marked difference in densities influenced the optical properties of the nanostructure. In general, the reflectance tendency of a subwavelength structure is determined by its refractive index profile [5]. The effective index of the subwavelength composite structure depends on its volume fraction and its intrinsic refractive index. Thus, the density of nanograss, which is related to both the volume fraction and the refractive index, played a crucial role in reflectance. Specifically, in the case of sparse nanograss (low density), a gradual increase in the refractive index profile was generated at the top and middle regions, due to its sharp, fine architecture; however, at the bottom, the index had changed dramatically due to the sparse architecture. The dense nanograss, on the other hand, generated a graded profile over the entire region due to the dense architecture. Figures 6(c) and 6(d) show how the specular and hemispherical reflectance

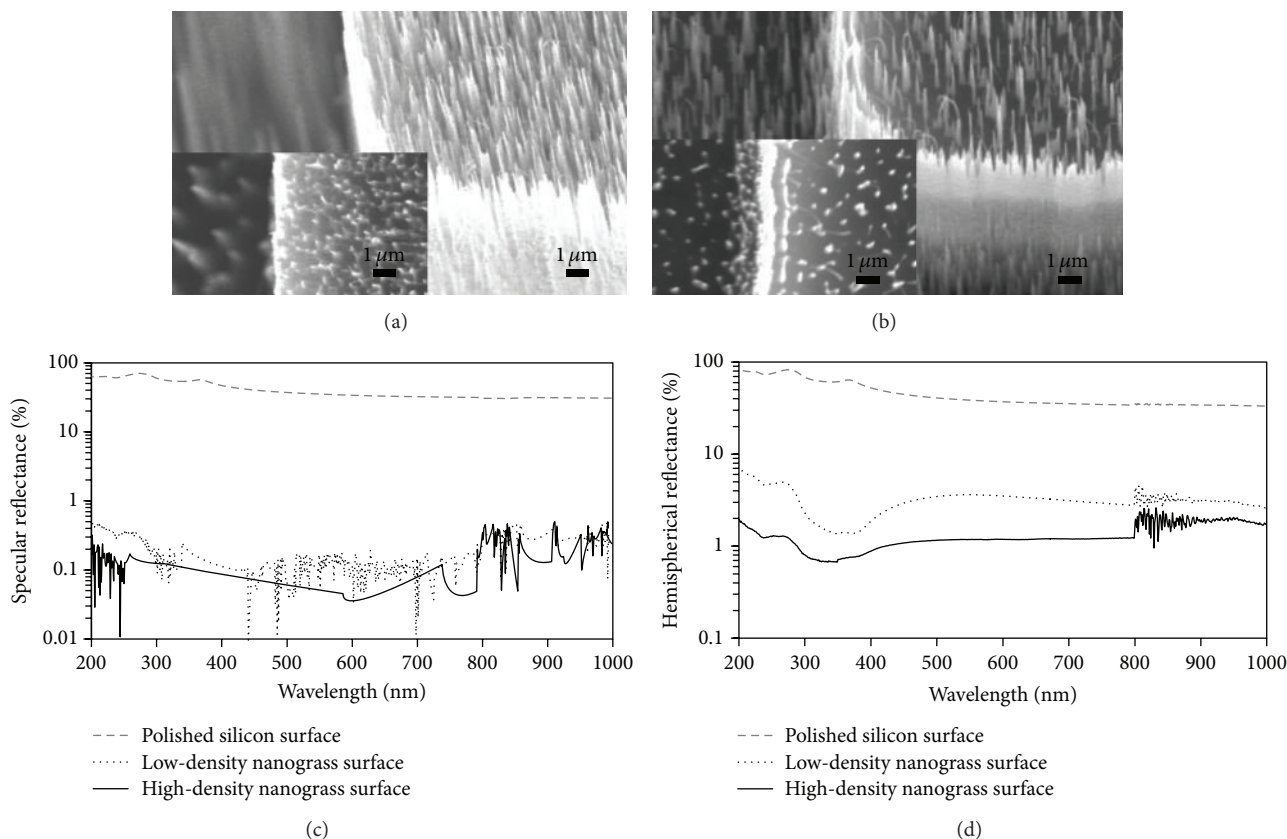


FIGURE 6: Control of the nanostructure density and measurement of optical properties. ((a), (b)) Hierarchical structures having high density and low density, respectively. ((c), (d)) Surface with antireflectivity over a broad wavelength region; the specular reflection and diffuse reflection are suppressed by the density of the nanostructure.

varied with the density of the nanostructure, respectively. The nanostructured silicon surface exhibited outstanding antireflectance compared with the polished silicon surface. In particular, the high-density nanograss surface provided excellent antireflective surfaces that possessed ca. 0.1% specular reflectance and ca. 1% hemispherical reflectance over the entire ultraviolet-visible-near infrared range (200–1000 nm). This reflectance is less than that for low-density nanograss surfaces (average specular reflectance of ca. 0.3% and average hemispherical reflectance of ca. 3%) and much lower than that for polished silicon (average of ca. 40%).

Fabrication of a hierarchical structure has been one of the main issues in antiwettability surface research. The antiwettability, which is often referred to as superhydrophobicity, can be achieved by low-energy chemical compositions and geometric micro- and nanostructured surfaces. To produce an antiwetting surface, we fabricated the nanostructured surface and hierarchical structure using our sacrificial-layer process. The surfaces were deposited with a low surface energy fluorocarbon polymer layer by a plasma-polymerized fluorocarbon coating (PPFC), using the same system as the DRIE process. Figure 7 shows the wettability of a high-density nanograss surface and a micro/nanohierarchically structured surface with a 5 μL sessile water drop. As a result, the surface exhibited excellent superhydrophobicity with

a high water contact angle (CA) and low sliding angle (SA). The high-density nanograss had a static CA of 165° and SA of <1°. The micro/nanohierarchically structured surface showed more outstanding antiwetting properties (CA ~ 170° and SA < 1°). The air gap between the drop and the surface (white arrow in the Figure 7) was observed optically. The air gap provides strong evidence for the formation of a stable, superhydrophobic surface with a Cassie state, in which a liquid droplet rests on a composite surface composed of a solid and trapped air.

4. Conclusion

We have demonstrated a novel process for the fabrication of patternable hierarchical structures that are a combination of a microstructure and a one-dimensional nanostructure. The morphologies of these structures have been modified using a PR sacrificial layer. A micropatterned hierarchical structure having a complex shape could be fabricated by a one-step process without invoking a nanopatterning process. The nanostructure can be controlled to have a cocktail-glass shape that resembled a gecko's foot hair or sharp spike shape having a high-aspect ratio. Our sacrificial-layer etching method allows denser nanostructures to form than would be attainable with existing processes. The dense nanostructure

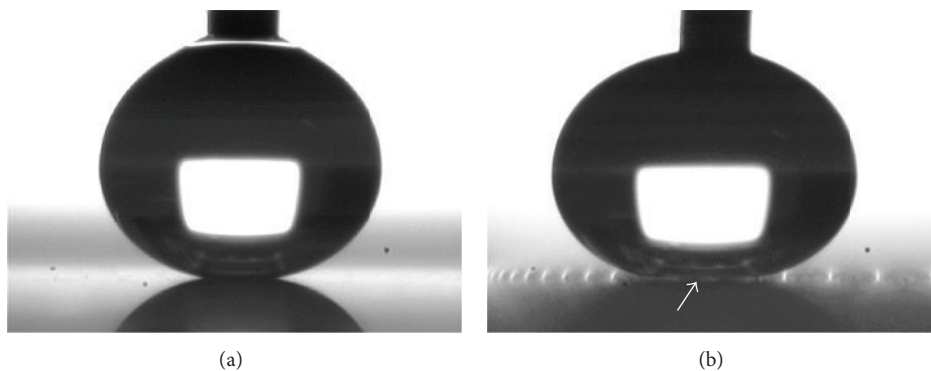


FIGURE 7: (a) Antiwettability test of the high-density nanograss surface with a $5\ \mu\text{L}$ sessile water drop (static water contact angle = 165° and sliding angle $<1^\circ$). (b) Antiwettability test of a micro/nanohierarchically structured surface (static water contact angle = 170° and sliding angle $<1^\circ$). The air gap between the drop and the surface (white arrow) was observed optically, due to the hierarchical surface's superior antiwettability.

resulted in a very low reflectance of the silicon surface, less than 1%. The nanostructured surface and hierarchically structured surface also exhibited excellent antiwetting properties. We believe our fabrication method can be utilized to prepare various functional surfaces, such as antireflecting surfaces for high-performance optical devices (e.g., solar cells) and self-cleaning, superhydrophobic surfaces.

Conflict of Interests

The authors declare no financial conflict of interests.

Acknowledgments

This research was financially supported by a grant to MEMS Research Center for National Defense funded by Defense Acquisition Program Administration.

References

- [1] Y. Li, J. Zhang, and B. Yang, "Antireflective surfaces based on biomimetic nanopillared arrays," *Nano Today*, vol. 5, no. 2, pp. 117–127, 2010.
- [2] Y.-F. Huang, S. Chattopadhyay, Y.-J. Jen et al., "Improved broadband and quasi-omnidirectional anti-reflection properties with biomimetic silicon nanostructures," *Nature Nanotechnology*, vol. 2, no. 12, pp. 770–774, 2007.
- [3] C. Dorrer and J. R uhe, "Wetting of silicon nanograss: from superhydrophilic to superhydrophobic surfaces," *Advanced Materials*, vol. 20, no. 1, pp. 159–163, 2008.
- [4] K. T. Lee and J. Cho, "Roles of nanosize in lithium reactive nanomaterials for lithium ion batteries," *Nano Today*, vol. 6, no. 1, pp. 28–41, 2011.
- [5] S. J. Cho, T. An, J. Y. Kim, J. Sung, and G. Lim, "Superhydrophobic nanostructured silicon surfaces with controllable broadband reflectance," *Chemical Communications*, vol. 47, no. 21, pp. 6108–6110, 2011.
- [6] K. Q. Peng and S. T. Lee, "Silicon nanowires for photovoltaic solar energy conversion," *Advanced Materials*, vol. 23, no. 2, pp. 198–215, 2011.
- [7] Z. Fan, H. Razavi, J.-W. Do et al., "Three-dimensional nanopillar-array photovoltaics on low-cost and flexible substrates," *Nature Materials*, vol. 8, no. 8, pp. 648–653, 2009.
- [8] T. An, W. Choi, E. Lee, I. T. Kim, W. Moon, and G. Lim, "Fabrication of functional micro- and nanoneedle electrodes using a carbon nanotube template and electrodeposition," *Nanoscale Research Letters*, vol. 6, article 306, 2011.
- [9] W. Choi, T. An, and G. Lim, "Organic electrochemical transistors based on a dielectrophoretically aligned nanowire array," *Nanoscale Research Letters*, vol. 6, article 339, 2011.
- [10] T. An, W. Choi, S. W. Joo, and G. Lim, "A novel fabrication method of CNT-CP composite single nanowires self-templated by dielectrophoresis and electropolymerization," *Physica Status Solidi (RRL)*, vol. 5, no. 7, pp. 235–237, 2011.
- [11] S. J. Cho, B. Kim, T. An, and G. Lim, "Replicable multilayered nanofibrous patterns on a flexible film," *Langmuir*, vol. 26, no. 18, pp. 14395–14399, 2010.
- [12] S. J. Cho, H. Nam, T. An, and G. Lim, "Replicable and shape-controllable fabrication of electrospun fibrous scaffolds for tissue engineering," *Journal of Nanoscience and Nanotechnology*, vol. 12, no. 12, pp. 9047–9050, 2012.
- [13] S. Chattopadhyay, Y. F. Huang, Y. J. Jen, A. Ganguly, K. H. Chen, and L. C. Chen, "Anti-reflecting and photonic nanostructures," *Materials Science and Engineering: R*, vol. 69, pp. 1–35, 2010.
- [14] Y. Su, B. Ji, K. Zhang, H. Gao, Y. Huang, and K. Hwang, "Nano to micro structural hierarchy is crucial for stable superhydrophobic and water-repellent surfaces," *Langmuir*, vol. 26, no. 7, pp. 4984–4989, 2010.
- [15] Y. Xiu, L. Zhu, D. W. Hess, and C. P. Wong, "Hierarchical silicon etched structures for controlled hydrophobicity/ superhydrophobicity," *Nano Letters*, vol. 7, no. 11, pp. 3388–3393, 2007.
- [16] T. An, S. J. Cho, W. Choi, J. H. Kim, S. T. Lim, and G. Lim, "Preparation of stable superhydrophobic mesh with a biomimetic hierarchical structure," *Soft Matter*, vol. 7, no. 21, pp. 9867–9870, 2011.
- [17] S. J. Cho, H. Nam, H. Ryu, and G. Lim, "A rubberlike stretchable fibrous membrane with anti-wettability and gas breathability," *Advanced Functional Materials*, 2013.
- [18] H. Jansen, M. de Boer, R. Legtenberg, and M. Elwenspoek, "The black silicon method: a universal method for determining the parameter setting of a fluorine-based reactive ion etcher in deep silicon trench etching with profile control," *Journal of*

Micromechanics and Microengineering, vol. 5, no. 2, pp. 115–120, 1995.

- [19] M. Gharghi and S. Sivoththaman, “Formation of nanoscale columnar structures in silicon by a maskless reactive ion etching process,” *Journal of Vacuum Science and Technology A*, vol. 24, no. 3, pp. 723–727, 2006.
- [20] I. I. Amirov and N. V. Alov, “Formation of microstructures on silicon surface in a fluorinated plasma via the cyclic etching-passivation process,” *High Energy Chemistry*, vol. 42, no. 2, pp. 132–136, 2008.
- [21] H. E. Jeong, J. K. Lee, H. N. Kim, S. H. Moon, and K. Y. Suh, “A nontransferring dry adhesive with hierarchical polymer nanohairs,” *Proceedings of the National Academy of Sciences of the United States of America*, vol. 106, no. 14, pp. 5639–5644, 2009.
- [22] Z. L. Wang, “Nanomaterials: sticky but not messy,” *Nature Nanotechnology*, vol. 4, pp. 407–408, 2009.

Research Article

Rapid and Efficient Synthesis of Silver Nanofluid Using Electrical Discharge Machining

Kuo-Hsiung Tseng,¹ Heng-Lin Lee,¹ Chih-Yu Liao,^{1,2}
Kuan-Chih Chen,¹ and Hong-Shiou Lin¹

¹ Department of Electrical Engineering, National Taipei University of Technology, Taipei 10608, Taiwan

² Light Source Division, National Synchrotron Radiation Research Center, Hsinchu 30076, Taiwan

Correspondence should be addressed to Kuo-Hsiung Tseng; khtseng@ee.ntut.edu.tw

Received 5 January 2013; Accepted 31 March 2013

Academic Editor: Jian Wei

Copyright © 2013 Kuo-Hsiung Tseng et al. This is an open access article distributed under the Creative Commons Attribution License, which permits unrestricted use, distribution, and reproduction in any medium, provided the original work is properly cited.

The electrical discharge machining (EDM) system has been proven feasible as a rapid and efficient method for silver nanofluid preparation. This study prepared the silver nano-fluid via EDM and investigated the relationship between its process parameters and product characteristics. The prior study had found that the silver nano-fluid prepared by EDM contained both silver nanoparticles and silver ions. Silver ions had revealed the cause of the high suspension of the silver nanoparticles. To examine the relationship between the stability of silver nanofluid and the process parameters, this study quantified the relationship of process parameters to the material removal rate (MRR) of silver electrode and silver ion output rate (IOR) in the fluid, in order to achieve the most effective process parameter condition. Furthermore, the stability of silver nano-fluid was analyzed by various devices, including UV-Vis spectroscopy, size-distribution, and Zeta-potential analyzer. The effects of MRR, IOR, particle size, Zeta-potential, and optical properties of silver nanofluid under different process parameters are also discussed.

1. Introduction

Silver nanofluid has the potential for broad applications. The most typical application of nanosilver is its antibacterial effect, which has been proved to be able to inhibit various kinds of bacteria. Its commercial products can be widely seen on the market. Among the various methods to prepare silver nanofluid, this study employed the electrical discharge machining (EDM) system. The EDM system uses concentrated energy to sputter the electrode surface in dielectric fluid, and this method has been widely applied in nanofabrication technology, for example, Ni-C powders in pure ethanol [1], silver nanofluid in ethylene glycol [2], gold nanoparticles in water or ethanol [3], and carbon nanotubes [4]. The EDM method has already been discussed by Ichinose et al. [5], and furthermore, Tien et al. [6] discovered that the resultant silver nanofluid fabricated by EDM method not only contains silver nanoparticles but also ionic silver [7], both can apply in the sterilization, for example, *Staphylococcus*

aureus, and already tested by Tien et al. [8]. In addition, for commonly nanofluid applications, the thermal conductive material, like diamond nanofluid [9], Al₂O₃ [10], carbon nanotubes [11], TiO₂ [12], Cu [13], Ag [14], and so forth nanofluids, the thermal conductive properties had discussed, since the particle concentration is high and size in particle is low which results in good quality of thermal conductivity behavior [15]. For nanofluid application issue, nanofluid must be strongly stable which does not sediment before application or analysis, but many factors may affect the stability of suspension, such as concentration of particles, particle size in diameter, solution properties, electric conductivity, and pH [16]. These factors enhance complex interactions to the nanofluid, for example, Van Der Waals combination force, electrostatic Coulomb repulsion force both were discussed in colloidal science DLVO (Derjaguin, Landau, Verwey, and Overbeek) theorem [17–19].

Literatures provide many methods in analyzing the stability of nanofluid. This study utilized the intensity of absorption

TABLE 1: The key parameters of electrical discharge machining (EDM) for silver nanofluid production.

Parameters	Values
Dielectric fluid volume	200 mL (18.2 M Ω -cm)
Anode diameter	1 mm
Cathode diameter	2 mm
Electrodes: metallic silver rod	99.9%
Open circuit voltage	140 V
Arcing current	11.5 \pm 0.5 A
On-off duration	Variable: 5-5 to 1000-1000 μ s
Temperature	Room temperature (25 $^{\circ}$ C)
Fabrication process time	1, 2, 3 min
Pressure	1 atm

spectrum to determine the stability of nanoparticle suspension in the bottle and further analyzed whether the electric potential at the surface of nanoparticle reached the stable level by Zeta-potential analyzer. Moreover, the size-distribution meter was employed to determine whether the samples in the bottle would be concentrated and augmented with the time variation. In the EDM process, the concentration of particles and ions would rise as the time increased, and the relationship affecting the stability was the key point for this study. The primary factor of well-suspension nanofluid is the maintenance of Zeta-potential [20–22]. The Zeta-potential represents the Coulomb repulsion force which prevents the particles from aggregating or precipitating out of solution. However, many factors like the particle size, particle/ion concentration, and pH could affect Zeta-potential magnitude or maintenance [22, 23]. In this research, the EDM system was equipped with bulk silver rod (99.9%), after a minute process in water; the resultant silver nanofluid contains both silver nanoparticles and ionic silver. In this case of analysis, both concentrations of the silver nanoparticles concentration and ionic silver concentration raised will enhance aggregating phenomenon, which defines as unstable suspension nanofluid [24–26]. Therefore, to evaluate nanofluid stability fabricated by EDM, the ideal way is to show the decay slope of UV-absorbance intensity of every sample and compare the Zeta-potential and average size of nanofluid [27, 28].

2. Materials and Methods

2.1. Preparation of Silver Nanofluid. In this study, the silver nanofluid was fabricated by EDM system, as shown in Figure 1. The EDM system contains an anode and cathode, which are both 99.9% silver rod, submerged in DI water (200 mL). The anode and cathode are chosen specifically in different diameter, because the anode removal rate is greater than cathode around 50 times [29], and the smaller anode aligns the plasma column which maintains on the electrodes surface plate not on the edge. The power supply supplies 140 Volts pulse DC on electrodes; the average arcing distance between electrodes is around 30 μ m. The servo control system drives upper electrode (anode) to move down, that enables the electrons emitted from cathode to strike on anode surface

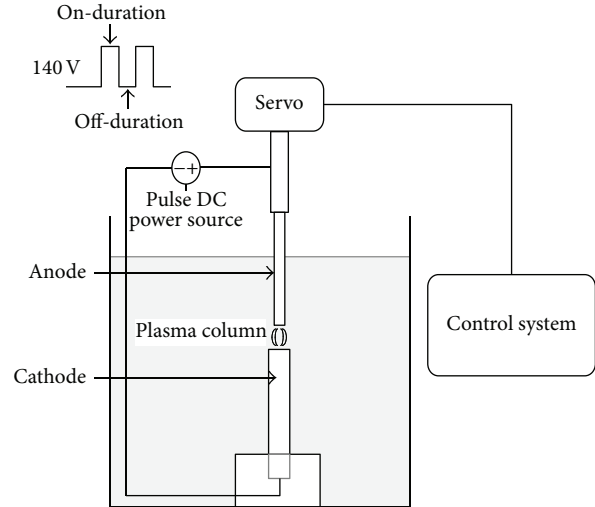


FIGURE 1: The scheme of electrical discharge machining (EDM) for silver nanofluid production.

continuously. Examination of the relationship between the characteristics of product and the process parameter (on-off duration) is the main purpose in this investigation. The detailed conditions are shown in Table 1.

2.2. Material Removal Rate (MRR) and Ion Output Rate (IOR). In electrical discharge machining processing, the arcing energy creates material removal rate (MRR, mg/sec) and ion output rate (IOR, ppm/sec), which are measured in different on-off time duration by electrode loss and titration (METTLER TOLEDO, DL50), respectively. MRR indicates measured anode loss after a significant process time (1 minute), because the main weight loss occurred on anode, and that the anode to cathode ratio is about 98:2 [29]; for this reason, we ignored the cathode loss while quantifying MRR. The relations between MRR and on-off time duration are nonlinear, which has been determined by [30, 31]. MRR and IOR are time dependent functions of EDM processing time.

2.3. Suspension Stability Test. After electrical discharge machining processing, the resultant silver nanofluid was collected, which contains sprayed silver nanoparticles and ionic silver, since the silver nanofluid fabricated by EDM was forming as a complex suspension fluid. There have been two main effects that will affect suspension stability, including the steric space and charged particle effects. Steric effect means higher concentration of nanofluid which will enhance particle collision and combination effect. Therefore, the crowded and negative charged silver nanoparticles will attract the positive charged ionic silver, and this makes the interaction in the resultant nanofluid becomes more complex. Like the charged particle-ion combination reaction and ions reduction reaction, then the suspension quality of nanofluid has been influenced. The factor explained by Gouy-Chapman theory that the ionic silver concentration will arise while EDM process time increased [18]. The increasing of

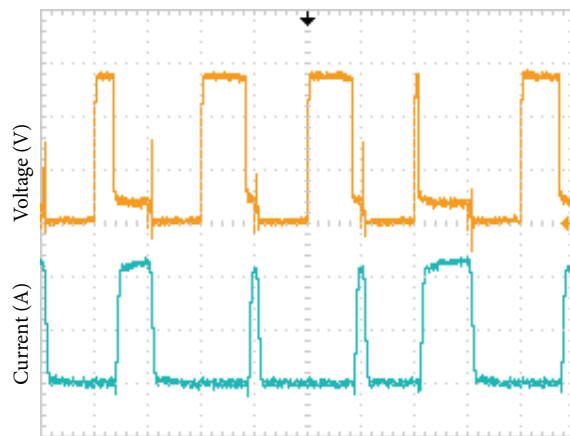


FIGURE 2: Voltage and current waveform during the EDM process.

ion concentration enables the compressing of double-layer Debye length; then the Zeta-potential magnitude gradually decayed. Finally, the suspension quality has been influenced. In addition, the concentration of suspension particle does affect Van Der Waals combination force. Thus the ionic silver concentration and the charged particle both can affect the suspension stability. In this study, the parameters of on-off duration were changed in order to investigate their influence on the process. The surface potential, size-distribution, and characteristic absorption peak value were analyzed by Zeta-potential, size-distribution, and UV-Vis spectroscopy, and the stability of fluid samples was tested through long-time observation. For the process parameters of the samples, the on-off duration of IOR and MMR maximum value was selected as the experimental objects, and the saturated and unsaturated samples obtained by the total processing time of 1 and 3 min, respectively, were analyzed.

3. Results and Discussion

3.1. Quantify the Discharge Energy. When the voltage applies to the electrode by a fixed on-off duration, not all cycles can discharge successfully. The measured electrical discharge is shown in Figure 2 (on-off duration, 30-30 μs), where the voltage pulse generated 41 pulses in this period, but only 23 current pulses were found (i.e., successful electrical discharges), so the arcing rate was around 55%. However, it is complicated to accurately quantify the discharge energy, with consideration of both the arcing rate (%) and the arcing duration (T_{arc}). Under the consideration of only the arcing rate, the oscilloscope was utilized to obtain the relative times of current signals produced by the electrical discharge machining, and the influence of different on-off durations to the arcing rate was compared. As shown in Figure 3, when the duration increased, the arcing times per second would be in proportion to the duration, theoretically; however, the experiment indicated that this slope was larger than the theoretical value. Thus, as presented in Figure 4, the arcing rate reached the maximum value at 10-10, 20-20, and 30-30 μs . That is to say, more arcs, more melted silver, could be produced at the settings of 10-10, 20-20, and 30-30 μs .

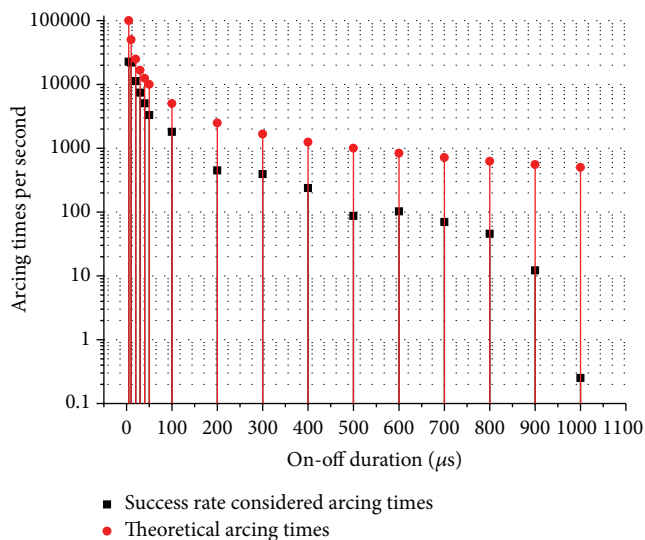


FIGURE 3: Comparison of theoretical and practical arcing times at different on-off duration.

3.2. Quantification of MRR and IOR. The concentration of particles and ions increased gradually along with time. Thus, the nanofluid contains more and more matters, results the change of steric space, ionic strength and pH value. The quantification result of MRR and IOR at different on-off duration (from 5 to 100) setting is shown in Figure 5. It shows that MRR and IOR were at the minimum when the on-off duration was set at 5-5 and 100-100 μs , but they reached the maximum values when the on-off duration setting was at 30-30 μs . This is probably because that the best arcing rate could be obtained at 30-30 μs , so MRR and IOR could reach their maximum values. High arcing rate represented that the energy accumulation and release have achieved the best fitting and were influenced by the electrode geometry, types of dielectric fluid, and magnitude of power source.

3.3. UV-Vis Analysis Results. For EDM process parameters, the on-off duration was set as 30-30 μs and the processing times as 1 and 3 min; the two samples for UV-Vis spectrum were analyzed at 400 nm. The analysis results are shown in Figure 6. The analysis method was time-based, where measurements were taken at the time 0 h, 12 h, and 24 h. The experiment revealed that the slope of sample was relatively low at 1 min; the concentrations of samples of silver nanoparticle were still larger than 2 min and 3 min at 12 h, and the concentrations of three samples were difficult to be measured at 24 h, denoting that all silver nanoparticles were deposited; so in the samples of 2 min and 3 min, the nanoparticle showed the trend of saturation.

3.4. Size-Distribution and Zeta-Potential. As shown in Figure 7, the samples of 1 min and 3 min were set at the same time points (settling for 10 min after the electrical discharge) for measurement. After settling for 10 min, the particle size of 3 min sample (~ 1200 nm) was larger than that of 1 min sample (~ 600 nm); this is because 3 min sample

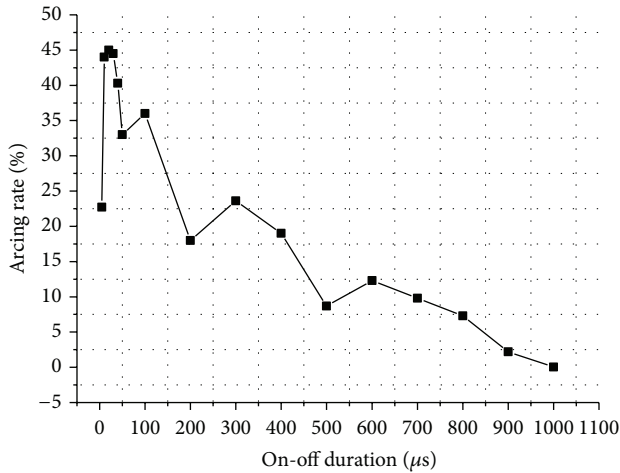


FIGURE 4: Arcing rate chart at different on-off duration.

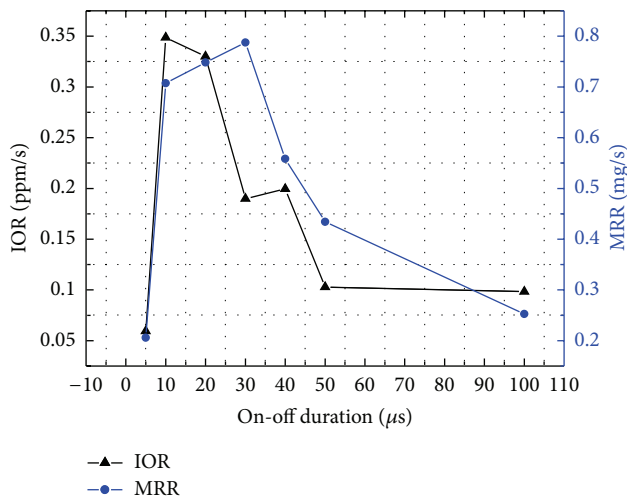


FIGURE 5: Material removal rate (MRR) and ion output rate (IOR) versus on-off duration setting.

was already saturated and aggregated during the electrical discharge. When taking the measurement after settling for 10 min, the particle would aggregate for a period of time. After the continuous measurement for 50 min, the particle sizes of 1 min and 3 min samples showed the trend of aggregation and becoming larger. The slope value of particle concentration of 3 min sample was slightly bigger than that of 1 min sample; hence, the 3 min sample particle would produce a large amount of aggregation and deposits during the electrical discharge. Since the particle concentration of 3 min sample while settling was greater than that of 1 min sample, the influence of concentration on the aggregation reaction could be known. After the EDM process, there were Ag ions and Ag particles in the dielectric fluid. The surface of Ag particles is charged (called Zeta-potential), whose magnitude dominated the suspension stability of particles. The continuous measurement of samples after settling for 15~55 min is illustrated in Figure 8. In the 3 min sample, due to greater concentration, the suspension space of charged

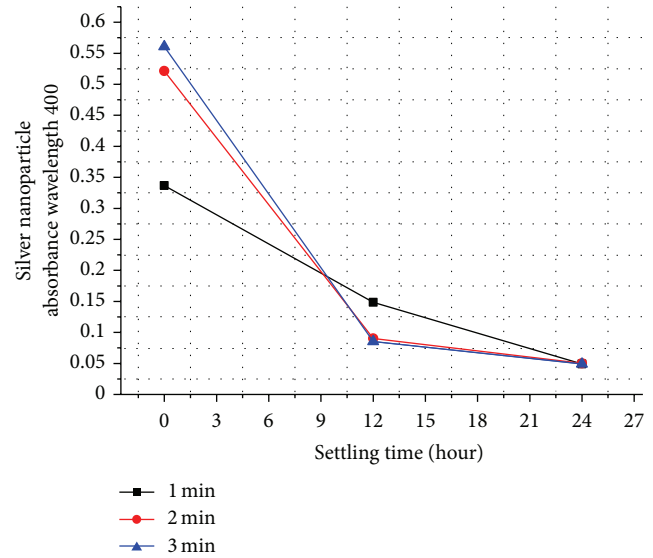


FIGURE 6: The UV-Vis absorbance of silver nanofluid at 400 nm versus settling time.

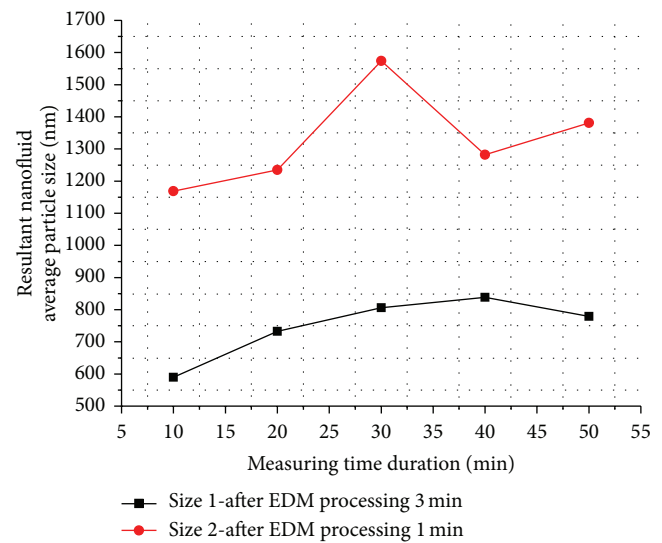


FIGURE 7: Particle size analysis of silver nanofluid.

particle was compressed; thus, the electrical double layer was compressed so that the Zeta-potential magnitude was lower than that of 1 min sample. However, through the observation of the slope of these two samples, it was found that Zeta-potential magnitude increased with time, probably because the small particles with relatively high potential became prominent after big particles aggregated and deposited.

3.5. The influence of Different On-Off Duration. In the experiment, the larger Ag particles were filtered by using the centrifugal machine. In addition, multiple groups of on-off duration control experiments were analyzed. Besides the equal proportion comparison, the on-duration and off-duration experiments were also conducted and the groups of

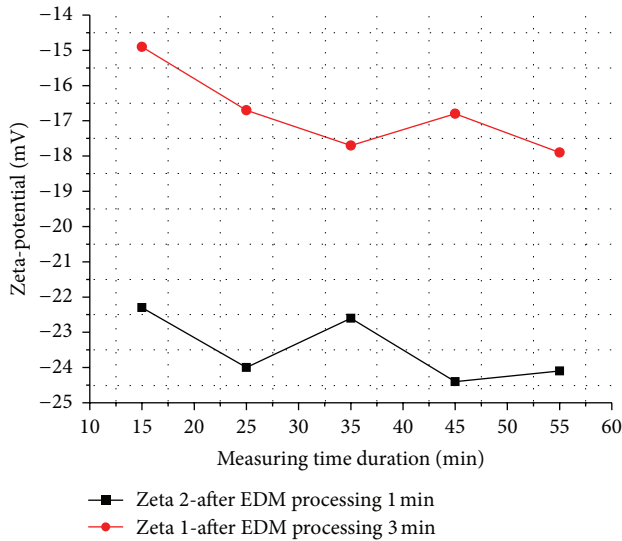


FIGURE 8: Zeta-potential analysis of silver nanofluid.

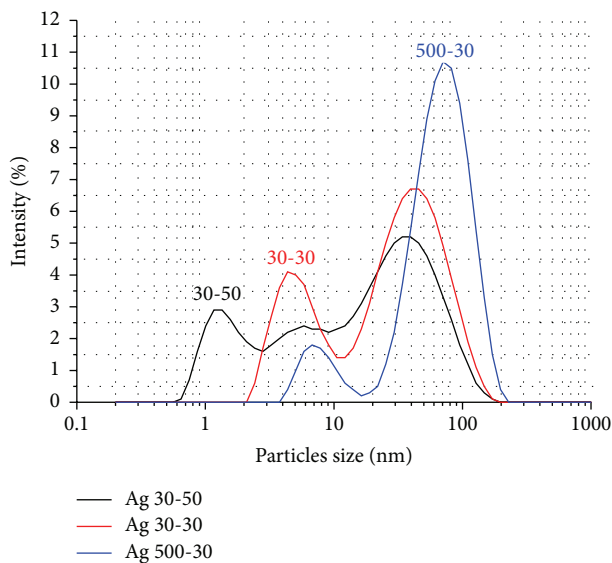


FIGURE 9: Particle size analysis of different on-off duration.

30-50, 30-30, and 500-30 were taken out for comparison. The analysis results showed that the particles of on-off duration of 500-30 were significantly larger in distribution and the most of particles were sized around 100 nm, as shown in Figure 9; under the parameter setting of 30:50, the particle size distribution was relatively smaller, and the particle size may even be smaller than 1 nm. Most of the particles suspending in the fluid were smaller in size, and a large amount of small particles extruded each other, resulting in the extrusion on the double electrode layer. Therefore, the Zeta-potential values were around -35 mV as shown in Figure 10, which was smaller than that of the larger particles sized 500:30. However, the value of the equal proportion control group sized 30:30 was between the two values.

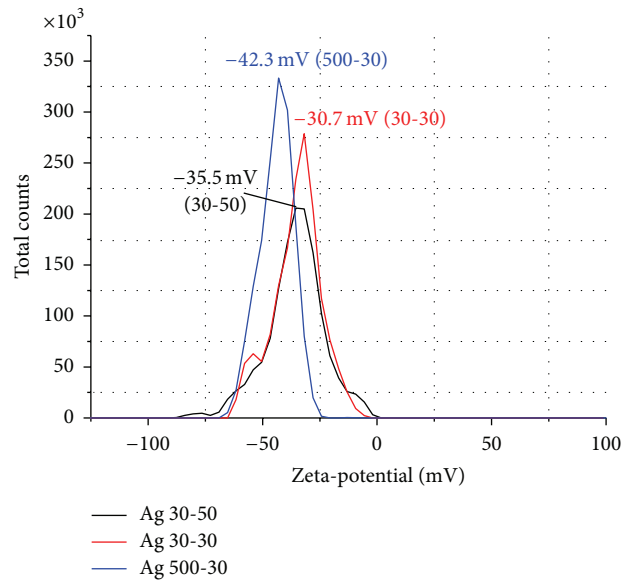


FIGURE 10: Zeta-potential analysis of different on-off duration.

4. Conclusions

This research focused on the preparation of silver nanofluid by the EDM system and the relationship between its process parameters and product characteristics. Based on the experimental results, the conclusions are summarized in the following points.

- (1) Quantifying the relationship between the process parameters and the material removal rate (MRR) of silver electrode and the ion output rate (IOR) in the fluid and identifying the most effective process parameter condition, where on-off pulse discharge duration was around 30-30 μ s.
- (2) For the analysis on stability of silver nanofluid, the variations of absorption spectrum, particle size, and Zeta-potential with time were observed, respectively, by UV-Vis spectroscopy, size-distribution, and Zeta-potential analyzer. The experiment indicated that the silver nanofluid under EDM process showed particle and ion saturation. When the process duration was too long, stable silver nanofluid could not be obtained.
- (3) The relationship of process parameters and suspensibility of silver nanofluid acquired in this study can serve as reference for future preparation of other silver nanofluids via EDM process.
- (4) After the filtering of the centrifugal machine, the Ag fluid of equal proportion parameter setting of particles sized 30-30 showed better material removal rate and the same UV absorption peak value at 400 nm. The range of the particle size distribution was about 1~200 nm and the concentration of the Ag fluid decreased with rising proportion. When increasing the on-duration setting, the size of the particles was

relatively larger and the UV absorption peak value had the “Red shift.” With increasing on-duration setting, the concentration of Ag fluid decreased. The deionization of the Ag ions enhanced under the application of the electric field. The insulation of the pure water decreased to result in a higher discharging success rate of the electrode. The concentration of discharge led to coarser and larger particles.

References

- [1] N. Parkansky, O. Goldstein, B. Alterkop et al., “Features of micro and nano-particles produced by pulsed arc submerged in ethanol,” *Powder Technology*, vol. 161, no. 3, pp. 215–219, 2006.
- [2] C. H. Lo, T. T. Tsung, and H. M. Lin, “Preparation of silver nanofluid by the submerged arc nanoparticle synthesis system (SANSS),” *Journal of Alloys and Compounds*, vol. 434–435, pp. 659–662, 2007.
- [3] K. H. Tseng, C. Y. Liao, J. C. Huang, D. C. Tien, and T. T. Tsung, “Characterization of gold nanoparticles in organic or inorganic medium (ethanol/water) fabricated by spark discharge method,” *Materials Letters*, vol. 62, no. 19, pp. 3341–3344, 2008.
- [4] Y. Y. Tsai, J. S. Su, and C. Y. Su, “A novel method to produce carbon nanotubes using EDM process,” *International Journal of Machine Tools and Manufacture*, vol. 48, no. 15, pp. 1653–1657, 2008.
- [5] N. Ichinose, Y. Ozaki, and S. Kashu, *Superfine Particle Technology*, 1992.
- [6] D. C. Tien, K. H. Tseng, C. Y. Liao, J. C. Huang, and T. T. Tsung, “Discovery of ionic silver in silver nanoparticle suspension fabricated by arc discharge method,” *Journal of Alloys and Compounds*, vol. 463, no. 1–2, pp. 408–411, 2008.
- [7] K. H. Tseng and C. Y. Liao, “Production of silver ions from colloidal silver by nanoparticle iontophoresis system,” *Journal of Nanoscience and Nanotechnology*, vol. 11, no. 3, pp. 1991–1995, 2011.
- [8] D. C. Tien, K. H. Tseng, C. Y. Liao, and T. T. Tsung, “Colloidal silver fabrication using the spark discharge system and its antimicrobial effect on *Staphylococcus aureus*,” *Medical Engineering and Physics*, vol. 30, no. 8, pp. 948–952, 2008.
- [9] H. Kim, G. DeWitt, T. McKrell, J. Buongiorno, and L. W. Hu, “On the quenching of steel and zircaloy spheres in water-based nanofluids with alumina, silica and diamond nanoparticles,” *International Journal of Multiphase Flow*, vol. 35, no. 5, pp. 427–438, 2009.
- [10] D. Zhu, X. Li, N. Wang, X. Wang, J. Gao, and H. Li, “Dispersion behavior and thermal conductivity characteristics of $\text{Al}_2\text{O}_3\text{-H}_2\text{O}$ nanofluids,” *Current Applied Physics*, vol. 9, no. 1, pp. 131–139, 2009.
- [11] N. Sano, H. Wang, I. Alexandrou et al., “Properties of carbon onions produced by an arc discharge in water,” *Journal of Applied Physics*, vol. 92, no. 5, p. 2783, 2002.
- [12] H. Chang and S. C. Lin, “Fabrication method for a TiO_2 nanofluid with high roundness and superior dispersion properties,” *Materials Transactions*, vol. 48, no. 4, pp. 836–841, 2007.
- [13] A. Calka, D. Wexler, B. Monaghan, A. Mosbah, and P. Balaz, “Rapid reduction of copper sulfide (Cu_2S) with elemental Fe and Mg using electrical discharge assisted mechanical milling (EDAMM),” *Journal of Alloys and Compounds*, vol. 486, no. 1–2, pp. 492–496, 2009.
- [14] H. Chang, M. J. Kao, C. S. Jwo, C. G. Kuo, Y. H. Yeh, and W. C. Tzeng, “Preparation of Co/Ag nanocompound fluid using ASNSS with aid of ultrasonic orthogonal vibration,” *Journal of Alloys and Compounds*, vol. 504, no. 1, pp. S376–S379, 2010.
- [15] W. Yu, D. M. France, J. L. Routbort, and S. U. S. Choi, “Review and comparison of nanofluid thermal conductivity and heat transfer enhancements,” *Heat Transfer Engineering*, vol. 29, no. 5, pp. 432–460, 2008.
- [16] K. H. Tsenga, C. Y. Liao, and D. C. Tien, “Silver carbonate and stability in colloidal silver: a by-product of the electric spark discharge method,” *Journal of Alloys and Compounds*, vol. 493, pp. 438–440, 2010.
- [17] K. Heiskanen, *Particle Classification*, Chapman and Hall, 1993.
- [18] I. D. Morrison and S. Ross, *Colloidal Dispersions Suspensions, Emulsions, and Foams*, Wiley-Interscience, 2002.
- [19] J. Jiang, G. Oberdörster, and P. Biswas, “Characterization of size, surface charge, and agglomeration state of nanoparticle dispersions for toxicological studies,” *Journal of Nanoparticle Research*, vol. 11, pp. 77–89, 2009.
- [20] T. Cosgrove, *Colloid Science: Principles, Methods and Applications*, Blackwell, 2005.
- [21] T. Pradeep, *NANO: The Essentials*, McGraw-Hill Education, 2007.
- [22] S. Jailani, G. V. Franks, and T. W. Healy, “ ζ Potential of nanoparticle suspensions: effect of electrolyte concentration, particle size, and volume fraction,” *Journal of the American Ceramic Society*, vol. 91, no. 4, pp. 1141–1147, 2008.
- [23] Y. Liang and J. Binner, “Effect of triblock copolymer non-ionic surfactants on the rheology of 3 mol% yttria stabilised zirconia nanosuspensions,” *Ceramics International*, vol. 34, no. 2, pp. 293–297, 2008.
- [24] F. Caruso, *Colloids and Colloid Assemblies*, Wiley-VCH, 2004.
- [25] D. Kong, H. Yang, Y. Yang, S. Wei, J. Wang, and B. Cheng, “Dispersion behavior and stabilization mechanism of alumina powders in silica sol,” *Materials Letters*, vol. 58, no. 27–28, pp. 3503–3508, 2004.
- [26] J. J. McDermott and D. Velegol, “Simple fabrication of metallic colloidal doublets having electrical connectivity,” *Langmuir*, vol. 24, no. 8, pp. 4335–4339, 2008.
- [27] T. Tsuji, D. H. Thang, Y. Okazaki, M. Nakanishi, Y. Tsuboi, and M. Tsuji, “Preparation of silver nanoparticles by laser ablation in polyvinylpyrrolidone solutions,” *Applied Surface Science*, vol. 254, no. 16, pp. 5224–5230, 2008.
- [28] M. F. Meléndrez, G. Cárdenas, J. Díaz, C. Cruzat, and J. Arbiol, “Synthesis and aggregation study of tin nanoparticles and colloids obtained by chemical liquid deposition,” *Colloid and Polymer Science*, vol. 287, pp. 13–22, 2009.
- [29] S. H. Yeo, W. Kurnia, and P. C. Tan, “Critical assessment and numerical comparison of electro-thermal models in EDM,” *Journal of Materials Processing Technology*, vol. 203, no. 1–3, pp. 241–251, 2008.
- [30] K. Salonitis, A. Stournaras, P. Stavropoulos, and G. Chrysolouris, “Thermal modeling of the material removal rate and surface roughness for die-sinking EDM,” *International Journal of Advanced Manufacturing Technology*, vol. 40, no. 3–4, pp. 316–323, 2009.
- [31] S. Son, H. Lim, A. S. Kumar, and M. Rahman, “Influences of pulsed power condition on the machining properties in micro EDM,” *Journal of Materials Processing Technology*, vol. 190, no. 1–3, pp. 73–76, 2007.

Research Article

Improved Antireflection Properties of an Optical Film Surface with Mixing Conical Subwavelength Structures

Chi-Feng Chen,^{1,2} Yu-Cheng Cheng,¹ and Chia-Jen Ting³

¹ Department of Mechanical Engineering, National Central University, Jhongli, Taiwan

² Institute of Opto-Mechatronics Engineering, National Central University, Jhongli, Taiwan

³ Mechanical and Systems Research Laboratories, Industrial Technology Research Institute, Hsinchu 31040, Taiwan

Correspondence should be addressed to Yu-Cheng Cheng; koalaking0205@gmail.com

Received 7 December 2012; Accepted 28 February 2013

Academic Editor: Jian Wei

Copyright © 2013 Chi-Feng Chen et al. This is an open access article distributed under the Creative Commons Attribution License, which permits unrestricted use, distribution, and reproduction in any medium, provided the original work is properly cited.

Based on finite difference time domain method, an optical film surface with mixing conical subwavelength structures is numerically investigated to improve antireflection property. The mixing conical subwavelength structure is combined with the pure periodic conical subwavelength structures and the added small conical structures in the gap between the pure periodic conical subwavelength structures. The antireflection properties of two types of subwavelength structures with different aspect ratios in spectral range of 400–800 nm are analyzed and compared. It is shown that, for the mixing type, the average reflectance is decreased and the variances of the reflectance are evidently smaller. When the added structure with a better aspect ratio exists, the average reflectance of the surface can be below 0.30%. Obviously, the antireflection properties of the optical film surface with mixing conical subwavelength structures can be improved.

1. Introduction

Antireflection coatings have been widely used to realize high efficiency in optical components and optoelectronics devices by eliminating unwanted surface reflections. We expect that the reflectional light is omitted or suppressed in many optical systems. The subwavelength structure (SWS) technology, which is inspired by the moth-eye effect, is a powerful method to realize the broadband antireflective effect. The specific subwavelength structure pattern, called antireflective subwavelength structure, on optical element surface produced by the nanostructure fabrication technology has been widely researched [1–4].

For the theoretical consideration, there are kinds of methods that can simulate electromagnetic wave transmission like rigorous coupled-wave analysis (RCWA), finite difference time domain (FDTD), or plane wave expansion method (PWE), and in the same research it is showed that the FDTD method is the effectual simulation tool used in 3D periodic SWS [5, 6]. It is directly calculated by the full-vector Maxwell's equations [6, 7]. Since it is a time-domain method,

FDTD solutions can cover a wide frequency range with a single simulation run and treat nonlinear material properties in a natural way. FDTD method is a systematic approach, with FDTD specifying a new structure to be modeled being reduced to a problem of mesh generation rather than the potentially complex reformulation of an integral equation [8]. In past studies, the antireflection coating has been fabricated in subwavelength structure technology and simulated in FDTD method at the same time. The average reflectances of the simulation and replicated polymer prototype are about 0.50% and 0.54% within the spectral ranges of 400–650 nm, respectively. The results showed that the FDTD method is an effective way to simulate electromagnetic wave propagation [9, 10].

In past works, antireflective characteristics of the SWS depend strongly on its dimensions and geometric shape, and there are some specific shapes can be fabricated like conical, cylinder, that pyramidal shapes. Subwavelength structure in low reflectance can also be obtained by both conical and pyramidal shapes over a broadband range. Comparing the reflectance of different structure shapes and aspect ratios

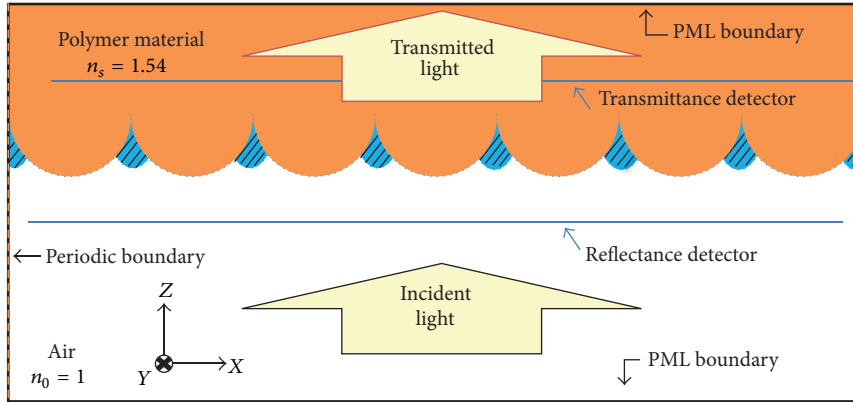


FIGURE 1: Sketch of the light-wave propagation through an optical film with SWS system simulated by the FDTD method.

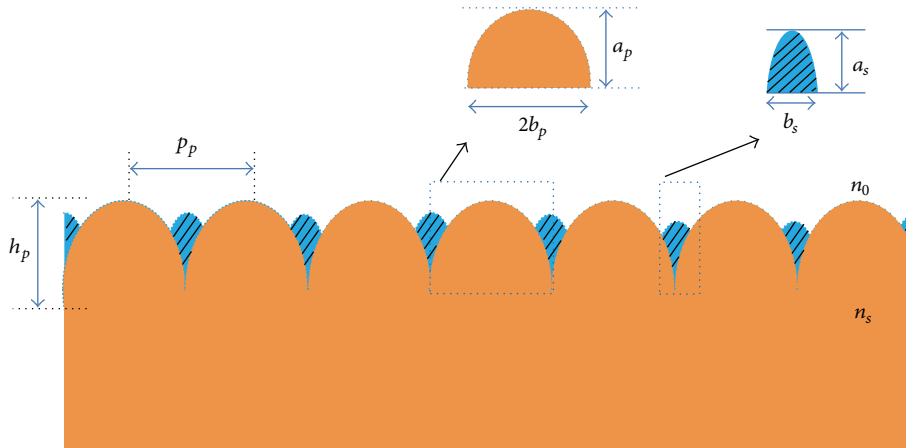


FIGURE 2: Schematic profiles of SWS surfaces with the composite structure surfaces.

by the FDTD method, it is shown that the antireflection efficiencies of the pyramidal structures are better than the conical structures in some particular ratios. It is also found that, for the conical structure surface, the average transmittance increases gradually with the aspect ratio and the average transmittance is about 99.6% [11].

In this study, we consider a new composite subwavelength structures based on pure periodic conical SWS [11] and adding a small conical structure in the gap between the pure periodic conical subwavelength structures and numerically analyze the optical characters of SWS of surfaces by using FDTD method to directly solve the full-vector Maxwell's equations. For the profile parameter of the conical SWS structures, the antireflection property is analyzed in a spectral range from 400 nm to 800 nm.

2. Structure and Method

We use FDTD method to design the parameters which are based on periodic conical subwavelength structures in

different spectral range. We consider that the light wave propagates from the air through the antireflective subwavelength structures surfaces into the polymer material in plane wave, and the absorption loss of the medium can be ignored. The design structured can be fabricated by microreplication process combined with the originated structure fabrication realized by interference lithography, Ni mold electroplating, and replication by the use of UV imprinting onto plastics.

The sketch of simulation model is shown in Figure 1, where n_0 and n_s are the refractive indices of the incident medium and polymer materials, respectively. Here, we choose $n_0 = 1$ for air and $n_s = 1.54$ for polymer material. In FDTD simulation, absorbing boundary conditions are required to truncate the computational domain without reflection. A perfect matched layer (PML) is a useful method to decrease the error induced from the boundary situation [12] in z -direction, and according to the Floquet theory [13] in periodic boundary condition in x -direction, we use the PML and periodic boundary to be the simulate area, and energy of transmittance light wave is measured by detector 1,

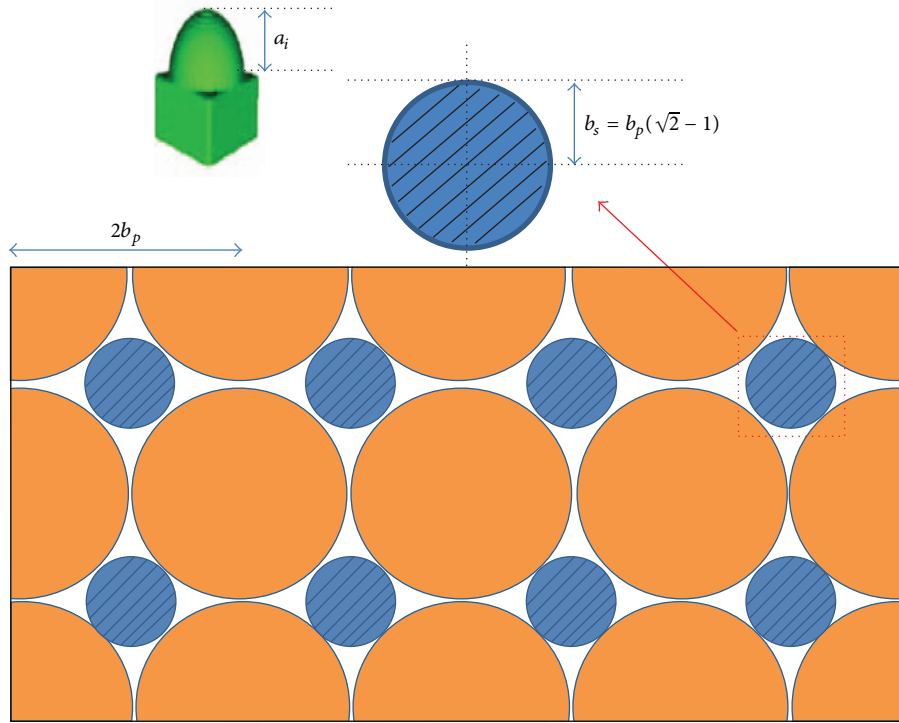


FIGURE 3: Schematic profiles of the SWS surfaces between the pure structures and the small structures.

and energy of reflectance light wave is measured by detector 2, respectively.

Figure 2 shows the schematic diagram of the SWS surfaces with the composite structures, and we can see these structures composed by the pure periodic conical subwavelength structures and extra small structures in the gap between the pure periodic conical subwavelength structures. The parameters of SWS surfaces with the composite structure surfaces in Figure 2, where the symbols p_p and h_p denote pure periodic structure's spatial period and spatial height, and the symbols a_s and b_s denote small structure's height and width. The height of ellipsoid a_p is equal to the spatial height h_p , and the radius of ellipsoid b_p is close to the spatial period p_p .

In this study, we add these small subwavelength structures and discuss their ratios influences to the whole SWS about reflection and transmittance. We can see the connected relation in Figure 3 between b_p and b_s : $b_s = b_p(\sqrt{2} - 1)$.

3. Results and Discussion

First, we describe the effect of the original SWSs which are pure periodic conical structures without small SWSs, and we can see the phenomenon in Figures 4(a)–4(d) in black line with circle pattern. And then, we consider holding the height and width of each pure periodic structure unit, where $p_p = h_p = a_p = 2b_p = 300$ nm, which we defined as the pure structure ratios (PSR), and adopting the small SWS height from ratios 0.00 to 1.00, where we defined the small structure ratios (SSR) as a_s/b_s . The variances of the reflectance for the small structures in spectral ranges of 400–800 nm

are shown in Figure 4. One can see that the reflectance has obviously decreased when we add the small SWS, and we show the best ratios which have the lowest reflectance and the same height with the small SWSs and pure periodic SWSs. We can also find that it has a stable reflectance after we use the nanostructure material for the coating surfaces.

We can analyze the data of reflectance; it is shown the average reflectance of pure periodic SWSs that below 0.48%, and the average reflectance of the improved SWS is below 0.29%. In the meantime, we can see that the different ratios of small SWSs have different effects in Figure 4. The reflectance and ratios of small structures have some relations. And in this way, we select three conditions, which are the pure SWSs, the same high small SWSs to the pure periodic SWSs, and the lowest aspect ratios of the small SWSs, in Figure 4. We can see that the reflectance of the pure periodic SWS has a ranges 0.14%~0.72%, 0.03%~0.47%, 0.01%~0.47%, and 0.05%~0.45%, and the new SWSs improved the effect from 0.22%~0.37%, 0.05%~0.27%, 0.02%~0.23%, 0.04%~0.2% in Figures 4(a)–4(d). We can also see the variances of the standard deviation for different small structures ratios of each pure periodic structure in Figure 5; it is shown that the small SWSs also have a property to keep the reflectance in a stable state. This antireflection property can be improved about 40–60% from the original structure.

4. Summary

We use the FDTD method to analyze the antireflection effect of SWS in a spectral range from 400 nm to 800 nm.

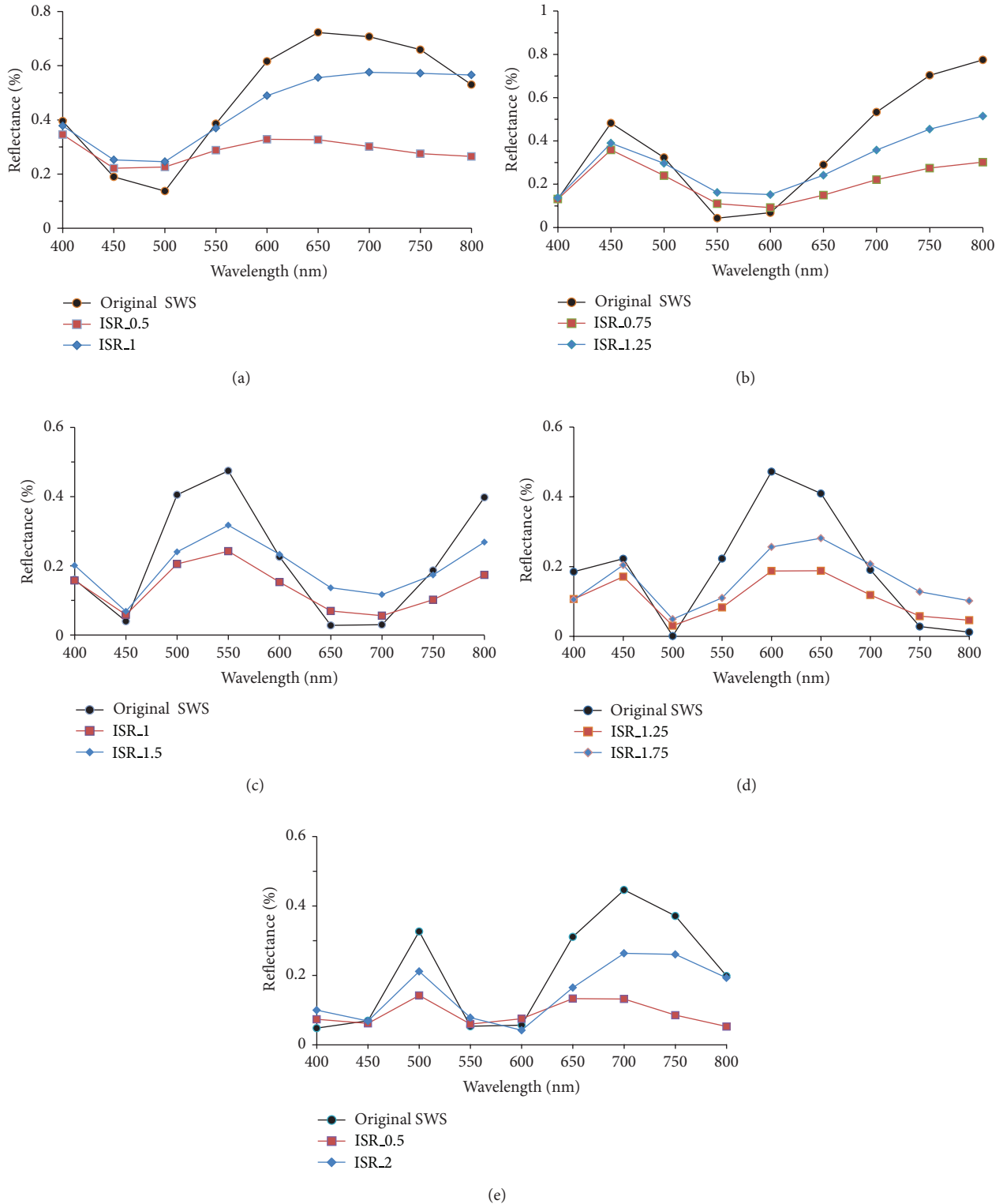


FIGURE 4: Variances of the reflectances for the pure periodic structures and different small structures ratios.

Such antireflection pattern is useful for solar cells, photodetectors, LEDs, and high-end imaging lens. We consider the pure periodic conical subwavelength structure and adding a small structure in the gap between the structures. It is

found that the antireflection function has obviously decreases in different ratios of the added small structures. A better ratio of the small structure is obtained, and the average reflectance can be below 0.30%. The optimal design of

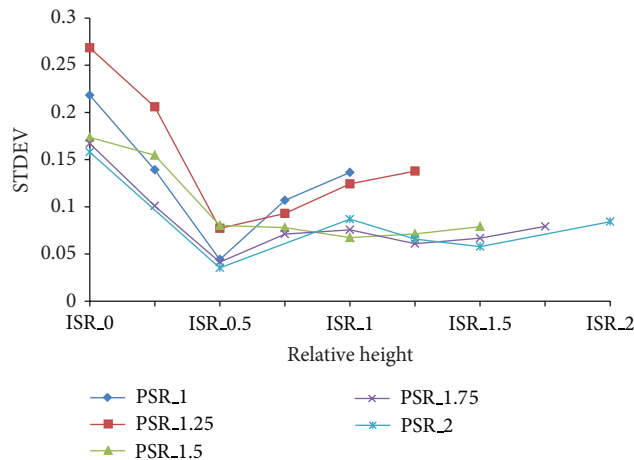


FIGURE 5: Variances of the standard deviation for different small structure ratios of each pure structure ratio.

the new SWS in conical shape can also steady the entire reflectance.

References

- [1] M. F. Land and D. E. Nilsson, *Animal Eyes*, Oxford University Press, New York, NY, USA, 2002.
- [2] A. R. Parker, *Blink of an Eye*, Cambridge University Press, Boston, Mass, USA, 2003.
- [3] L. P. Biro and J. P. Vigneron, "Photonic nanoarchitectures in butterflies and beetles: valuable sources for bioinspiration," *Laser & Photonics Reviews*, vol. 5, pp. 27–51, 2011.
- [4] Ph. Ball, *The Self-Made Tapestry: Pattern Formation in Nature*, Oxford University Press, New York, NY, USA, 1999.
- [5] Y. Li, M. Y. Lee, H. W. Cheng, and Z. L. Lu, "3D simulation of morphological effect on reflectance of Si_3N_4 sub-wavelength structures for silicon solar cells," *Nanoscale Research Letters*, vol. 7, no. 1, p. 196, 2012.
- [6] J. P. Bérenger, "Perfectly matched layer for the FDTD solution of wave-structure interaction problems," *IEEE Transactions on Antennas and Propagation*, vol. 44, no. 1, pp. 110–117, 1996.
- [7] E. Hecht, *Optics*, Addison-Wesley, Reading, Mass, USA, 4th edition, 2002.
- [8] A. Taflove and S. C. Hagness, *Computational Electrodynamics: the Finite-Difference Time-Domain Method*, Artech House Publishers, 3rd edition, 2005.
- [9] C. J. Ting, F. Y. Chang, C. F. Chen, and C. P. Chou, "Fabrication of an antireflective polymer optical film with subwavelength structures using a roll-to-roll micro-replication process," *Journal of Micromechanics and Microengineering*, vol. 18, no. 7, Article ID 075001, 2008.
- [10] C. J. Ting, C. F. Chen, and C. P. Chou, "Subwavelength structures for broadband antireflection application," *Optics Communications*, vol. 282, no. 3, pp. 434–438, 2009.
- [11] C. J. Ting, C. F. Chen, and C. J. Hsu, "Subwavelength structured surfaces with a broadband antireflection function analyzed by using a finite difference time domain method," *Optik*, vol. 121, no. 12, pp. 1069–1074, 2010.
- [12] K. L. Hong and L. K. Cheng, "Anisotropic PML B.C. for periodic FDTD calculation," *ACTA Electronica Sinica*, vol. 28, no. 12, pp. 111–114, 2000.
- [13] F. P. Hunsberger, K. S. Kunz, R. B. Standler, M. P. Schneider, and R. Luebbers, "A frequency-dependent finite-difference time-domain formulation for dispersive materials," *IEEE Transactions on Electromagnetic Compatibility*, vol. 32, no. 3, pp. 222–227, 1990.

Research Article

Densely Packed Linear Assemblies of Carbon Nanotube Bundles in Polysiloxane-Based Nanocomposite Films

Hong-Baek Cho,¹ Minh Triet Tan Huynh,¹ Tadachika Nakayama,¹ Son Thanh Nguyen,¹ Hisayuki Suematsu,¹ Tsuneo Suzuki,¹ Weihua Jiang,¹ Satoshi Tanaka,¹ Yoshinori Tokoi,² Soo Wahn Lee,³ Tohoru Sekino,⁴ and Koichi Niihara¹

¹ Extreme Energy-Density Research Institute, Nagaoka University of Technology, Nagaoka, Niigata 940-2188, Japan

² Department of Electrical and Engineering System Engineering, Nagaoka National College of Technology, Nagaoka, Niigata 940-8532, Japan

³ Department of Environment Engineering, Sun Moon University, Asan, Chung Nam 336-708, Republic of Korea

⁴ Institute of Multidisciplinary Research for Advanced Materials, Tohoku University, Sendai, Miyagi 980-8577, Japan

Correspondence should be addressed to Hong-Baek Cho; hong-baekcho@etigo.nagaokaut.ac.jp

Received 13 December 2012; Accepted 18 January 2013

Academic Editor: Jian Wei

Copyright © 2013 Hong-Baek Cho et al. This is an open access article distributed under the Creative Commons Attribution License, which permits unrestricted use, distribution, and reproduction in any medium, provided the original work is properly cited.

Linear assemblies of carbon nanotubes (LACNTs) were fabricated and controlled in polysiloxane-based nanocomposite films and the effects of the LACNTs on the thermal and electrical properties of the films were investigated. CNTs were dispersed by mechanical stirring and sonication in a prepolymer of polysiloxane. Homogeneous suspensions were cast on polyamide spacers and oriented by linear-assembly by applying DC and switching DC electric fields before the mixture became cross-linked. Densely packed LACNTs that fixed the composite film surfaces were fabricated with various structures and thicknesses that depended on the DC and switching DC conditions. Polymer nanocomposites with different LACNT densities exhibited enhanced thermal and electrical conductivities and high optical transmittances. They are considered promising structural materials for electronic sectors in automotive and aerospace applications.

1. Introduction

Polymer-based nanocomposites, which are formed by adding a small amount of nanoparticles to a polymer matrix, have generated great interest in science and engineering because they exhibit superior mechanical, thermal, and electrical properties through controlled assembly of inclusions [1–4]. Polymers are multifunctional materials with superior properties, including reasonable strength, good processability, and high elasticity. Consequently, polymer-based materials are widely used in various applications including electrical devices, filtration, and biomedical applications [5]. However, polymers have very low thermal conductivities. It is thus necessary to increase the thermal conductivities of polymer-based materials for scientific and industrial applications. The physical properties of polymer-based materials have been improved by adding fillers with high thermal or electrical

conductivities such as boron nitride (BN) [6, 7], carbon nanotubes (CNTs) [8–10], and graphite nanosheets [11] to polymer matrices. The thermal conductivities of such composites are strongly affected by the dispersion, orientation, and linear alignment of inorganic fillers aligned to parallel to the thermal flux [12–14] in polymer matrices [15]. The orientation and formation of network structures containing small quantities of nanofillers in a polymer matrix can be controlled by applying a shear force [16], a magnetic field [17], or an electric field [18–20], or by mechanical stretching [21, 22]. Of these methods, orienting conducting or dielectric nanofillers by applying an electric field has the advantage that the fillers form self-assembled linear structures due to Coulombic attraction during electrophoretic movement in a polymer with a controlled viscosity [23, 24]. Assembly of fillers with end-to-end attachment can also reduce the thermal boundary resistance. This cannot be achieved in

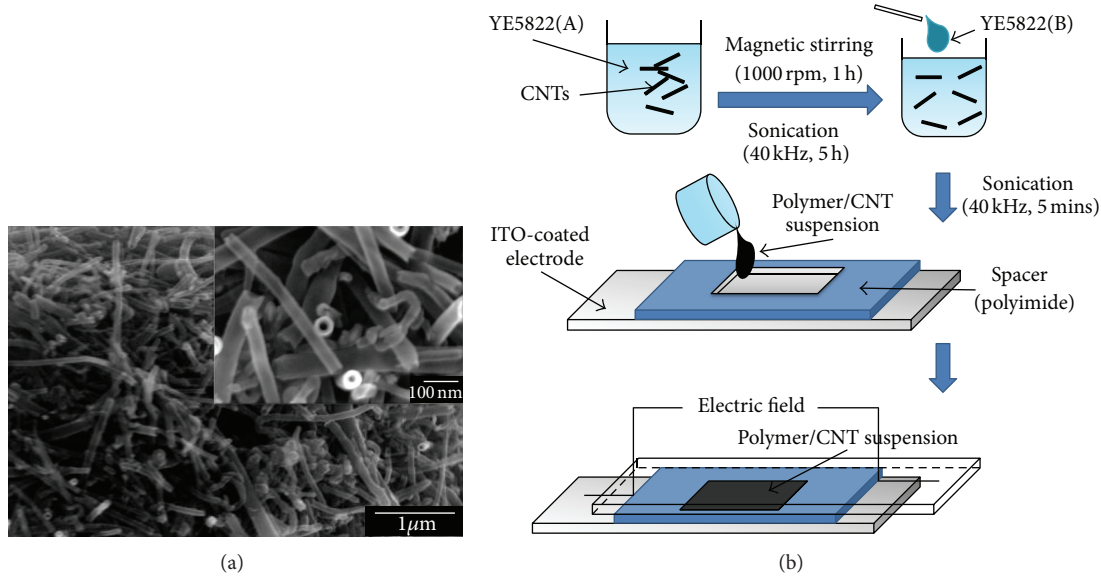


FIGURE 1: (a) SEM images of CNTs and (b) experimental setup for fabricating polysiloxane/CNT nanocomposite films.

composites with random filler orientation or using other torque sources, such as shear or a magnetic field, which can only change the orientations of 1D or 2D fillers [16, 17, 25].

Since the first report in 1991 by Iijima [26], CNTs have attracted great interest in many areas of scientific research. There are two forms of CNTs: single-walled CNTs (SWCNTs) and multiwalled CNTs. Tubular structures formed from hexagonal arrangements of carbon atoms [27] give rise to the unique physical properties of CNTs, such as extremely high Young's moduli [28–30], high axial thermal conductivities (about 3000 W/mK for multiwalled CNTs even higher for SWCNTs [10, 31], and remarkable electrical properties [18]. These properties make CNTs promising fillers for enhancing the thermal conductivity and other physical properties of polymer-based nanocomposites [32].

However, low-dimensional fillers such as CNTs tend to form agglomerates that have random orientations. This reduces the efficiency of acoustic phonon transfer across polymer-based composite films [33]. Therefore, attaining a homogeneous dispersion of CNTs is important prior to fabricating controlled assemblies of CNT in a polymer [34, 35]. Using CNTs with higher aspect ratios and straightness increases the anisotropy and the thermal conductivity of composites because the fillers form conduction paths at lower filler contents [36]. DC and AC electric fields have been applied when incorporating CNTs in a polymer [10, 18, 37]. In a DC electric field, CNTs move and form a linear dendritic structure that develops and extends from the positive electrode to the negative electrode so that the electrodes eventually become connected by the CNTs in the polymer matrix [24, 37]. When an AC electric field is applied, the CNTs reorient and form network structures oriented perpendicular to the film surface [38]. The modulation of fillers consisting of linear assemblies of CNTs (LACNTs) in polymer-based composites has not been studied. Here, we demonstrate that

modulating the DC electric field causes LACNTs to form densely packed structures in a polysiloxane matrix, which noticeably enhances the thermal and electrical properties and the optical transmittance of the nanocomposite films.

The four main objectives of this study are to fabricate self-assemblies of CNTs in polymer-based films, to investigate the effects of applying DC and switching DC fields on linear structure formation, to determine the effect of the linear structures on the thermal and electrical properties of the resulting nanocomposites, and to elucidate the formation mechanism of densely packed LACNTs. Homogeneously dispersed CNTs in a prepolymer mixture of polysiloxane were subjected to a DC field or a switching DC field during cross-linking. Scanning electron microscopy (SEM) and digital microscopy observations and thermal diffusivity, UV-Vis transmission, and electrical resistivity measurements were used to characterize the polysiloxane/CNT nanocomposites.

2. Experimental

2.1. Materials. Polysiloxane/CNT nanocomposites were prepared by introducing CNTs into a polysiloxane prepolymer mixture. As-purchased CNTs (GSI Creos Co. Ltd., Tokyo, Japan, density: 2.0 g/cm³) were used without further treatment, as shown in Figure 1(a), which confirms that the dimension of CNTs (average length: 5 μm; inside diameter: 50–70 nm; outer diameter: 80–100 nm). Two prepolymers with different viscosities were used to prepare polysiloxane: YE5822(A) (viscosity: 1.2 Pa·s, $M_{w,av}$: 21,000) and YE5822(B) (viscosity: 0.2 Pa·s, $M_{w,av}$: 16,000) (purchased from Momentive Performance Materials). The electrode for applying the electric field was an indium tin oxide (ITO) coated glass slide (2.5 × 7.5 × 1.0 mm³) that had a surface resistivity of 8–12 Ω/sq (Sigma-Aldrich).

2.2. Fabrication of LACNTs in Polysiloxane/CNT Composites. Polysiloxane/CNT nanocomposites were prepared by the following method (see Figure 1(b)). Various amounts of CNT were incorporated into prepolymer of polysiloxane ranging from 0~0.15 vol%. For example, 0.0011 g of CNTs (0.05 vol%) were distributed in 2 g of prepolymer YE5822(A) by ultrasonic treatment for 5 h after mechanical stirring at 1000 rpm for 1 h. 0.2 g of YE5822(B) were introduced into the mixture and sonicated for 5 min to produce a homogeneous dispersion. This dispersion was placed on a polyamide spacer ($1.2 \times 1.2 \text{ mm}^2 \times 120 \mu\text{m}$), which was placed between two electrodes. DC and switching DC electric fields were applied for 16 h at room temperature to enhance the orientation and assembly by relocation of the CNTs in the prepolymer suspensions. To switch the DC electric field, the polarity of the electric field was reversed during the 16 h application of the electric field in four different intervals of 2 h (seven times), 2 h 40 min (five times), 4 h (three times), and 8 h (once). Finally, the prepared composites were dried for 30 min at 80°C to complete curing.

2.3. Characterization and Measurements. The viscosity of prepolymer/CNT suspension was measured using a cone-plate (Haake, RheoWin, Thermo Scientific Co.). The surface morphology of the CNT fillers was observed by SEM (JEOL, JSM-6700F). The orientation and linear structure of CNT fillers in the polysiloxane matrix were observed by a digital microscope (Keyence, VHX-9000) after cross-sectional cutting the films. To evaluate the dispersion and orientation, the transmittance of the composites was measured using a UV-visible spectrometer (V630, JASCO). The thermal conductivities of the films were measured using a system for measuring thermal diffusivity based on temperature wave analysis (ai-Phase Mobile 1, ai-Phase Co.). The surface resistivity of composite films was measured using a digital multimeter (Advantest R6581) and an AC/DC power supply (Hioki, wt-8752) by the two-point probe method, which is capable of measuring high surface resistivities.

3. Results and Discussion

Figure 2 shows the viscosity of the prepolymer/CNT suspension as a function of stirring time. The viscosity increases with the degree of cross-linking of the two prepolymers. The viscosity increased very gradually until 2 h of mixing. It increased rapidly after 2 h and 30 min when it increased to 1200 Pa.s over 50 min, the fabrication of a polymer composite film. This is typical behavior during polymerization of a prepolymer suspension. This measurement was performed while mixing the suspension, which was exposed to air. These conditions differ from those used to fabricate nanocomposites in an electric field for which the prepolymer mixture is in a sealed container between two ITO-coated electrodes and the polyimide spacer. Consequently, the viscosity may increase considerably faster than in actual fabrication conditions. However, the trend of the viscosity variation of the prepolymer mixture provides information regarding the basic tendency of the polymer viscosity during cross-linking,

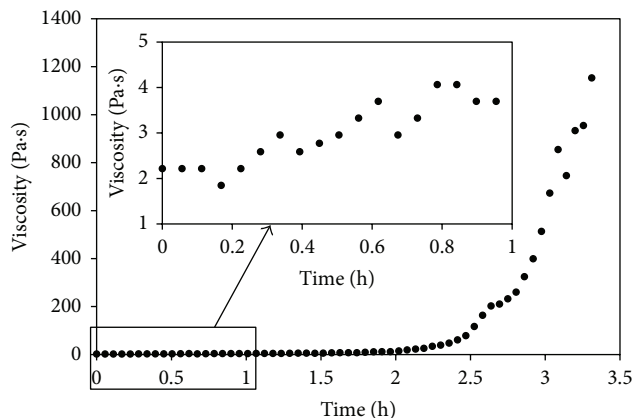


FIGURE 2: Variation of viscosity of prepolymer and CNT suspension as a function of mixing time (inset: magnification of viscosity responses between 0 and 1 h of mixing time).

which can be used to develop a strategy for controlling the electric field induced torque to improve the orientation and assembly of CNTs in the polymer matrix. The observed tendency implies that CNT assembly finishes before the steep increase in the viscosity. Complete cross-linking of the polysiloxane prepolymer was indirectly determined from the DC breakdown voltage [39]. The breakdown voltage increases as a function of the polymerization of the prepolymer suspension; it stabilized after applying an electric field for 16 h, which corresponds to the completion of polymerization.

Figure 3 shows surface and cross-sectional micrographs of polysiloxane/CNT nanocomposites fabricated under different electric fields. The dark microscale domains of CNTs indicated by the white circles in the surface micrographs in Figures 3(a1)–3(c1) reveal that many CNTs agglomerate. These agglomerates are homogeneously distributed over a smaller scale in the polymer without the application of an electric field. They form linearly aligned assembly when an electric field is applied Figures 3(b2)–3(c2). Applying DC (Figure 3(b)) and switching DC (Figure 3(c)) electric fields gives quite different CNT structures in the polymer matrix, as both the surface and cross-sectional images show. After applying DC and switching DC electric fields, the dark domains, which correspond to CNTs agglomerates and tips of LACNTs that anchor the film surfaces, were observed on the surfaces of the nanocomposite films. While applying both DC and switching DC fields causes the fabrication of LACNTs, the LACNT population and the CNT density in the linear structures vary depending on the applied electric field.

Comparison of the cross-sectional images in Figures 3(b2) and 3(c2) reveals that the LACNTs fabricated under a switching DC field are thicker and darker than those fabricated under a DC field. The slightly lower number of identifiable LACNTs produced by the DC field compared with the switching DC field indicates that some LACNTs were incorporated in other LACNTs, increasing their thickness. This gives rise to the denser packing of CNTs in LACNTs. The interconnected LACNTs networks indicated by the circles in Figure 3(c) may be related to traces

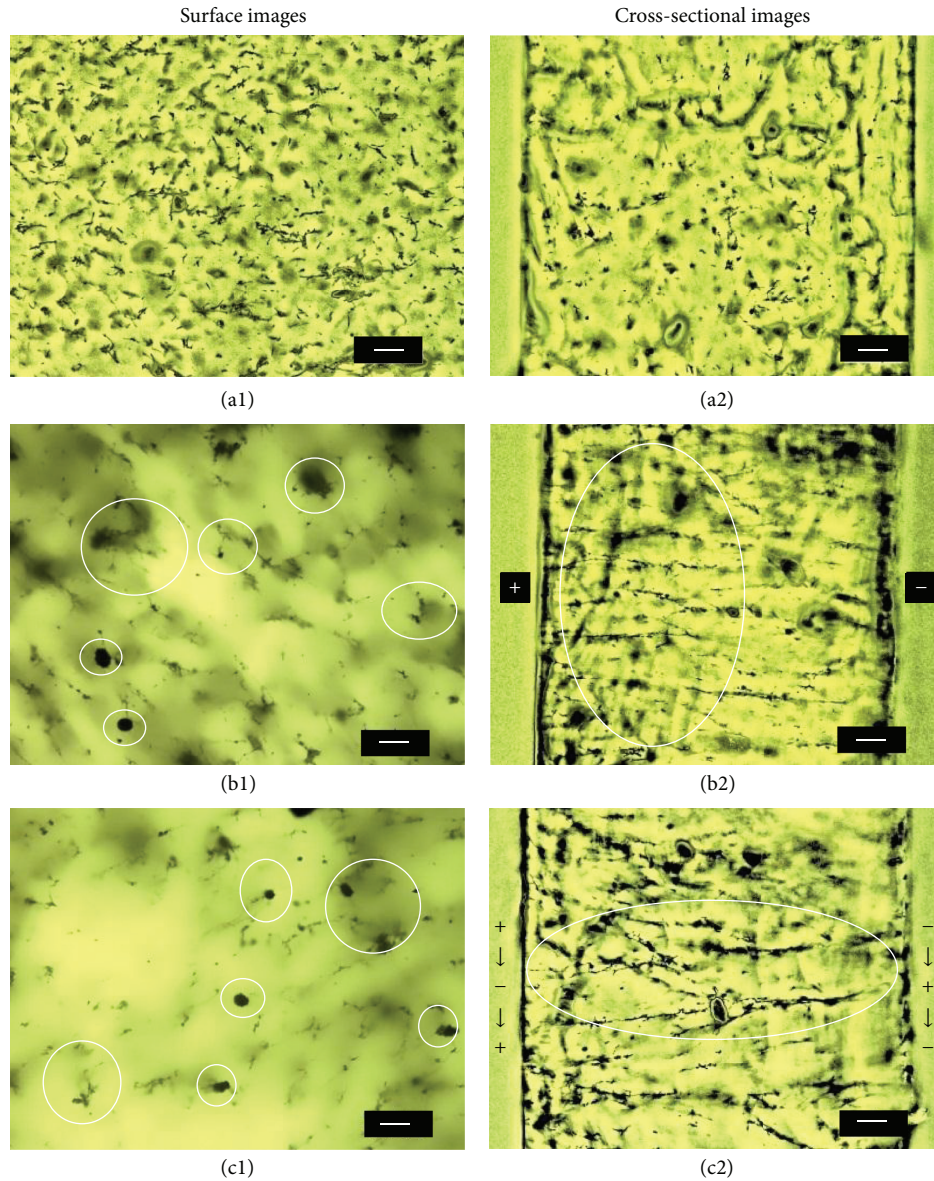


FIGURE 3: Digital micrographs of polysiloxane/CNT nanocomposites prepared by applying different electric fields (CNT: 0.05 vol%; scale bar: 20 μm); (a) no electric field, (b) DC electric field, (c) SWDC_4h (three times).

formed during incorporation of LACNTs when switching the electric field. Comparison of the surface images for DC and switching DC shows that domains with fewer but thicker CNT agglomerates are obtained by the switching DC field. This implies that applying a switching DC field increases the CNT population in LACNTs. When an electric field is applied, polarized 1D or 2D dielectric fillers tend to orient their longitudinal directions parallel to the electric flux to minimize the electrostatic energy [16]. The polarized ends of CNTs become interconnected through Coulomb attraction forming a side-by-side attachment of CNTs due to self-assembly and generating a dendritic structure of CNTs [37]. This structure in which one end is localized to the anode electrode is typical when a DC electric field is

applied [24]. An increased thickness in LACNT bundles has previously been observed when CNT surfaces were modified with tetraoctylammonium and bromide ions for charge stabilization in an electric field that was alternately switched on and off [20]. However, there have been no reports of controlling LACNT thickness by just modulating external torque sources. Thus, the formation of LACNTs that anchor the composite surfaces and the increase in the LACNT thickness on applying a switching DC field are a novel observation.

To investigate the modulation of LACNT structures in a switching DC electric field, the polysiloxane/CNT suspensions were subjected to DC fields with different switching intervals, as shown in Figure 4. For a DC switching with

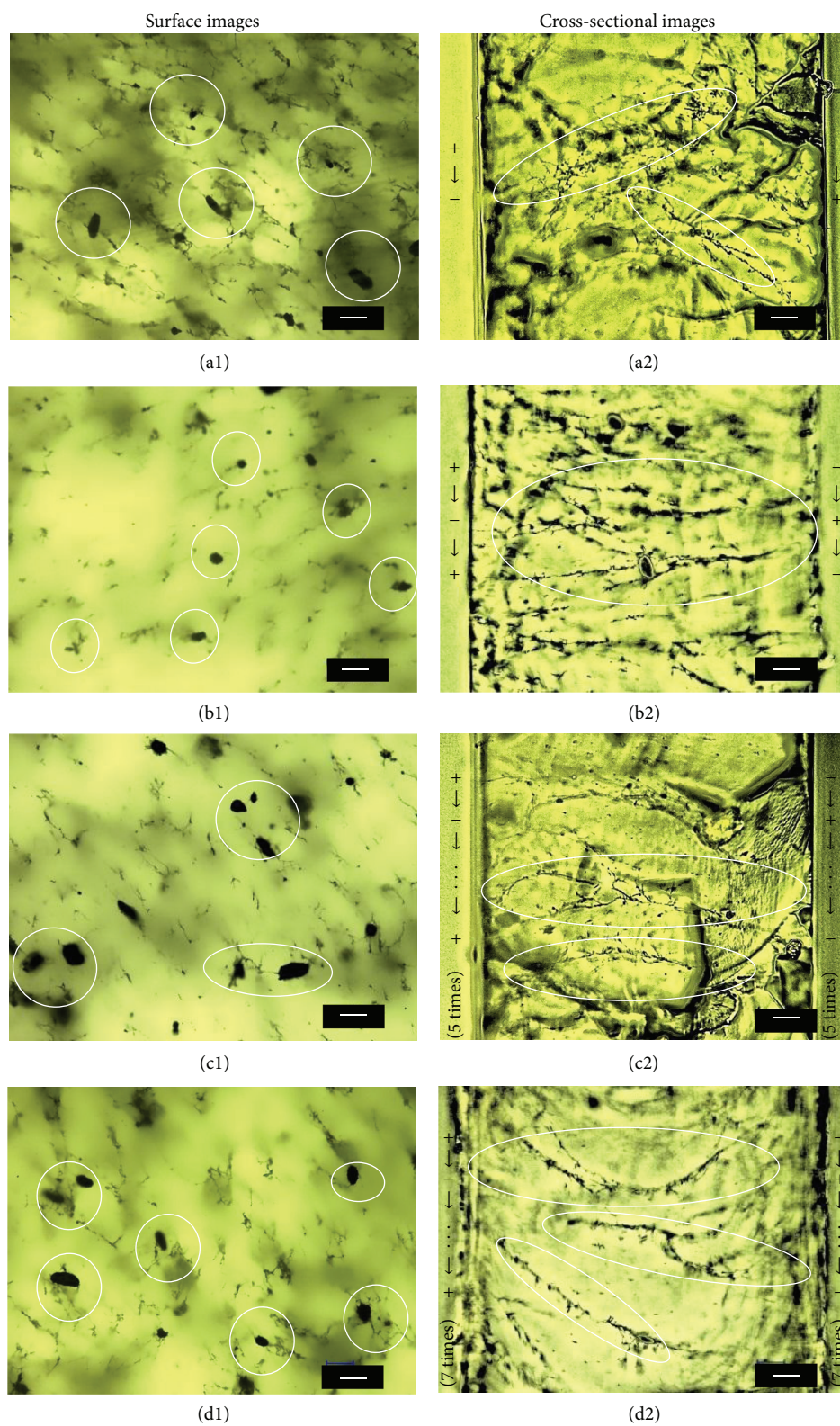


FIGURE 4: Digital micrographs of polysiloxane/CNT nanocomposites prepared for DC fields with different switching intervals (CNT: 0.05 vol%; scale bar: 20 μm); (a) SWDC50V_8 h, (b) SWDC50V_4 h, (c) SWDC50V_2 h 40 min, and (d) SWDC50V_2 h.

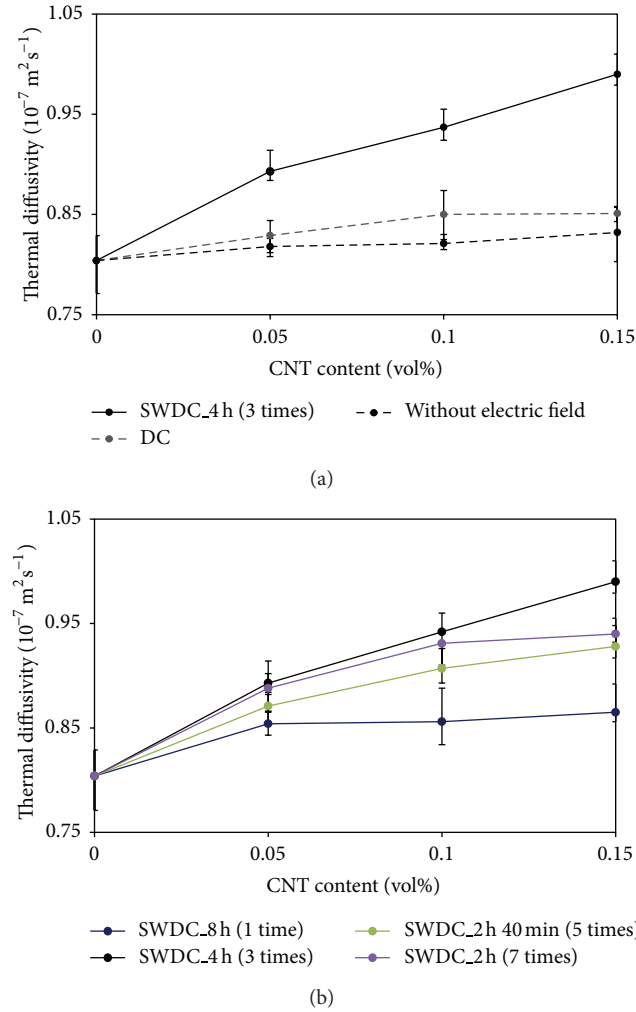


FIGURE 5: Thermal diffusivities of nanocomposites as a function of CNT content under (a) different electric fields and (b) switching DC times.

an 8 h interval, the LACNT tips are located on the right-hand side surface of the film where the positive electrode was located (Figure 4(a1)). With increasing switching interval, the thickness of ramified LACNTs that anchor the film surfaces is increased (Figures 4(b2)–4(d2)). The cross-sectional images indicate that the reduction in the number of LACNTs is directly related to the increase in the LACNT thickness. This implies that LACNTs with low CNT densities were incorporated in neighboring LACNTs, resulting in the formation of LACNTs with a higher CNT density. The darker and thicker domains of CNT agglomerates in the surface images also indicate that the CNT concentration of LACNTs increases with increasing DC switching interval. The CNT density of agglomerates was the highest for switching DC (SWDC) of 8 h (Figure 4(b1)). However, the CNT concentration started to decrease with increasing switching time, resulting in denser CNT agglomerates.

The thermal diffusivity was measured to investigate the cause of the variation in LACNT structures fabricated under different electric fields (Figure 5). The thermal diffusivity

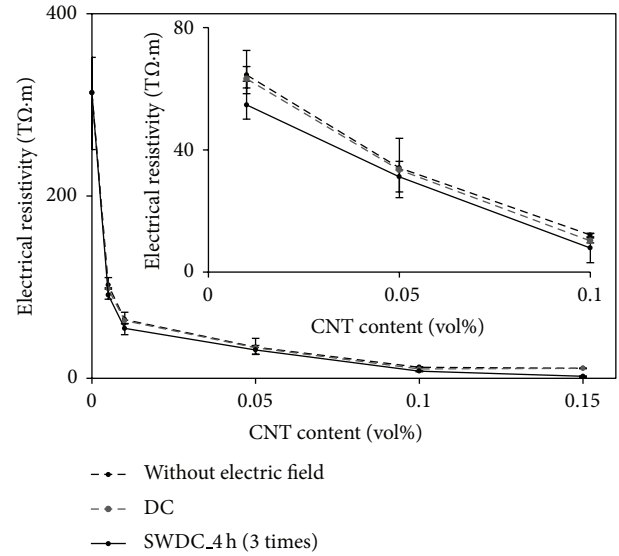


FIGURE 6: Electrical resistivities of nanocomposites as a function of CNT content under different electric fields (inset: magnification of resistivity responses between 0 and 0.1 vol% of CNT content).

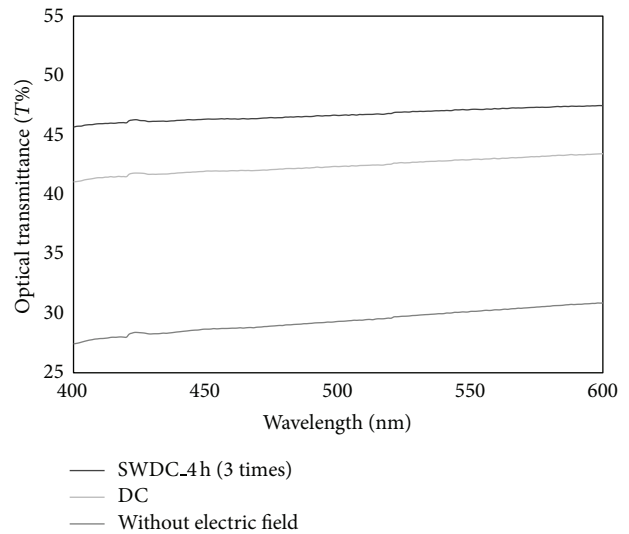


FIGURE 7: UV-Vis transmittance of nanocomposites under different electric fields (CNT: 0.05 vol%).

of each nanocomposite film was measured five times and the average value was obtained. Two different electric field structures were applied: one involving the application of a DC field or a switching DC field (Figure 5(a)) and the other involving varying the switching interval during application of a switching DC field (Figure 5(b)). The thermal diffusivity increased proportionally with increasing CNT content for both DC and switching DC fields (Figure 5(a)). The diffusivity was enhanced by a factor of almost five times when a switching DC field and no electric field were applied compared to when a DC field and no electric field were applied. This enhancement in the thermal diffusivity on the application of a switching DC field is related to the variation

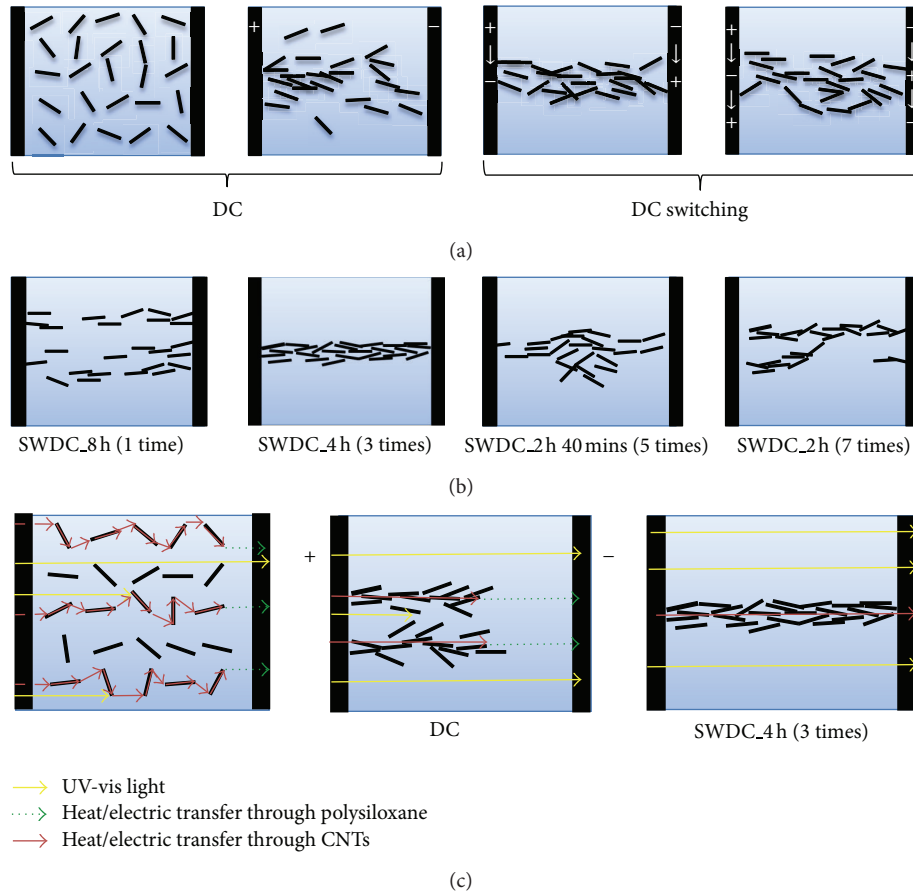


FIGURE 8: Illustration for mechanisms for (a) fabricating LACNTs with densely packed CNT gap induced by switching DC field, (b) optimizing LACNTs as a function of switching DC interval, and (c) enhancing optical, thermal, and electrical properties by LACNTs.

in the LACNT structure. As Figure 3 shows, when a DC electric field is applied, CNT fillers have dendritic structures and are localized on the anode side so that they do not anchor the composite surfaces. On switching the electric field, this dendritic CNT structure develops into network structures that consist of densely packed LACNTs, which anchor the composite surfaces; this occurs even when the same amounts of CNTs are used. This implies that the closely packed CNTs in the LACNTs are responsible for the large enhancement in the thermal diffusivity since they form high thermal conductivity paths.

Figure 5 shows the variation in the thermal diffusivity of the composites for different DC field switching intervals. The nanocomposite films fabricated by switching the DC field three times exhibited the highest thermal diffusivity. The thermal diffusivity increased in the order: once < five times < seven times < three times. These thermal diffusivities are higher than those obtained by the DC electric field. The thermal diffusivity did not increase proportionally with the switching interval. This may be explained in terms of the plane and cross-sectional images of the composites shown in Figure 4. With increasing switching interval, the LACNT thickness increased and the number of CNTs in a single LACNT bundle increased. However, too frequent switching

of the DC field induced partial breakup of the LACNTs during reassembling, as the cross-sectional images in Figures 4(c2) and 4(d2) show. This may be due to the variation in the viscosity of the prepolymer mixture as a function of time (Figure 2). The gradual increase in the viscosity will result in the fabrication of denser, thicker LACNTs in the polymer matrix, which will require longer to realize close filler-to-filler attachment. If the DC field is switched before the LACNTs are fabricated, the linear structure will break due to the increased viscosity of the matrix. This will reduce the Coulombic attraction due to the large increase in the polymer viscosity.

Figure 6 shows the effects of the LACNTs on the electric resistivity of the composite films. Despite only adding a very small amount (0.15 vol.%) of CNTs, the linear structure reduced the resistivity to $2.14 \text{ T}\Omega\cdot\text{m}$ due to the formation of densely packed LACNTs. This resistivity is comparable to that ($11.0 \text{ T}\Omega\cdot\text{m}$) of the composite film fabricated without application of an electric field. A conducting polymer composite requires a resistivity of at least $\sim 0.1 \text{ M}\Omega\cdot\text{m}$ [40, 41], whereas the electrical conductivity of the present composites is in the range of an insulator. However, the electrical conductivity varied over several orders of magnitude and is highly sensitive to the applied electric field and the CNT content (Figure 6).

This means that the fabrication of densely packed linear structures with conducting CNTs simultaneously enhances the thermal diffusivity and the electrical conductivity.

The LACNTs also affect the optical properties of the composites, as indicated by the variation in the optical transmittance shown in Figure 7. A homogeneous dispersion of CNTs in the polymer matrix obtained when no electric field was applied gave the lowest transmittance. The composite films oriented by applying DC and switching DC electric fields had higher transmittances. Visible light introduced from one surface of the film will either be absorbed or scattered in a different direction when it encounters a surface of an inorganic nanofiller in the polymer matrix. The formation of a linear dendritic or network structure by CNT movement can be induced by the combination of Coulombic attraction and electrophoresis in a polymer [20]. The CNTs that migrate leave spaces in the polymer matrix, which permit UV and visible light to transmit through the film planes.

Figure 8 illustrates the mechanisms for (a) fabricating LACNTs with densely packed CNTs under a switching DC field, (b) optimizing LACNTs by varying the DC switching interval, and (c) enhancing the thermal, electrical, and optical properties using LACNTs. When a DC electric field is applied, the longitudinal ends of the conducting 1D nanofillers are depolarized [16] and fillers with high aspect ratios orient their longitudinal ends parallel to the direction of the electric flux to realize electrical stabilization [24] (see Figure 8(a)). For a low-viscosity prepolymer such as polysiloxane, the oriented CNTs start to move toward the positive electrode by electrophoresis. At the same time, the depolarized ends of the CNTs will be attracted to each other by Coulombic attraction resulting in end-to-end attachment [24], which will facilitate the formation of linear dendritic or network structures of CNTs on application of an electric field. By repeatedly switching the DC field, the LACNTs with low CNT densities will be attracted to each other. CNTs that do not form LACNTs during previous application of a DC electric field will join to form denser LACNTs due to Coulombic attraction. Repeated switching will result in the formation of LACNT-to-LACNT interconnections, changing the linear structure from a dendritic structure to a network structure, as the cross-sectional images in Figures 4(b)–4(d) show. These interconnections between groups of LACNTs may give rise to a narrower filler-to-filler attachment in the polymer, if the prepolymer viscosity is kept constant. However, the prepolymer viscosity typically increases abruptly over a short time as polymerization proceeds, as shown in Figure 2. (Note that the rate of increase of the viscosity in Figure 2 is over four times higher than that of an actual experimental setup, which is performed in a sealed container with no exposure to air when the electric field is applied. The test data is presented to show the tendency of the polymer viscosity to vary with cross-linking.) Consequently, excessive switching of the DC field will reduce the number of LACNTs (see Figure 8(b)), especially when DC field switching occurs as the viscosity of the polymer matrix is increasing. This implies that it is necessary to optimize the DC switching interval relative to the variation of the viscosity of the prepolymer matrix. Modifying the CNT surface can cause the linear structure

to develop into a denser bundle structure [37], as has been demonstrated by cycling the electric field on and off in tetrahydrofuran [20]. Orientating conducting fillers parallel to the heat flux enhances the thermal conduction relative to a random distribution [10] because it increases the number of heat conduction paths through the conducting filler. Such enhancement of the thermal and electrical conductivities and the optical transmittance can be realized by fabricating linear LACNTs and by developing structures that anchor film surfaces by realizing dense packing, as illustrated in Figure 8(c). Fabricating densely packed LACNTs by switching a DC field can increase the thermal and electrical conductivities while using less filler than conventional methods.

4. Conclusion

Densely packed LACNTs were fabricated in a polymer-based nanocomposite film by applying and modulating DC electric fields. Linear-assembly of CNTs was demonstrated through Coulombic attraction and electrophoresis by controlling the viscosity of the prepolymer mixture. The application of a switching DC field caused the linear structures to form densely packed structures. On the application of a DC field, the CNT fillers formed a dendritic structure, which developed into densely packed LACNTs when the direction of the DC electric field was switched at a controlled switching interval. The resulting LACNTs enhanced the thermal and electrical conductivities and the optical transmittance of the polysiloxane/CNT nanocomposites. It is thus a promising technique for fabricating polymer-based materials with high thermal and electrical conductivities without using surface modification or increasing the conducting filler content.

Acknowledgments

The authors are grateful for support from the New Energy and Industrial Technology Development Organization (NEDO) of Japan, the Ultra Composite Material Technology Development Project (“Ultra Composite”), and the Global Research Lab. (GRL) Program of the National Research Foundation of Korea (NRF) funded by the Ministry of Education, Science and Technology (MEST) of Korea (Grant no. 2010-00339).

References

- [1] V. Choudhary and A. Gupta, “Polymer/carbon nanotube nanocomposites,” in *Carbon Nanotubes—Polymer Nanocomposites*, S. Yellampalli, Ed., Intech, 2011.
- [2] W. S. Lee and J. Yu, “Comparative study of thermally conductive fillers in underfill for the electronic components,” *Diamond and Related Materials*, vol. 14, no. 10, pp. 1647–1653, 2005.
- [3] J. Deng, X. Ding, W. Zhang et al., “Carbon nanotube-polyaniline hybrid materials,” *European Polymer Journal*, vol. 38, no. 12, pp. 2497–2501, 2002.
- [4] B. S. Shim, J. Starkovich, and N. Kotov, “Multilayer composites from vapor-grown carbon nano-fibers,” *Composites Science and Technology*, vol. 66, no. 9, pp. 1171–1178, 2006.
- [5] Z. M. Huang, Y. Z. Zhang, M. Kotaki, and S. Ramakrishna, “A review on polymer nanofibers by electrospinning and their

- applications in nanocomposites," *Composites Science and Technology*, vol. 63, no. 15, pp. 2223–2253, 2003.
- [6] H. B. Cho, T. Nakayama, T. Suzuki et al., "Linear assemblies of BN nanosheets, fabricated in polymer/BN nanosheet composite film," *Journal of Nanomaterials*, vol. 2011, Article ID 693454, 7 pages, 2011.
- [7] S. Kemalolu, G. Ozkoc, and A. Aytac, "Properties of thermally conductive micro and nano size boron nitride reinforced silicon rubber composites," *Thermochimica Acta*, vol. 499, no. 1–2, pp. 40–47, 2010.
- [8] X. L. Xie, Y. W. Mai, and X. P. Zhou, "Dispersion and alignment of carbon nanotubes in polymer matrix: a review," *Materials Science and Engineering R*, vol. 49, no. 4, pp. 89–112, 2005.
- [9] Y. S. Song and J. R. Youn, "Influence of dispersion states of carbon nanotubes on physical properties of epoxy nanocomposites," *Carbon*, vol. 43, no. 7, pp. 1378–1385, 2005.
- [10] Z. Han and A. Fina, "Thermal conductivity of carbon nanotubes and their polymer nanocomposites: a review," *Journal of Nanomaterials*, vol. 36, no. 7, pp. 914–944, 2011.
- [11] W. Zhao, H. Wang, H. Tang, and G. Chen, "Facile preparation of epoxy-based composite with oriented graphite nanosheets," *Polymer*, vol. 47, no. 26, pp. 8401–8405, 2006.
- [12] W. Zhou, S. Qi, H. Li, and S. Shao, "Study on insulating thermal conductive BN/HDPE composites," *Thermochimica Acta*, vol. 452, no. 1, pp. 36–42, 2007.
- [13] E. Logakis, C. H. Pandis, P. Pissis, J. Pionteck, and P. Pötschke, "Highly conducting poly(methyl methacrylate)/carbon nanotubes composites: investigation on their thermal, dynamic-mechanical, electrical and dielectric properties," *Composites Science and Technology*, vol. 71, no. 6, pp. 854–862, 2011.
- [14] H. B. Cho, T. Nakayama, T. Suzuki et al., "Formation and structural characteristic of perpendicularly aligned boron nitride nanosheet bridges in polymer/boron nitride composite film and its thermal conductivity," *Japanese Journal of Applied Physics*, vol. 50, no. 1, Article ID 01BJ05, 2011.
- [15] M. H. Al-Saleh and U. Sundararaj, "A review of vapor grown carbon nanofiber/polymer conductive composites," *Carbon*, vol. 47, no. 1, pp. 2–22, 2009.
- [16] J. Lu, W. Weng, X. Chen, D. Wu, C. Wu, and G. Chen, "Piezoresistive materials from directed shear-induced assembly of graphite nanosheets in polyethylene," *Advanced Functional Materials*, vol. 15, no. 8, pp. 1358–1363, 2005.
- [17] N. Toyohara, Y. Benino, T. Fujiwara et al., "Enhancement and depression in second-order optical nonlinearity of $\text{Ba}_2\text{TiGe}_2\text{O}_8$ in crystallized glass prepared in a high magnetic field," *Journal of Applied Physics*, vol. 99, no. 4, 2006.
- [18] X. Q. Chen, T. Saito, H. Yamada, and K. Matsushige, "Aligning single-wall carbon nanotubes with an alternating-current electric field," *Applied Physics Letters*, vol. 78, no. 23, pp. 3714–3716, 2001.
- [19] T. Takahashi, T. Murayama, A. Higuchi, H. Awano, and K. Yonetake, "Aligning vapor-grown carbon fibers in polydimethylsiloxane using dc electric or magnetic field," *Carbon*, vol. 44, no. 7, pp. 1180–1188, 2006.
- [20] P. V. Kamat, K. G. Thomas, S. Barazzouk, G. Girishkumar, K. Vinodgopal, and D. Meisel, "Self-assembled linear bundles of single wall carbon nanotubes and their alignment and deposition as a film in a dc field," *Journal of the American Chemical Society*, vol. 126, no. 34, pp. 10757–10762, 2004.
- [21] T. Saotome, H. Kim, D. Lashmore et al., "Transparent conducting film: effect of mechanical stretching to optical and electrical properties of carbon nanotube mat," *Bulletin of Materials Science*, vol. 34, no. 4, pp. 615–622, 2011.
- [22] K. Mylvaganam and L. C. Zhang, "Fabrication and application of polymer composites comprising carbon nanotubes," *Recent Patents on Nanotechnology*, vol. 1, no. 1, pp. 59–65, 2007.
- [23] Y. Zhang, A. Chang, J. Cao et al., "Electric-field-directed growth of aligned single-walled carbon nanotubes," *Applied Physics Letters*, vol. 79, no. 19, pp. 3155–3157, 2001.
- [24] C. A. Martin, J. K. W. Sandler, A. H. Windle et al., "Electric field-induced aligned multi-wall carbon nanotube networks in epoxy composites," *Polymer*, vol. 46, no. 3, pp. 877–886, 2005.
- [25] L. Chen, G. Chen, and L. Lu, "Piezoresistive behavior study on finger-sensing silicone rubber/graphite nanosheet nanocomposites," *Advanced Functional Materials*, vol. 17, no. 6, pp. 898–904, 2007.
- [26] S. Iijima, "Helical microtubules of graphitic carbon," *Nature*, vol. 354, no. 6348, pp. 56–58, 1991.
- [27] R. Khare and S. Bose, "Carbon nanotube based composites—a review," *Journal of Minerals & Materials Characterization & Engineering*, vol. 4, pp. 31–46, 2005.
- [28] A. L. Kalamkarov, A. V. Georgiades, S. K. Rokkam, V. P. Veedu, and M. N. Ghasemi-Nejhad, "Analytical and numerical techniques to predict carbon nanotubes properties," *International Journal of Solids and Structures*, vol. 43, no. 22–23, pp. 6832–6854, 2006.
- [29] J. P. Salvétat-Delmotte and A. Rubio, "Mechanical properties of carbon nanotubes: a fiber digest for beginners," *Carbon*, vol. 40, no. 10, pp. 1729–1734, 2002.
- [30] R. S. Ruoff, D. Qian, and W. K. Liu, "Mechanical properties of carbon nanotubes: theoretical predictions and experimental measurements," *Comptes Rendus Physique*, vol. 4, no. 9, pp. 993–1008, 2003.
- [31] F. Deng, Q. S. Zheng, L. F. Wang, and C. W. Nan, "Effects of anisotropy, aspect ratio, and nonstraightness of carbon nanotubes on thermal conductivity of carbon nanotube composites," *Applied Physics Letters*, vol. 90, no. 2, Article ID 021914, 2007.
- [32] M. J. Biercuk, M. C. Llaguno, M. Radosavljevic, J. K. Hyun, A. T. Johnson, and J. E. Fischer, "Carbon nanotube composites for thermal management," *Applied Physics Letters*, vol. 80, no. 15, pp. 2767–2769, 2002.
- [33] J. I. Paredes and M. Burghard, "Dispersions of individual single-walled carbon nanotubes of high length," *Langmuir*, vol. 20, no. 12, pp. 5149–5152, 2004.
- [34] Z. Ounaies, C. Park, K. E. Wise, E. J. Siochi, and J. S. Harrison, "Electrical properties of single wall carbon nanotube reinforced polyimide composites," *Composites Science and Technology*, vol. 63, no. 11, pp. 1637–1646, 2003.
- [35] J. Sandler, M. S. P. Shaffer, T. Prasse, W. Bauhofer, K. Schulte, and A. H. Windle, "Development of a dispersion process for carbon nanotubes in an epoxy matrix and the resulting electrical properties," *Polymer*, vol. 40, no. 21, pp. 5967–5971, 1999.
- [36] O. Breuer and U. Sundarara, "Big returns from small filber: a review of polymer/carbon nanotube composites," *Polymer Composites*, vol. 25, pp. 630–641, 2004.
- [37] M. Senthil Kumar, T. H. Kim, S. H. Lee et al., "Influence of electric field type on the assembly of single walled carbon nanotubes," *Chemical Physics Letters*, vol. 383, no. 3–4, pp. 235–239, 2004.
- [38] T. Prasse, J. Y. Cavallé, and W. Bauhofer, "Electric anisotropy of carbon nanofibre/epoxy resin composites due to electric field

- induced alignment,” *Composites Science and Technology*, vol. 63, no. 13, pp. 1835–1841, 2003.
- [39] H. B. Cho, T. Nakayama, Y. Tokoi et al., “Facile preparation of a polysiloxane-based hybrid composite with highly-oriented boron nitride nanosheets and an unmodified surface,” *Composites Science and Technology*, vol. 70, no. 12, pp. 1681–1686, 2010.
- [40] C. Zhang, P. Wang, C. A. Ma, G. Wu, and M. Sumita, “Temperature and time dependence of conductive network formation: dynamic percolation and percolation time,” *Polymer*, vol. 47, no. 1, pp. 466–473, 2006.
- [41] H. Tintang, J. Y. Ong, C. L. Loh et al., “Using oxidation to increase the electrical conductivity of carbon nanotube electrodes,” *Carbon*, vol. 47, no. 7, pp. 1867–1870, 2009.

Research Article

UV-Ozone Treatment on Cs_2CO_3 Interfacial Layer for the Improvement of Inverted Polymer Solar Cells

Yusheng Xin, Zixuan Wang, Lu Xu, Xiaowei Xu, Yang Liu, and Fujun Zhang

Key Laboratory of Luminescence and Optical Information of Ministry of Education, Beijing Jiaotong University, Beijing 100044, China

Correspondence should be addressed to Fujun Zhang; fjzhang@bjtu.edu.cn

Received 11 November 2012; Revised 24 December 2012; Accepted 4 January 2013

Academic Editor: Jian Wei

Copyright © 2013 Yusheng Xin et al. This is an open access article distributed under the Creative Commons Attribution License, which permits unrestricted use, distribution, and reproduction in any medium, provided the original work is properly cited.

Inverted configuration polymer solar cells (IPSCs) were prepared by using Cs_2CO_3 modified indium tin oxide (ITO) substrates as cathode and MoO_3/Al as anode, ITO/ Cs_2CO_3 /P3HT:PCBM/ MoO_3/Al . The interfacial Cs_2CO_3 layers were conducted with annealing treatment and different time UV-Ozone treatment. The power conversion efficiency (PCE) of IPSCs was improved to 1% when the UV-Ozone treatment time is 15 minutes, with the open-circuit voltage of 0.48 V, short-circuit current density of 5.4 mA/cm², and fill factor of 39%. The improvement of IPSCs should be attributed to the increased electron transporting and collection ability of Cs_2CO_3 layer induced by UV-Ozone treatment. The underlying mechanism of PCE improvement was discussed in terms of series and shunt resistance of cells induced by UV-Ozone treatment on Cs_2CO_3 layer, and the mole ratio of Cs to O of Cs_2CO_3 layer with different UV-Ozone treatment was investigated by scanning electron microscopy operating in the mode for in situ energy dispersive X-ray (EDX) spectra.

1. Introduction

Polymer solar cells (PSCs) have attracted more and more attention as next-generation solar cells, owing to their merits of flight weight, lower cost, and friendly environments [1–3]. The power conversion efficiency (PCE) of organic solar cells has undergone a more than tenfold increase from ~1.0% by Tang in 1986 to ~10% in 2012 announced by Heliatek GmbH [4]. Along with the PCE increase of PSCs, the stability of PSCs is another key parameter for its application. The conventional structure PSCs are commonly prepared on indium tin oxide (ITO) substrates or ITO coated with poly(3,4-ethylenedioxythiophene):poly(styrene sulfonate) (PEDOT:PSS) substrates as anode and low work function metals as top cathode [5, 6]. However, metals with low work function are not very stable as the top electrode due to their sensitivity to oxygen and moisture in air. In order to improve the stability of PSCs, inverted configuration PSCs were designed with low work function materials modified ITO as the transparent cathode and a high work function metal as anode, which could effectively avoid the device degradation induced by the contamination

of metal cathodes. Liao et al. demonstrate a highly efficient inverted bulk heterojunction PSCs based on regioregular poly(3-hexylthiophene):[6,6]-phenylC61 butyric acid methyl ester (PC₆₀BM) with a low temperature annealed interfacial buffer layer, cesium carbonate (Cs_2CO_3). This approach improves the power conversion efficiency of IPSCs from 2.3% to 4.2% [7]. Recently, Shim et al. reported inverted tandem PSCs with two identical active layers comprising a donor (P3HT) and a fullerene derivative acceptor PC₆₀BM, and the PCE of inverted tandem PSCs arrives to about 2.1% [8]. The most commonly used material system for PSCs consists of conjugated polymers as the electron donor and fullerene derivatives as the electron acceptor materials, blended in a bulk heterojunction (BHJ) to overcome the strong excitonic behavior of photogenerated charge carriers. The interpenetrated network of the donor-acceptor blend in the BHJ structure provides charge separation and charge transportation properties for achieving high efficiency. It is imperative that a bicontinuous network with a domain width approximately twice that of the exciton diffusion length and a high donor/acceptor interface is formed, which favors the exciton dissociation and transport of the separated charges to

the respective electrode. The active layer could be easily prepared by spin coating, inkjet printing, spray coating, gravure coating, and roller casting, which makes them feasible for preparing large scale PSCs [9, 10]. The main factors limiting the PSCs and IPSCs performance could be summarized as follows [11–13]: (i) incomplete solar spectrum absorption, (ii) thermalization of hot carriers (or excitons) in the form of excess heat, (iii) chemical potential (thermodynamic) losses dictating that the photovoltage must be less than band gap (E_G) for relaxed carriers, (iv) radiative recombination during charge carrier transport, and (v) the presence of other nonradiative losses.

Some effective methods were carried out to improve the performance of PSCs, such as thermal treatment, solvent treatment, adding additives, and inserting ultrathin buffer layers [14–19]. Sun and coworkers reported that PCE of the IPSCs based on P3HT: indene- C_{70} bisadduct was improved from 5.80% for the device without the additive to 6.35% for the device with 3-hexylthiophene additive and to 6.69% with 3-methylthiophene additive [17]. Oo et al. successfully exploited solution processed, high electron mobility and highly transparent zinc tin oxide (ZTO) as electron transporting buffer layer in IPSCs of FTO/ZTO/P3HT:PCBM/ WO_3/Ag . The PCE of 3.05% was achieved, which was attributed to a better electron transporting, hole blocking capacities, and reduced recombination probabilities at electron collecting electrode with ZTO layer [19]. Park and his coworkers reported a facile and effective treatment method for controlling the morphology of bulk heterojunction (BHJ) structured polymer-based solar cells (PSCs) using a gas-assisted spray (g-spray) technique [20]. In order to achieve highly efficient IPSCs, it is critical to improve the electron collection of modified ITO electrode as well as suppress its hole collection. For IPSCs, the order of the layers is reversed with the top metal electrode now being the hole collecting anode. Low work function metals or metal oxidation, such as calcium, ZnO or Cs_2CO_3 , are typically used to modified ITO substrates, and higher work function metals or metal oxidation, such as silver, gold, or MoO_3/Al , are selected as top anode in the IPSCs [21–24]. In this paper, we investigated the different UV-Ozone treatment time on the buffer layer Cs_2CO_3 on the effect of IPSCs performance.

2. Experimental Details

The indium tin oxide (ITO) glass substrates (sheet resistance $15 \Omega/\square$) were cleaned consecutively in ultrasonic baths containing acetone, ethanol, and deionized water and dried by high pure nitrogen gas. The cleaned ITO substrates were treated by UV-Ozone for 10 min. The Cs_2CO_3 was dissolved in 2-ethoxyethanol or deionized water with the concentration 1 mg/mL and then spin-coated onto the ITO substrates at the speed of 4000 rpm for 40 seconds. The ITO substrates coated with Cs_2CO_3 thin film were transferred to a hot plate and annealed at $150^\circ C$ for 20 min. Parts of Cs_2CO_3 -coated ITO substrates were treated by UV-Ozone with different time. Polymer electron donor P3HT and electron acceptor PC₆₀BM were dissolved in chloroform with concentration 20 mg/mL, respectively, and then blended together with the

same weight ratio. The blended solution was spin coated on Cs_2CO_3 coated ITO substrates at the speed of 2000 rpm for 30 seconds. The substrates coated with active layers were transferred to a vacuum chamber, and a 5 nm thickness layer of MoO_3 was deposited on the active layer under 5×10^{-3} Pa vacuum. The film thickness was monitored by a quartz crystal microbalance. The aluminum (Al) cathode with the thickness of 100 nm and the active area about 0.1 cm^2 defined through foursquare shadow mask was evaporated under 5×10^{-3} Pa conditions. The prepared IPSCs (ITO/ Cs_2CO_3 /P3HT:PCBM/ MoO_3 (5 nm)/Al) were carried out postannealing treatment under $120^\circ C$ for 10 min.

The absorption spectra were measured by Shimadzu UV-3101 PC spectrometer. The current-voltage characteristics of IPSCs were measured by a Keithley source meter 2410 in dark and under illumination at 100 mW/cm^2 by using a 150 W Xenon lamp. The morphology of thin films was characterized by scanning electron microscope (SEM). The schematic diagrams of inverted configuration polymer solar cells and its energy level alignment are shown in Figure 1.

3. Results and Discussion

The absorption spectra of P3HT, PCBM, pristine P3HT:PCBM, and annealed P3HT:PCBM film are shown in the Figure 2. The electron donor material P3HT has a relative large absorption range from 450 nm to 600 nm, and its absorption peak locates at 517 nm. The electron acceptor material PCBM has a strong absorption peak at 300 nm and a weak absorption range from 400 nm to 550 nm. The blended P3HT:PCBM films show a distinguished blue shift of absorption peak at 480 nm compared with 517 nm of neat P3HT films. After annealing treatment on the blended film by $120^\circ C$ with 10 min, the main absorption peak shifts to the 510 nm, and a shoulder absorption peak at 603 nm was observed. The variation of blended P3HT:PCBM absorption spectra should be attributed to the increased order phase of P3HT induced by annealing treatment, which was demonstrated by our pervious works and other groups [25–28].

All the inverted configuration polymer solar cells have the same cell configuration of ITO/ Cs_2CO_3 /P3HT:PCBM/ MoO_3/Al ; the only difference of each cell is UV-Ozone treatment time on Cs_2CO_3 interfacial layer. It was reported that Cs_2CO_3 decomposes into stoichiometric Cs_2O doped with Cs_2O_2 during thermal evaporation [29]. Liao and coworkers reported that the work function of annealed Cs_2CO_3 layer decreases from 3.45 to 3.06 eV by ultraviolet photoelectron spectroscopy [30]. The work function reduction could be attributed to this doped cesium oxide that behaves as a n-type semiconductor, with a lower interface resistance than pristine Cs_2CO_3 . The ITO/ Cs_2CO_3 was used as cathode to collect electron from the active layer. The MoO_3/Al was used as anode to collect hole from the active layer. The insertion of MoO_3 layer was found to be critical to the device performance, effectively extracting holes to prevent the exciton quenching and reducing the interfacial resistance because of alignment of energy levels [31]. It was demonstrated that ultrathin MoO_3 layer may form a tunneling

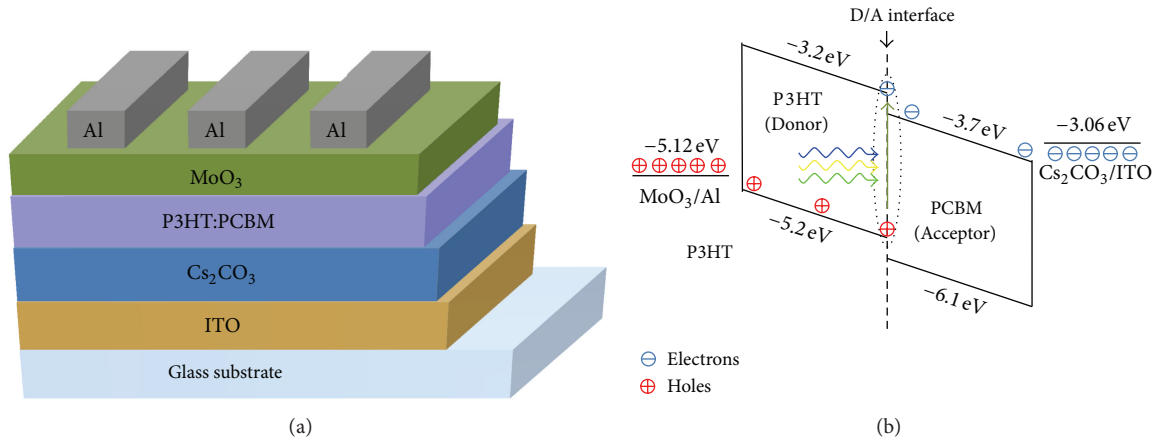


FIGURE 1: Schematic diagram of inverted configuration polymer solar cells and its energy level alignment.

TABLE 1: The key parameters of fabricated inverted polymer solar cells.

Number	Times	J_{sc} (mA/cm ²)	V_{oc} (V)	R_{sh} (Ω -cm ²)	R_s (Ω -cm ²)	FF %	PCE %
1	0 min	4.0	0.58	266	88	33	0.76
2	5 min	4.5	0.51	215	85	31	0.71
3	10 min	5.0	0.49	239	69	32	0.78
4	15 min	5.4	0.48	345	47	39	1.01
5	20 min	3.7	0.39	136	95	27	0.39

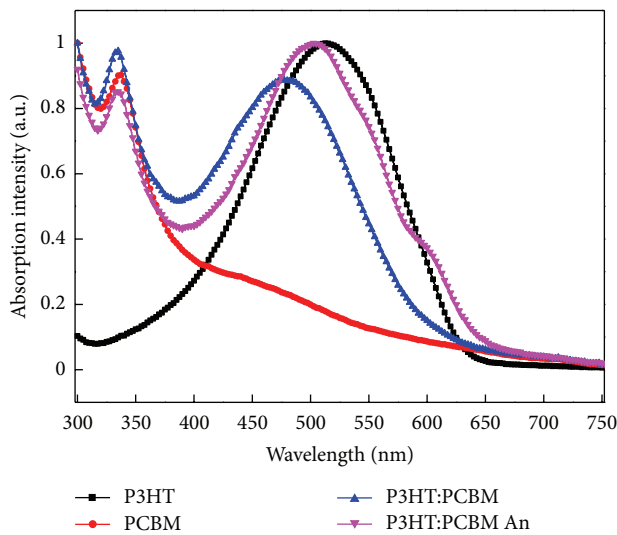


FIGURE 2: The absorption spectra of P3HT, PCBM, and the blended films.

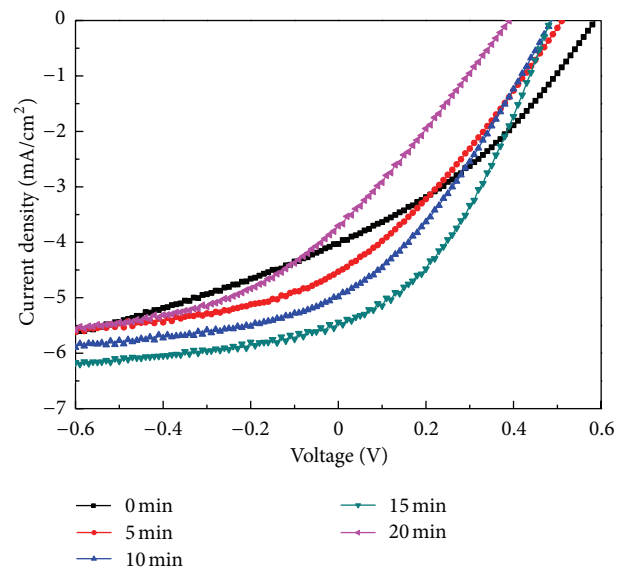


FIGURE 3: The J - V curves of IPSCs with different time UV-Ozone treatment on Cs_2CO_3 films under the illumination of $100 \text{ mW}/\text{cm}^2$.

junction to increase built-in electric field, an interfacial dipole layer to shift the work function of electrodes [32]. The IPSCs J - V characteristic curves dependence on the UV-Ozone treatment time on Cs_2CO_3 under $100 \text{ mW}/\text{cm}^2$ are shown in the Figure 3. All the key parameters of IPSCs, including open circuit voltage (V_{oc}), short circuit current density (J_{sc}), fill factor (FF), power conversion efficiency (PCE), shunt resistance (R_{sh}), and series resistance (R_s), are summarized in the Table 1.

The V_{oc} was monotonously decreased along with increase of UV-Ozone treatment time on Cs_2CO_3 layer. However, the J_{sc} was firstly increased and then decreased when the UV-Ozone treatment time goes beyond 15 minutes. The maximum PCE of IPSCs arrives to 1% when the Cs_2CO_3 layer was treated by UV-Ozone with 15 minutes, which resulted from the increased J_{sc} and FF, the decreased V_{oc} . It is known

TABLE 2: Element analysis of Cs_2CO_3 film with different time of UV-Ozone treatment.

Elements		O	Si	In	Sn	Cs	O/Cs (mol)
5 min	Wt %	22.31	22.41	31.29	2.07	21.92	8.45
	At %	52.68	30.14	10.30	0.66	6.23	
10 min	Wt %	26.95	26.21	25.50	2.04	19.29	11.59
	At %	56.11	31.08	7.40	0.57	4.84	
15 min	Wt %	22.37	27.91	28.93	3.21	17.57	10.56
	At %	49.88	35.45	8.99	0.97	4.72	
20 min	Wt %	46.44	27.26	12.71	0.85	12.75	30.22
	At %	71.02	23.75	2.71	0.18	2.35	

(Wt %: weight percent; At %: elemental mol percent; O/Cs: Mol ratio.)

that the three parameters are very sensitive to the variation of series resistance (R_s) and shunt resistance (R_{sh}). The R_s of solar cells depends on resistance of the semiconductor bulk, the metal electrodes, and the metal/semiconductor interfaces. The R_s of cells is a parasitic, power consuming parameter. It decreases the maximum achievable output power, and hence it softens the J - V characteristics of a solar cell in the fourth quadrant. As seen from Table 1, the FF is also increased from 33% to 39% along with the decrease of R_s from 88 to 47 $\Omega\text{-cm}^2$, which could be the enhancement of electronic coupling between the inorganic materials cesium oxides and active layer to mediate better forward charge transfer and reduce back charge recombination at the interface. The R_{sh} is relative to the recombination of charge carriers at the donor/acceptor interface and near electrodes. The R_{sh} was increased from 266 to 354 $\Omega\text{-cm}^2$, which decreased the charge recombination between the buffer layer and the active layer interface. The combined effect of the decreased R_s and increased R_{sh} on charge carrier transport and collection results in the increase of J_{sc} and the reverse current saturation.

The dark J - V characteristic curves of all IPSCs are shown in Figure 4. All the IPSCs with Cs_2CO_3 layer undergoing UV-Ozone treatment have shown remarkable diodes prosperities, high forward current, and very low reverse current. However, there is a "S" shape J - V curve in the forward bias region for the cells based on Cs_2CO_3 layer without UV-Ozone treatment, resulting in the limit of charge carriers transport and collection. It is very apparent that the reverse dark current was markedly increased when the Cs_2CO_3 layer was UV-Ozone treatment about 20 minutes, and the high dark current in the reverse bias region can be attributed to the leakage current in reverse bias mode, resulting in much more charge carrier interfacial recombination and the decrease of short circuit current density.

Figure 5 shows the SEM images of ITO substrate and Cs_2CO_3 film on ITO substrates, and it is apparent that snowflake-like morphology of Cs_2CO_3 was observed. However, the Cs_2CO_3 films could not completely covered ITO surfaces when the Cs_2CO_3 films were prepared under the low spin coating conditions (500 rpm). In order to further confirm the effect of Cs_2CO_3 film modified ITO substrates on the performance of IPSCs. The elemental analysis of thick Cs_2CO_3 film with different treatments, annealing treatment,

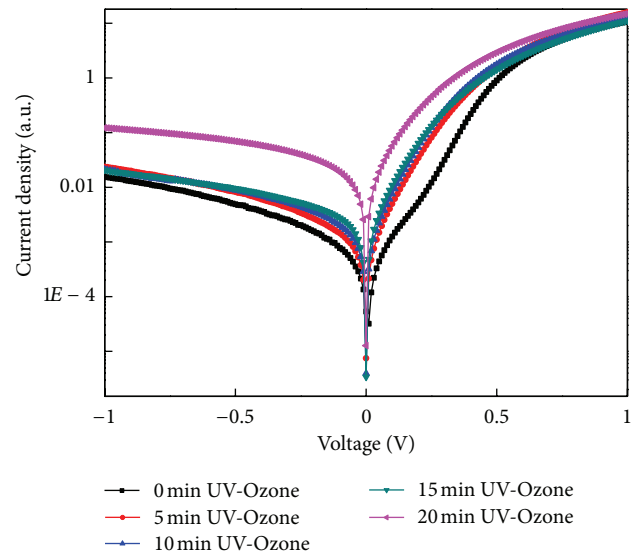


FIGURE 4: The J - V curves of IPSCs with different time UV-Ozone treatment on Cs_2CO_3 films in the dark.

and UV-Ozone treatment with different time was collected by SEM operating in the mode for in situ energy dispersive X-ray (EDX) spectra. The weight and mol percent of Si, O, Cs, In, and Sn elements were measured, and the mole ratio of O to Cs was summarized in the Table 2. The X-ray of In, Sn, O, and Si from ITO substrates could be collected due to the thin and discontinuous Cs_2CO_3 layer. Therefore, the relative ratio of Cs atom to O atom was simply discussed, which may be caused by UV-Ozone treatment on Cs_2CO_3 and the thickness of Cs_2CO_3 film and uncovered ITO surface.

4. Conclusions

A series of IPSCs based on the P3HT:PCBM as the active layer were fabricated with ITO/ Cs_2CO_3 as cathode and MoO_3/Al as anode. The performances of IPSCs were enhanced when the Cs_2CO_3 layer was treated by UV-Ozone with 15 minutes, which should be attributed to the enhancement of carrier transport and collection by Cs_2CO_3 layer. The maximum PCE of IPSCs arrives to 1% with the open circuit voltage of 0.48V,

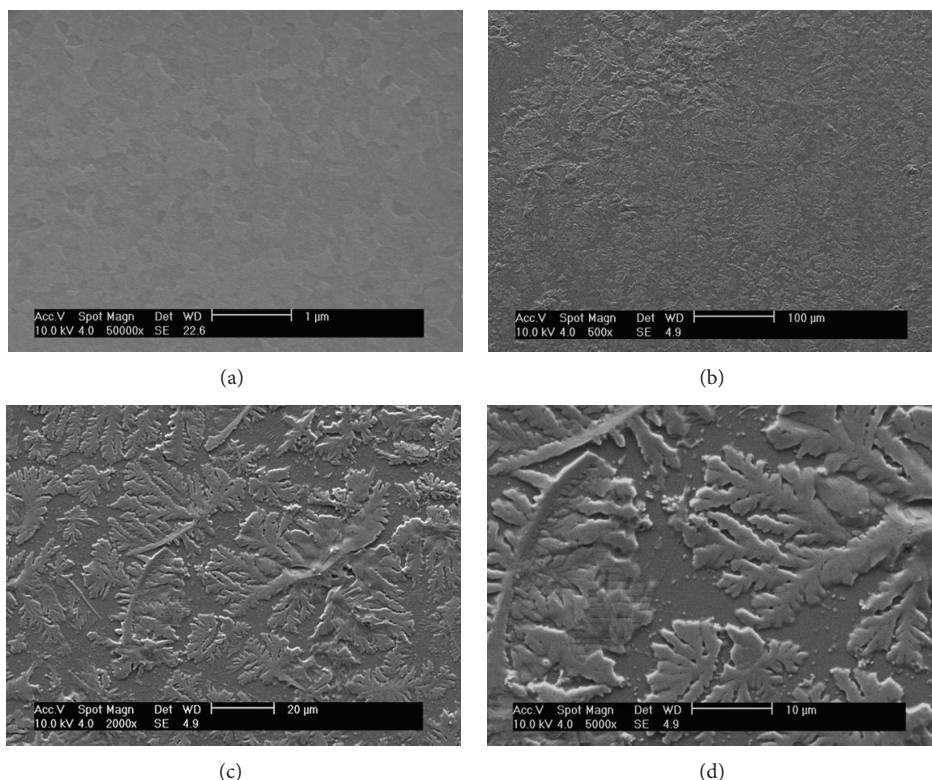


FIGURE 5: SEM pictures of (a) ITO surface, ((b)–(d)) Cs_2CO_3 films on ITO substrate with different magnification.

short circuit current density of 5.4 mA/cm^2 , and fill factor of 39%.

Acknowledgments

The authors express their thanks to Beijing Natural Science Foundation (2122050); Basic Research Foundation of the Central Universities (2013JBZ004). F. Zhang thanks the support from the State Key Laboratory of Catalysis, CAS.

References

- [1] N. J. Zhou, X. G. Guo, R. P. Ortiz et al., “Bithiophene imide and benzodithiophene copolymers for efficient inverted polymer solar cells,” *Advanced Materials*, vol. 24, no. 17, pp. 2242–2248, 2012.
- [2] H. Zhen, K. Li, Z. Huang et al., “Inverted indium-tin-oxide-free cone-shaped polymer solar cells for light trapping,” *Applied Physics Letters*, vol. 100, no. 21, Article ID 213901, 2012.
- [3] Y. Zhao, L. Zhu, J. Chen, and D. Ma, “Improving color stability of blue/orange complementary white OLEDs by using single-host double-emissive layer structure: comprehensive experimental investigation into the device working mechanism,” *Organic Electronics*, vol. 13, no. 8, pp. 1340–1348, 2012.
- [4] C. W. Tang, “Two-layer organic photovoltaic cell,” *Applied Physics Letters*, vol. 48, no. 2, pp. 183–185, 1986.
- [5] K. Sun, B. Zhao, V. Murugesan et al., “High-performance polymer solar cells with a conjugated zwitterion by solution processing or thermal deposition as the electron-collection interlayer,” *Journal of Materials Chemistry*, vol. 22, no. 45, pp. 24155–24165, 2012.
- [6] B.-Y. Ren, C.-J. Ou, C. Zhang et al., “Diarylfuorene-modified fulleropyrrolidine acceptors to tune aggregate morphology for solution-processable polymer/fullerene bulk-heterojunction solar cells,” *Journal of Physical Chemistry C*, vol. 116, no. 16, pp. 8881–8887, 2012.
- [7] H.-H. Liao, L.-M. Chen, Z. Xu, G. Li, and Y. Yang, “Highly efficient inverted polymer solar cell by low temperature annealing of Cs_2CO_3 interlayer,” *Applied Physics Letters*, vol. 92, no. 17, Article ID 173303, 2008.
- [8] J. W. Shim, Y. Zhou, C. Fuentes-Hernandez et al., “Studies of the optimization of recombination layers for inverted tandem polymer solar cells,” *Solar Energy Materials and Solar Cells*, vol. 107, pp. 51–55, 2012.
- [9] K. M. Coakley and M. D. McGehee, “Conjugated polymer photovoltaic cells,” *Chemistry of Materials*, vol. 16, no. 23, pp. 4533–4542, 2004.
- [10] F. Zhang, X. Xu, W. Tang et al., “Recent development of the inverted configuration organic solar cells,” *Solar Energy Materials and Solar Cells*, vol. 95, no. 7, pp. 1785–1799, 2011.
- [11] R. R. Lunt, T. P. Osedach, P. R. Brown, J. A. Rowehl, and V. Bulovic, “Practical roadmap and limits to nanostructured photovoltaics,” *Advanced Materials*, vol. 23, no. 48, pp. 5712–5727, 2011.
- [12] M. C. Hanna and A. J. Nozik, “Solar conversion efficiency of photovoltaic and photoelectrolysis cells with carrier multiplication absorbers,” *Journal of Applied Physics*, vol. 100, no. 7, Article ID 074510, 2006.

- [13] M. A. Green, K. Emery, Y. Hishikawa, and W. Warta, "Solar cell efficiency tables (version 37)," *Progress in Photovoltaics*, vol. 19, no. 1, pp. 84–92, 2011.
- [14] B. Peng, X. Guo, C. Cui, Y. Zou, C. Pan, and Y. Li, "Performance improvement of polymer solar cells by using a solvent-treated poly(3,4-ethylenedioxythiophene):poly(styrenesulfonate) buffer layer," *Applied Physics Letters*, vol. 98, no. 24, Article ID 243308, 2011.
- [15] J. S. Kim, W. S. Chung, K. Kim et al., "Performance optimization of polymer solar cells using electrostatically sprayed photoactive layers," *Advanced Functional Materials*, vol. 20, no. 20, pp. 3538–3546, 2010.
- [16] S.-H. Chan, C.-S. Lai, H.-L. Chen, C. Ting, and C.-P. Chen, "Highly efficient P₃HT: C60 solar cell free of annealing process," *Macromolecules*, vol. 44, no. 22, pp. 8886–8891, 2011.
- [17] Y. Sun, C. Cui, and H. Wang, "Efficiency enhancement of polymer solar cells based on poly(3-hexylthiophene)/indene-C₇₀ bisadduct via methylthiophene additive," *Advanced Energy Materials*, vol. 1, no. 6, pp. 1058–1061, 2011.
- [18] Z. Zhuo, F. Zhang, J. Wang et al., "Efficiency improvement of polymer solar cells by iodine doping," *Solid-State Electronics*, vol. 63, no. 1, pp. 83–88, 2011.
- [19] T. Z. Oo, R. Devi Chandra, N. Yantara, R. R. Prabhakar, L. H. Wong, and S. G. Mhaisalkar, "Zinc Tin Oxide (ZTO) electron transporting buffer layer in inverted organic solar cell," *Organic Electronics*, vol. 13, no. 5, pp. 870–874, 2012.
- [20] H. Y. Park, K. Kim, D. Y. Kim, S. K. Choi, S. M. Jo, and S. Y. Jang, "Facile external treatment for efficient nanoscale morphology control of polymer solar cells using a gas-assisted spray method," *Journal of Materials Chemistry*, vol. 21, no. 12, pp. 4457–4464, 2011.
- [21] X. Xu, F. Zhang, J. Zhang et al., "High efficient inverted polymer solar cells with different annealing treatment," *Materials Science and Engineering C*, vol. 32, no. 4, pp. 685–691, 2012.
- [22] F. J. Zhang, D. W. Zhao, Z. L. Zhuo, H. Wang, Z. Xu, and Y. S. Wang, "Inverted small molecule organic solar cells with Ca modified ITO as cathode and MoO₃ modified Ag as anode," *Solar Energy Materials and Solar Cells*, vol. 94, no. 12, pp. 2416–2421, 2010.
- [23] X. W. Sun, D. W. Zhao, L. Ke, A. K. K. Kyaw, G. Q. Lo, and D. L. Kwong, "Inverted tandem organic solar cells with a MoO₃/Ag/Al/Ca intermediate layer," *Applied Physics Letters*, vol. 97, no. 5, Article ID 053303, 2010.
- [24] A. K. K. Kyaw, X. W. Sun, C. Y. Jiang, G. Q. Lo, D. W. Zhao, and D. L. Kwong, "An inverted organic solar cell employing a sol-gel derived ZnO electron selective layer and thermal evaporated MoO₃ hole selective layer," *Applied Physics Letters*, vol. 93, no. 22, Article ID 221107, 2008.
- [25] Z.-L. Zhuo, F.-J. Zhang, X.-W. Xu, J. Wang, L.-F. Lu, and Z. Xu, "Photovoltaic performance improvement of P₃HT:PCBM polymer solar cells by annealing treatment," *Acta Physico*, vol. 27, no. 4, pp. 875–880, 2011.
- [26] C.-Y. Kuo, M.-S. Su, G.-Y. Chen, C.-S. Ku, and K.-H. Wei, "Annealing treatment improves the morphology and performance of photovoltaic devices prepared from thieno[3,4-c]pyrrole-4,6-dione-based donor/acceptor conjugated polymers and CdSe nanostructures," *Energy and Environmental Science*, vol. 4, no. 6, pp. 2316–2322, 2011.
- [27] Z. Zhao, L. Rice, H. Efstathiadis, and P. Haldar, "Thickness dependent effects of thermal annealing and solvent vapor treatment of poly(3-hexylthiophene) and fullerene bulk heterojunction photovoltaics," in *MRS Fall Meeting, Photovoltaic Materials and Manufacturing Issues*, vol. 1123, pp. 171–178, December 2008.
- [28] H.-Z. Yu and J.-B. Peng, "Annealing treatment effect on photoelectric properties of P₃HT:PCBM blend system," *Acta Physico*, vol. 24, no. 5, pp. 905–908, 2008.
- [29] J. Huang, Z. Xu, and Y. Yang, "Low-work-function surface formed by solution-processed and thermally deposited nanoscale layers of cesium carbonate," *Advanced Functional Materials*, vol. 17, no. 12, pp. 1966–1973, 2007.
- [30] H.-H. Liao, L.-M. Chen, Z. Xu, G. Li, and Y. Yang, "Highly efficient inverted polymer solar cell by low temperature annealing of Cs₂CO₃ interlayer," *Applied Physics Letters*, vol. 92, no. 17, Article ID 173303, 2008.
- [31] F. Cheng, G. Fang, X. Fan et al., "Enhancing the short-circuit current and efficiency of organic solar cells using MoO₃ and CuPc as buffer layers," *Solar Energy Materials and Solar Cells*, vol. 95, no. 10, pp. 2914–2919, 2011.
- [32] F. Zhang, F. Sun, Y. Shi et al., "Effect of an ultra-thin molybdenum trioxide layer and illumination intensity on the performance of organic photovoltaic devices," *Energy and Fuels*, vol. 24, no. 7, pp. 3739–3742, 2010.

Research Article

Annealing Effect on Photovoltaic Performance of CdSe Quantum-Dots-Sensitized TiO₂ Nanorod Solar Cells

Yitan Li,¹ Lin Wei,² Ruizi Zhang,¹ Yanxue Chen,¹ and Jun Jiao³

¹ School of Physics and State Key Laboratory of Crystal Materials, Shandong University, Jinan 250100, China

² School of Information Science and Engineering, Shandong University, Jinan 250100, China

³ Department of Physics, Portland State University, P.O. Box 751, Portland, OR 97207-0751, USA

Correspondence should be addressed to Yanxue Chen, cyx@sdu.edu.cn

Received 4 August 2012; Revised 22 October 2012; Accepted 24 October 2012

Academic Editor: Jian Wei

Copyright © 2012 Yitan Li et al. This is an open access article distributed under the Creative Commons Attribution License, which permits unrestricted use, distribution, and reproduction in any medium, provided the original work is properly cited.

Large area rutile TiO₂ nanorod arrays were grown on F:SnO₂ (FTO) conductive glass using a hydrothermal method at low temperature. CdSe quantum dots (QDs) were deposited onto single-crystalline TiO₂ nanorod arrays by a chemical bath deposition (CBD) method to make a photoelectrode. The solar cell was assembled using a CdSe-TiO₂ nanostructure as the photoanode and polysulfide solution as the electrolyte. The annealing effect on optical and photovoltaic properties of CdSe quantum-dots-sensitized TiO₂ nanorod solar cells was studied systematically. A significant change of the morphology and a regular red shift of band gap of CdSe nanoparticles were observed after annealing treatment. At the same time, an improved photovoltaic performance was obtained for quantum-dots-sensitized solar cell using the annealed CdSe-TiO₂ nanostructure electrode. The power conversion efficiency improved from 0.59% to 1.45% as a consequence of the annealing effect. This improvement can be explained by considering the changes in the morphology, the crystalline quality, and the optical properties caused by annealing treatment.

1. Introduction

At present, technologies to utilize solar energy have attracted world-wide attention. Although the solar cells based on monocrystalline Si could provide ample power, their relatively high cost has impaired the research and development of new photovoltaic (PV) systems. Many new PV systems have been introduced including dye-sensitized solar cell [1–3], organic solar cells [4], and multijunction solar cells [5]. As a promising alternative to silicon-based solar cells, dye-sensitized solar cells (DSSCs) have played a promising role in the development of renewable energy. In the laboratory, DSSCs can reach light-to-electric conversion efficiencies of up to 11% [6]. Although the results reported recently are very impressive, the use of expensive dye to sensitize the solar cell is still not feasible for practical applications. Therefore, it is critical to tailor the materials to be not only cost-effective but also long lasting.

Considering the high cost and low stability of organic dyes, using nanosized narrowband gap semiconductor materials as sensitizers in place of the molecular dyes in DSSCs has been put forward as an efficient and promising alternative. Inorganic semiconductors have several advantages over conventional dyes. (i) The band gap of semiconductor quantum dots (QDs) can be tuned by size to match the solar spectrum. (ii) Their large intrinsic dipole moments can lead to rapid charge separation and a large extinction coefficient, which is known to reduce the dark current and increase the overall efficiency. (iii) In addition, semiconductor QD sensitizers provide new chances to utilize hot electrons or generate multiple charge carriers with a single photon. Hence, nanosized narrowband gap semiconductors are ideal candidates for the optimization of a solar cell for improved performance.

Recently, various nanosized semiconductors including CdS [7], CdSe [8], CdTe [9], Sb₂S₃ [10, 11], and Bi₂S₃

[12] have been studied for photocatalyst and solar cell applications. Among these sensitizers, CdSe has shown much promise as an impressive sensitizer due to its reasonable band gap of about 1.70 eV, which has a strong absorption of the solar spectrum. The use of CdSe quantum dots, which may produce more than one electron-hole pair per single absorbed photon (also known as multiple exciton generation (MEG)), is a promising solution to enhance power conversion efficiency. Furthermore, the creation of a type-II heterojunction by growing CdSe QDs on the TiO₂ surface greatly enhances charge separation. All these effects are known to increase the exciton concentration, quantum yield, and lifetime of hot electrons and therefore, the performance of QD-sensitized solar cells.

To date, CdSe-TiO₂-nanostructured solar cells have been reported by several groups [13–16]. While most of the reported work was conducted on polycrystalline TiO₂, little work has been done on the single-crystalline TiO₂ nanorod arrays. Compared with polycrystalline TiO₂, single-crystalline TiO₂ nanorods grown directly on transparent conductive oxide (TCO) electrodes provide a perfect solution by avoiding the particle-to-particle hopping that occurs in polycrystalline films, thereby increasing the photocurrent efficiency.

In this paper, we combine CdSe semiconductor quantum dots and single-crystalline rutile TiO₂ nanorod arrays to produce a practical quantum-dot-sensitized solar cell. A low-temperature hydrothermal technique was used to grow ordered TiO₂ nanorod arrays directly on fluorine-doped tin oxide (FTO) glass, and CdSe nanoparticles were deposited using a CBD method. Postpreparation annealing was conducted to improve the solar cell performance. After annealing, apparent changes in morphology, optical and photovoltaic properties were observed. The photoconversion efficiency of the quantum-dots-sensitized solar cell assembled using a CdSe-TiO₂ nanostructure annealed at 400°C for 30 min showed an increase of 146% compared with that based on as-grown CdSe-TiO₂ nanostructure.

2. Experimental

2.1. Growth of Single-Crystalline Rutile TiO₂ Nanorods by Hydrothermal Process. Ordered TiO₂ nanostructures with different morphologies, such as nanowires [17], nanotubes [18], and nanoparticles [19], have been obtained by different groups using hard-template methods. Alternative wet-chemical techniques for crystalline TiO₂ growth and morphology control are also an interesting and promising subject. It is known that in wet-chemical techniques, the particle size, morphology, and structure can be easily controlled by adjusting preparation parameters. In this study, single crystal rutile TiO₂ nanorod arrays were directly grown on fluorine-doped-tin-oxide- (FTO-) coated glass using the following hydrothermal method. 50 mL of deionized water was mixed with 40 mL of concentrated hydrochloric acid (HCl, 36–38% by weight, Sinopharm). After stirring at ambient temperature for 5 min, 400 μ L of titanium tetrachloride (TiCl₄, 99.9%, Aladdin) was added to the mixture.

The mixture was injected into a stainless steel autoclave with a Teflon container cartridge. The FTO substrates were ultrasonically cleaned for 10 min in a mixed solution of deionized water, acetone, and 2-propanol with volume ratios of 1 : 1 : 1 and then were placed at an angle against the Teflon container wall with the conducting side facing down. The hydrothermal synthesis was conducted at 180°C for 2 h. After synthesis, the autoclave was cooled to room temperature under flowing water, and the FTO substrates were taken out, washed extensively with deionized water, and dried in the open air.

2.2. Deposition of CdSe Nanoparticles with Chemical Bath Deposition (CBD) Method and Annealing Treatment. In a typical CBD cycle, the F:SnO₂ conductive glass, pregrown with TiO₂ nanorod arrays, was dipped into the 0.2 M cadmium chloride (CdCl₂) solution for 5 minutes, rinsed in water, then dipped into the 0.1 M sodium selenosulphate solution (obtained by constantly stirring the mixed solution of selenium powder and sodium sulphite for 6 h at 50°C) for another 5 minutes at 80°C, and rinsed in water. This entire CBD process was repeated from 5 to 9 cycles to achieve the desired thickness of CdSe nanoparticles layer. To investigate the annealing effect on the optical and structural properties of synthesized CdSe-TiO₂ nanostructures, annealing treatments were carried out in air at varied temperatures from 100°C to 400°C for 30 min using a tube furnace.

2.3. Characterization. A field emission scanning electron microscope (SEM, S-4800, Hitachi) and a transmission electron microscope (TEM, JEOL JEM-2100) were used to characterize the morphology and internal structures of the samples. The crystal structure of the CdSe-TiO₂ samples was examined by X-ray diffraction (XD-3, PG Instruments Ltd.) with Cu K α radiation ($\lambda = 0.154$ nm) at a scan rate of 2° per min. X-ray tube voltage and current were set at 40 kV and 35 mA, respectively. The optical absorption spectra were obtained using a UV-visible spectrometer (TU-1900, PG Instruments, Ltd.).

2.4. J-V Measurements. Solar cells were assembled using CdSe-TiO₂ nanostructures as the photoanode. Pt counter electrodes were prepared by depositing 20 nm thick Pt film on FTO glass using magnetron sputtering. A 60 μ m thick sealing material (SX-1170-60, Solaronix SA) with a 2.5 \times 2.5 mm aperture was pasted onto the Pt counter electrodes. The Pt counter electrode and the CdSe-TiO₂ photoelectrode were sandwiched and sealed with the conductive sides facing inward. A polysulfide electrolyte was injected into the space between the two electrodes. The polysulfide electrolyte was composed of 1 M sulfur, 1 M Na₂S, and 0.1 M NaOH, which were dissolved in methanol/water (7 : 3, v/v) and stirred at 80°C for 2 h.

A solar simulator (Model 94022A, Newport) with an AM1.5 filter was used to illuminate the working solar cell at light intensity of 1 sun illumination (100 mW/cm²). A sourcemeter (2400, Keithley) was used for electrical characterization during the measurements. The measurements

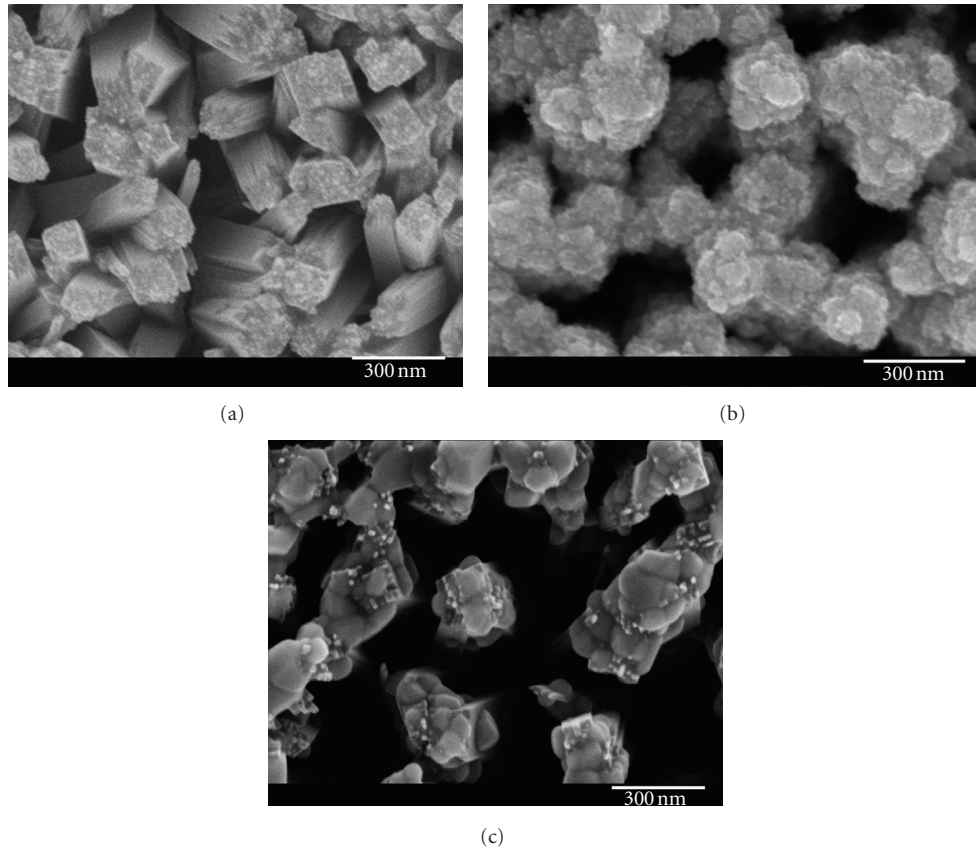


FIGURE 1: Top view SEM images of the bare TiO₂ nanorod (a), the CdSe-TiO₂ nanostructure after 7 CBD cycles (b), and the sample with 7 CBD cycles annealed at 400°C for 30 minutes (c).

were carried out with respect to a calibrated OSI standard silicon solar photodiode.

3. Results and Discussion

Field emission scanning electron microscopy (FESEM) images show a typical morphology of the rutile TiO₂ nanorod arrays in Figure 1(a), confirming that the entire surface of the FTO-coated glass substrate was uniformly covered with ordered TiO₂ nanorods. The nanorods are typically 100–150 nm in diameter and are tetragonal in shape with square top facets consisting of many small grids. The density of nanorods is 20 nanorods/ μm^2 with suitable space for deposition of CdSe nanoparticles. The CdSe QDs deposited onto TiO₂ nanorods with different CBD cycles were also characterized by FESEM. The SEM results (not shown here) suggest that as the number of CBD cycles increased from 5 to 7 and then to 9, the thickness of the CdSe nanoparticles increased correspondingly. A thicker CdSe nanoparticles layer is beneficial for stronger sunlight absorption, but will cause severe recombination of photo-induced carriers at the same time. Hence, an optimal thickness should be determined to achieve a higher power conversion efficiency. In our experiment, the best photovoltaic performance was observed in the CdSe-TiO₂ photoelectrode deposited with 7 CBD cycles. Therefore, in the following research process

we are focused on this CdSe-TiO₂ nanostructure with 7 deposition cycles to study the annealing effect on optical and photovoltaic properties. A close look at the CdSe-TiO₂ nanostructure with 7 successive deposition cycles is shown in Figure 1(b). A uniform porous CdSe shell composed of small nanoparticles was formed on the TiO₂ nanorod surface. Figure 1(c) showed the morphology of this CdSe-TiO₂ nanostructure after annealing at 400°C for 30 minutes. Compared with Figure 1(b), a significant change in the morphology was observed. After annealing, the porous CdSe layer transformed into larger CdSe particles with size of about 100 to 150 nm. Also, as shown in Figure 1(c), this annealing treatment enabled a much close contact between CdSe particle and the TiO₂ nanorod surface. This firm connection is beneficial to the charge separation and will improve the overall properties of the sensitized solar cells.

The detailed microscopic structure of the CdSe nanoparticles before and after annealing was further investigated by a high-resolution TEM. For the as-deposited sample only a blurred HRTEM image (Figure 2(a)) was obtained, which indicates that the CdSe layer is polycrystalline with a poor crystallization. Further characterization suggests that the CdSe shell consists of nanoparticles with an average diameter of approximately 5–10 nm, which is coincident with the SEM measurement above. The HRTEM image of the annealed CdSe-TiO₂ nanostructure is presented in Figure 2(b).

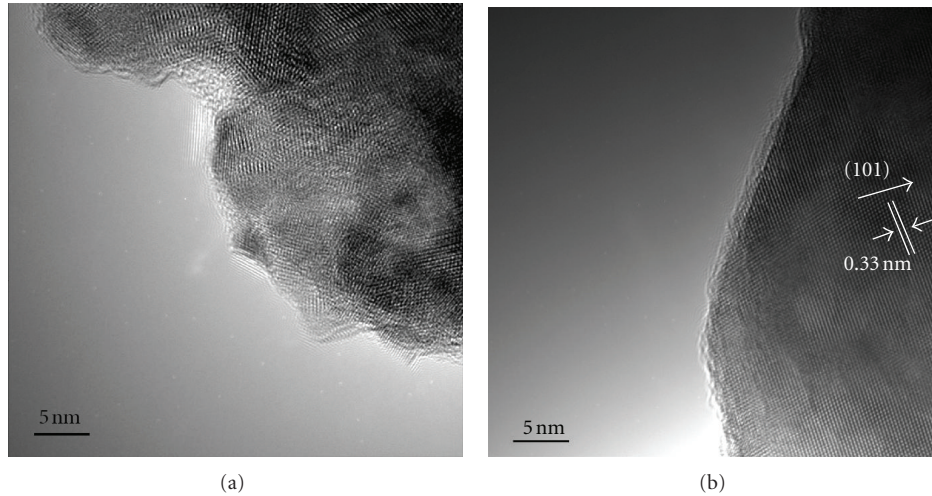


FIGURE 2: HRTEM images of CdSe nanoparticles deposited on TiO₂ nanorod arrays before (a) and after (b) annealing treatment.

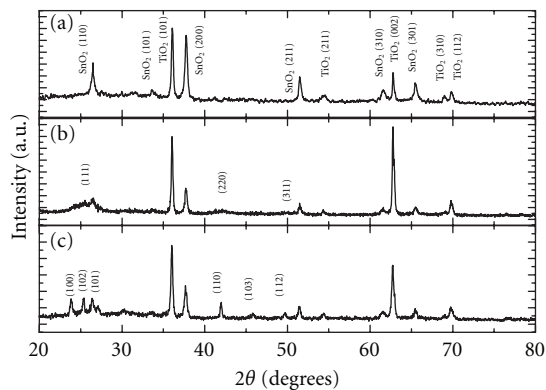


FIGURE 3: XRD patterns of (a) the TiO₂ bare nanorod array, (b) the as-synthesized CdSe-TiO₂ nanorod array electrode, and (c) the CdSe-TiO₂ nanorod array electrode annealed at 400°C for 30 min. All the peaks from SnO₂ and TiO₂ are indexed in (a), and those from CdSe nanoparticles are indexed in (b) and (c).

The clear lattice fringes in the HRTEM image indicate that the CdSe particle has a high degree of crystallinity. The lattice spacing is measured to be approximately 0.33 nm, which agrees well with the spacing of the (101) planes of the wurtzite CdSe. The high interior crystal quality of the CdSe nanoparticles is conducive to reduce the recombination of the excited electron-hole pairs and increase the photocurrent of the solar cells.

X-ray diffraction (XRD) patterns of the bare TiO₂ nanorod array, the as-synthesized CdSe-TiO₂ nanostructure, and the annealed nanostructure are shown in Figure 3. Note in Figure 3(a) that the TiO₂ nanorod arrays grown on the FTO-coated glass substrates have a tetragonal rutile structure (JCPDS no. 02-0494), which could be attributed to the small lattice mismatch between FTO and rutile. The as-synthesized CdSe-TiO₂ nanostructure exhibits weak diffraction peaks at $2\theta = 25.3^\circ$, 42.0° , and 49.8° , corresponding to the (111), (220), and (311) planes of metastable cubic (sphalerite)

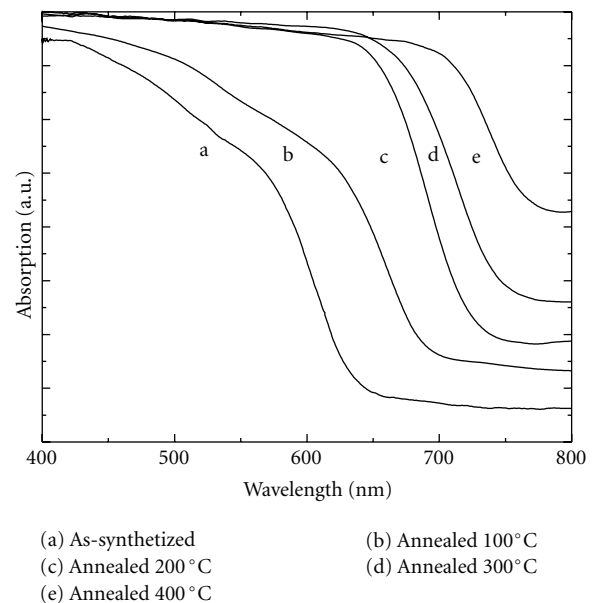


FIGURE 4: Optical absorption spectra of CdSe-TiO₂ nanostructure samples before (a) and after annealing at 100°C (b), 200°C (c), 300°C (d), and 400°C (e).

CdSe with the lattice constant $a = 0.609$ nm (JCPDS no. 19-0191). After being annealed at 400°C, diffraction peaks could be indexed as the (100), (102), (101), (110), (103), and (112) planes of wurtzite hexagonal phase (JCPDS no. 08-0459). Compared with Figure 3(b), it is obvious that for the annealed samples, the diffraction peaks became sharper and the full width at half maximum (FWHM) decreased. This was due to the improvement of the crystalline and the increase in particle size during the annealing process.

The optical absorption spectra of CdSe-TiO₂ nanostructure samples are shown in Figure 4. An optical band gap of 2.04 eV is estimated for the as-synthesized CdSe nanoparticles from the absorption spectra, which are much

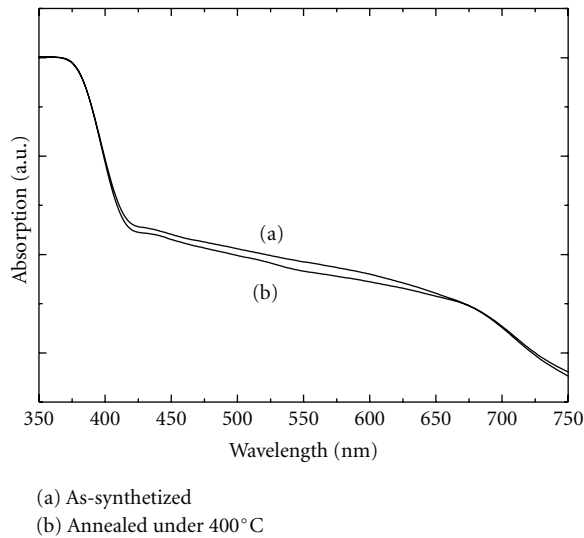


FIGURE 5: Optical absorption spectra of nanorod arrays with and without annealing treatment.

wider than that of bulk wurtzite CdSe. After annealing at 100°C, 200°C, 300°C, and 400°C for 30 min, respectively, the band gap of CdSe nanoparticles was red-shifted to 1.88 eV (660 nm), 1.80 eV (690 nm), 1.74 eV (714 nm), and 1.68 eV (736 nm) accordingly (Figures 4(b)–4(e)). The annealed CdSe-TiO₂ nanostructures show an enhanced absorption in the visible range, which is very important for solar cell application and will result in higher power conversion efficiency. As shown by the XRD patterns, SEM images and HRTEM images, this red shift in the annealed samples could be explained by the annealing-induced phase transformation (from cubic to hexagonal) at the elevated temperatures as well as the increase in particle size [20]. The annealing effect on the optical absorption spectra of bare TiO₂ nanorod arrays was also studied. As shown in Figure 5, no obvious difference was found between the samples with and without annealing treatment. This result suggests that although annealing changes the morphology and crystallinity of CdSe nanoparticles, it does not have significant effect on the optical property of the TiO₂ nanorod arrays.

Figure 6 shows the photocurrent-voltage (I-V) performance of the quantum-dots-sensitized solar cells assembled using CdSe-TiO₂ nanostructures annealed under different temperatures. The I-V curves of the QDSSC were measured under one sun illumination (AM1.5, 100 mW/cm²). An open-circuit voltage (V_{oc}) of 0.33 V, a short-circuit current density (J_{sc}) of 7.8 mA/cm², and an overall efficiency of 0.59% were observed for QDSSC based on the as-grown CdSe-TiO₂ nanostructure. As the annealing temperature increased, the open-circuit voltage (V_{oc}) was improved from 0.33 V to 0.38 V, and the short-circuit current density (J_{sc}) was increased from 7.7 mA/cm² to 12.5 mA/cm². An overall efficiency of 1.45% was observed for QDSSC based on CdSe-TiO₂ nanostructures annealed at 400°C, indicating an increase of up to 146% compared with that of the as-synthesized one.

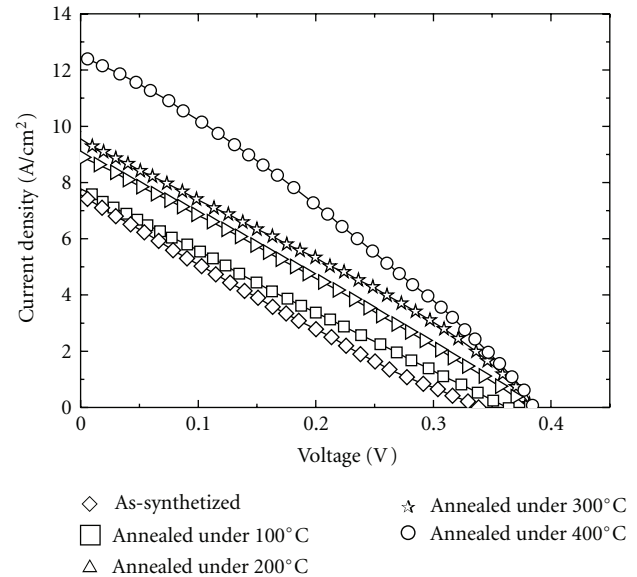


FIGURE 6: I-V curves for the solar cells assembled using CdSe-TiO₂ nanostructures annealed under different temperatures.

This significant improvement of the photovoltaic performance obtained for QDSSC based on annealed CdSe-TiO₂ nanostructure can be ascribed to the following reasons. (i) As confirmed by the absorption spectra presented in Figure 4, an enhanced absorption of sunlight caused by the red shift of the band gap will result in an enhanced current density. (ii) Increase of CdSe grain size by annealing will reduce the particle-to-particle hopping of the photo-induced carrier. This hopping may occur in an as-grown nanostructure with a CdSe layer composed of CdSe nanoparticles. (iii) Improvement of crystal quality of the CdSe nanoparticles by annealing treatment will decrease the internal defects, which can reduce the recombination of photoexcited carriers and result in a higher power conversion efficiency. (iv) Good contact between the CdSe quantum dots and the TiO₂ nanorod is formed as a result of high-temperature annealing. Such a superior interface between TiO₂ and QDs can inhibit the interfacial recombination of the injected electrons from TiO₂ to the electrolyte, which is also responsible for its higher efficiency.

This study opens the possibility of using a 3D nanostructure material with a facile hydrothermal method for QDSSC studies. In present work, the low photoelectric efficiency may be caused by the low transport efficiency of the S/S⁻² redox couple. By applying more efficient redox couple electrolyte, higher cell efficiency could be achieved.

4. Conclusions

Using a facile hydrothermal method, the single-crystalline TiO₂ nanorod arrays were successfully grown on fluorine-doped tin oxide (FTO) glass. Then the densely distributed CdSe nanoparticles were deposited on TiO₂ nanorod arrays using a chemical bath deposition (CBD) method. Annealing

was conducted to improve the properties of the CdSe-TiO₂ nanostructure. Greatly improved crystallinity of CdSe nanoparticles and obvious enhancement in visible light absorption were observed for the annealed samples. Significant improvement of the photovoltaic performance for QDSSC based on the annealed CdSe-TiO₂ nanostructure was obtained. Compared with QDSSC based on as-deposited CdSe-TiO₂ nanostructures, an increase of up to 146% in power conversion efficiency was achieved for QDSSCs using the annealed CdSe-TiO₂ photoanode.

Acknowledgments

This work was supported by the State Key Research Development Program of China (2010CB833103), the National Natural Science Foundation of China (60976073), the National Found for Fostering Talents of Basic Science (J1103212), and the Foundation for Outstanding Young Scientist in Shandong Province (BS2010CL036). J. Jiao thanks the financial support from the Oregon Nanoscience Microtechnologies Institute (ONAMI) and the National Science Foundation.

References

- [1] B. O'Regan and M. Grätzel, "A low-cost, high-efficiency solar cell based on dye-sensitized colloidal TiO₂ films," *Nature*, vol. 353, no. 6346, pp. 737–740, 1991.
- [2] M. Grätzel, "Photoelectrochemical cells," *Nature*, vol. 414, no. 6861, pp. 338–344, 2001.
- [3] H. S. Chen, C. Su, J. L. Chen, T. Y. Yang, N. M. Hsu, and W. R. Li, "Preparation and characterization of pure rutile TiO₂ nanoparticles for photocatalytic study and thin films for dye-sensitized solar cells," *Journal of Nanomaterials*, vol. 2011, Article ID 869618, 8 pages, 2011.
- [4] F. A. de Castro, F. Nüesch, C. Walder, and R. Hany, "Challenges found when patterning semiconducting polymers with electric fields for organic solar cell applications," *Journal of Nanomaterials*, vol. 2012, Article ID 478296, 6 pages, 2012.
- [5] M. Yamaguchi, "Multi-junction solar cells and novel structures for solar cell applications," *Physica E*, vol. 14, no. 1-2, pp. 84–90, 2002.
- [6] Y. Chiba, A. Islam, Y. Watanabe, R. Komiya, N. Koide, and L. Han, "Dye-sensitized solar cells with conversion efficiency of 11.1%," *Japanese Journal of Applied Physics*, vol. 45, no. 24–28, pp. L638–L640, 2006.
- [7] C. Wang, Z. Jiang, L. Wei et al., "Photosensitization of TiO₂ nanorods with CdS quantum dots for photovoltaic applications: a wet-chemical approach," *Nano Energy*, vol. 1, no. 3, pp. 440–447, 2012.
- [8] U. Farva and C. Park, "Colloidal synthesis and air-annealing of CdSe nanorods for the applications in hybrid bulk heterojunction solar cells," *Materials Letters*, vol. 64, no. 13, pp. 1415–1417, 2010.
- [9] A. Morales-Acevedo, "Thin film CdS/CdTe solar cells: research perspectives," *Solar Energy*, vol. 80, no. 6, pp. 675–681, 2006.
- [10] Y. Itzhaik, O. Niitsoo, M. Page, and G. Hodes, "Sb₂S₃-sensitized nanoporous TiO₂ solar cells," *Journal of Physical Chemistry C*, vol. 113, no. 11, pp. 4254–4256, 2009.
- [11] M. Sun, G. Chen, Y. Zhang, Q. Wei, Z. Ma, and B. Du, "Efficient degradation of azo dyes over Sb₂S₃/TiO₂ heterojunction under visible light irradiation," *Industrial & Engineering Chemistry Research*, vol. 51, no. 7, pp. 2897–2903, 2012.
- [12] L. M. Peter, K. G. U. Wijayantha, D. J. Riley, and J. P. Waggett, "Band-edge tuning in self-assembled layers of Bi₂S₃ nanoparticles used to photosensitize nanocrystalline TiO₂," *Journal of Physical Chemistry B*, vol. 107, no. 33, pp. 8378–8381, 2003.
- [13] I. Robel, V. Subramanian, M. Kuno, and P. V. Kamat, "Quantum dot solar cells. Harvesting light energy with CdSe nanocrystals molecularly linked to mesoscopic TiO₂ films," *Journal of the American Chemical Society*, vol. 128, no. 7, pp. 2385–2393, 2006.
- [14] J. Y. Kim, S. B. Choi, J. H. Noh et al., "Synthesis of CdSe-TiO₂ nanocomposites and their applications to TiO₂ sensitized solar cells," *Langmuir*, vol. 25, no. 9, pp. 5348–5351, 2009.
- [15] L. Liu, J. Hensel, R. C. Fitzmorris, Y. Li, and J. Z. Zhang, "Preparation and photoelectrochemical properties of CdSe/TiO₂ hybrid mesoporous structures," *Journal of Physical Chemistry Letters*, vol. 1, no. 1, pp. 155–160, 2010.
- [16] L. Yang, S. Luo, R. Liu et al., "Fabrication of cdse nanoparticles sensitized long TiO₂ nanotube arrays for photocatalytic degradation of anthracene-9-carboxylic acid under green monochromatic light," *Journal of Physical Chemistry C*, vol. 114, no. 11, pp. 4783–4789, 2010.
- [17] Z. Zhou, J. Fan, X. Wang, W. Zhou, Z. Du, and S. Wu, "Effect of highly ordered single-crystalline TiO₂ nanowire length on the photovoltaic performance of dye-sensitized solar cells," *ACS Applied Materials & Interfaces*, vol. 3, no. 11, pp. 4349–4353, 2011.
- [18] J. Wang and Z. Lin, "Dye-sensitized TiO₂ nanotube solar cells with markedly enhanced performance via rational surface engineering," *Chemistry of Materials*, vol. 22, no. 2, pp. 579–584, 2010.
- [19] P. Wang, A. Abrusci, H. M. P. Wong, M. Svensson, M. R. Andersson, and N. C. Greenham, "Photoinduced charge transfer and efficient solar energy conversion in a blend of a red polyfluorene copolymer with CdSe nanoparticles," *Nano Letters*, vol. 6, no. 8, pp. 1789–1793, 2006.
- [20] A. Kongkanand, K. Tvrdy, K. Takechi, M. Kuno, and P. V. Kamat, "Quantum dot solar cells. Tuning photoresponse through size and shape control of CdSe-TiO₂ architecture," *Journal of the American Chemical Society*, vol. 130, no. 12, pp. 4007–4015, 2008.

Research Article

Preparation and Characterization of Alumina Nanoparticles in Deionized Water Using Laser Ablation Technique

**Veeradate Piriya Wong,^{1,2} Voranuch Thongpool,¹
Piyapong Asanithi,¹ and Pichet Limsuwan^{1,2}**

¹Applied Nanotechnology Laboratory (ANT Lab), Department of Physics,
King Mongkut's University of Technology Thonburi, Bangkok 10140, Thailand

²Thailand Center of Excellence in Physics, CHE, Ministry of Education, Bangkok 10400, Thailand

Correspondence should be addressed to Veeradate Piriya Wong, changphysics@hotmail.com
and Pichet Limsuwan, opticslaser@yahoo.com

Received 9 August 2012; Accepted 23 October 2012

Academic Editor: Jian Wei

Copyright © 2012 Veeradate Piriya Wong et al. This is an open access article distributed under the Creative Commons Attribution License, which permits unrestricted use, distribution, and reproduction in any medium, provided the original work is properly cited.

Al₂O₃ nanoparticles were synthesized using laser ablation of an aluminum (Al) target in deionized water. Nd:YAG laser, emitted the light at a wavelength of 1064 nm, was used as a light source. The laser ablation was carried out at different energies of 1, 3, and 5 J. The structure of ablated Al particles suspended in deionized water was investigated using X-ray diffraction (XRD). The XRD patterns revealed that the ablated Al particles transformed into γ -Al₂O₃. The morphology of nanoparticles was investigated by field emission scanning electron microscopy (FE-SEM). The FE-SEM images showed that most of the nanoparticles obtained from all the ablated laser energies have spherical shape with a particle size of less than 100 nm. Furthermore, it was observed that the particle size increased with increasing the laser energy. The absorption spectra of Al₂O₃ nanoparticles suspended in deionized water were recorded at room temperature using UV-visible spectroscopy. The absorption spectra show a strong peak at 210 nm arising from the presence of Al₂O₃ nanoparticles. The results on absorption spectra are in good agreement with those investigated by XRD which confirmed the formation of Al₂O₃ nanoparticles during the laser ablation of Al target in deionized water.

1. Introduction

Metal oxide nanoparticles have been extensively developed in the past decades. They have been widely used in many applications such as catalysts, sensors, semiconductors, medical science, capacitors, and batteries [1–6]. Among them, aluminum oxide (Al₂O₃) and its compounds have long been known for more than a century, for example, aluminum oxide hydroxide (AlOOH) and aluminum trihydroxide (Al(OH)₃).

Al₂O₃ or alumina generally refers to corundum. It is a white oxide. Alumina has several phases such as gamma, delta, theta, and alpha. However, the alpha alumina phase is the most thermodynamically stable phase. In general, alumina has many interesting properties, for example high hardness, high stability, high insulation, and transparency [7]. Alumina is also widely used in the fire retard, catalyst,

insulator, surface protective coating, and composite materials [8–12].

Al₂O₃ nanoparticles can be synthesized by many techniques including ball milling, sol-gel, pyrolysis, sputtering, hydrothermal, and laser ablation [13–18]. Among them, the laser ablation is a widely used technique for the synthesis of nanoparticles since it can be synthesized in gas, vacuum or liquid. This technique offers several advantages such as rapid and high purity process compared with other methods [19]. Furthermore, nanoparticles prepared by the laser ablation of materials in liquid are easier to be collected than those of in gas atmosphere.

In the recent years, Al₂O₃ nanoparticles were synthesized in liquid using a short pulse laser with the pulse width in the range of nanosecond [20–22]. Furthermore, Al target was used as a starting material for laser ablation in those works. Therefore, in this study we reported the synthesis

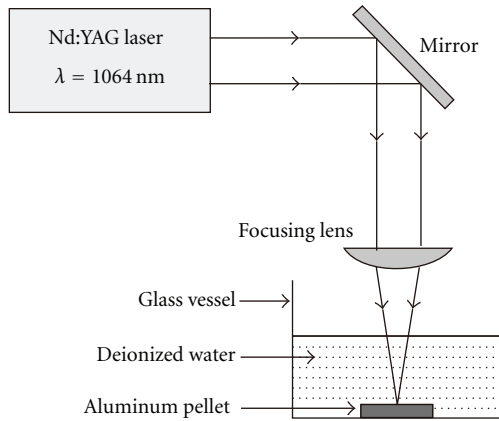


FIGURE 1: Experimental setup for synthesizing Al_2O_3 nanoparticles by laser ablation of Al in deionized water.

of Al_2O_3 from Al powders using laser ablation in deionized water with a long pulsed Nd:YAG laser. The laser pulse widths adopted in this work were 2.5, 6, and 9.5 ms to obtain the output laser energies of 1, 3, and 5 J, respectively. The particle size and morphology of synthesized nanoparticles obtained at different laser energies were investigated by field emission scanning electron microscopy (FE-SEM). The optical property of synthesized nanoparticles was carried out using UV-visible spectroscopy. The structure of the synthesized nanoparticles was investigated using X-ray diffraction (XRD) technique.

2. Experimental Setup

2.1. Material Preparation for Laser Ablation. Aluminum powder with purity of 99.99% (American Elements) and an average particle size of $35\ \mu\text{m}$ were pressed in a stainless steel mold by a hydraulic with a pressure of 100 bars to obtain the aluminum pellet with a diameter of 15 mm and 5 mm thick. The aluminum pellet was used as a target for laser ablation. The experimental setup of the laser ablation is shown in Figure 1. The aluminum pellet was placed at the bottom of a glass vessel with a diameter of 30 mm and 50 mm in height. Deionized water with a volume approximately of 10 mL was poured into the vessel until its level was approximately 5 mm above the target. The Nd:YAG (Miyachi, ML-2331B) that emitted the laser light at a wavelength of 1064 nm was used for the laser ablation. The laser ablation was carried out at different laser energies of 1, 3, and 5 J with a repetition rate of 2 Hz. The laser beam was focused by a 50 mm focal-length lens onto the aluminum pellet. For each energy of laser ablation, the aluminum target was ablated with 5,000 pulses for the total time of about 40 min. After the laser ablation, the Al_2O_3 particles suspended in deionized water was obtained.

2.2. Characterization. After the laser ablation of Al target in deionized water was carried out, the Al particles suspended in deionized water were characterized to confirm that they transformed into Al_2O_3 . The ablated Al particles suspended

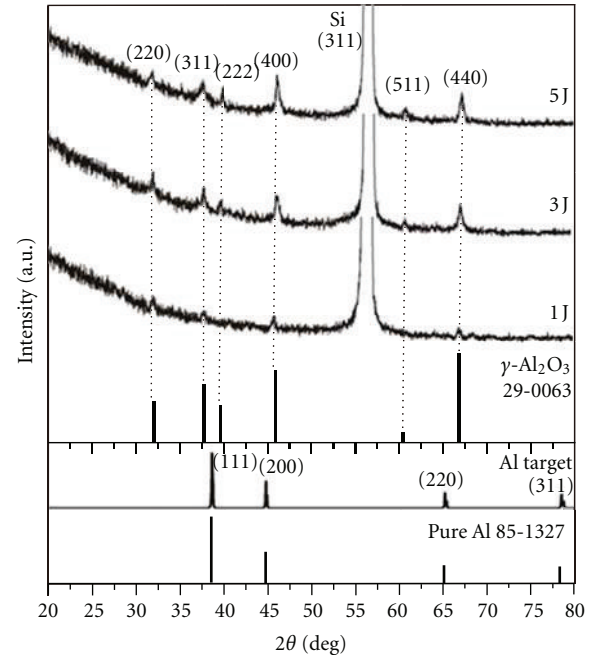


FIGURE 2: XRD patterns of pure Al and Al_2O_3 nanoparticles synthesized from laser energies of 1, 3, and 5 J.

in deionized water were used for the optical measurement. The optical absorption spectra were recorded at room temperature using a UV-Vis spectrophotometer (JASCO, V570). Then, the liquid sample was dropped on silicon wafers and dried in an oven at 40°C for 4 h. The dried-particles sample on silicon substrates was used for investigating the structure and morphology. The structure of particles was investigated using X-ray diffraction (PANalytical, X'Pert Pro) with $\text{CuK}\alpha$ radiation and a pattern recorded at grazing incidence angle (3°) in the 2θ range of 20° – 80° with a scan step of 0.02 in a scan time of 5 s. The morphology of particles was investigated using field emission scanning electron microscopy (Hitachi, S4700).

3. Results and Discussion

3.1. The Structure of Ablated Particles. The structure of ablated particles was investigated by XRD measurement. To identify the structural difference between ablated particles and Al, the XRD measurement for Al target was also carried out. Figure 2 shows the XRD patterns of Al target and particles synthesized from laser energies of 1, 3, and 5 J. The observed peaks in Figure 2 could be indexed based on pure Al and $\gamma\text{-Al}_2\text{O}_3$ phase in Joint Committee on Powder Diffraction Standard-International Center for Diffraction Data (JCPDS-ICDD) Card nos. 85-1327 and 29-0063, respectively. It is seen from the XRD spectra that all particles obtained from laser ablation with different laser energies are $\gamma\text{-Al}_2\text{O}_3$. This confirms that Al transformed into $\gamma\text{-Al}_2\text{O}_3$ after the ablation in deionized water. Moreover, it is clearly observed that the intensity of XRD peaks increased with increasing

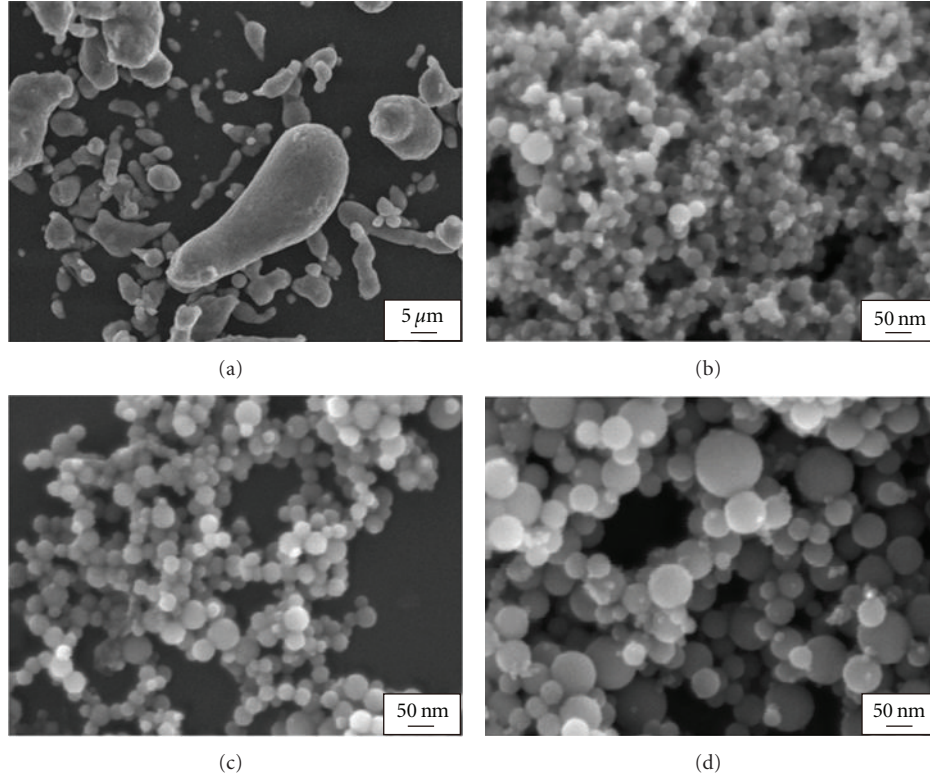
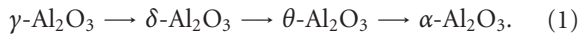


FIGURE 3: FE-SEM images of (a) aluminum powder, and Al_2O_3 nanoparticles at different laser energies of (b) 1 J, (c) 3 J, and (d) 5 J.

laser energy. This might lead to the conclusion that the particle concentration, suspended in deionized water, obtained from a laser energy of 5 J is higher than those of 1 and 3 J.

It should be pointed out that the phase transitions in aluminum oxide occur in the following order [23]:



Since $\gamma\text{-Al}_2\text{O}_3$ occurs at the lowest temperature compared with those of another phases, the most likely phase of Al_2O_3 to be formed after laser ablation of Al target in deionized water is $\gamma\text{-Al}_2\text{O}_3$.

3.2. Morphology of Al_2O_3 Nanoparticles. The morphology of dried Al_2O_3 nanoparticle samples obtained from the laser ablation of aluminum pellet in deionized water at different energies was investigated using field emission scanning electron microscopy. For comparison, the morphology of aluminum powder was also investigated. Figure 3(a) shows the FE-SEM image of the aluminum powder used as the target. It revealed that the morphology of the aluminum was a non-spherical shape with the size in the range of 1–35 μm . Figures 3(b)–3(d) show the FE-SEM images of the Al_2O_3 nanoparticles synthesized in deionized water with different laser energies of 1, 3, and 5 J, respectively. It is clearly observed that the morphology of the synthesized Al_2O_3 nanoparticles is mostly spherical shape. These results are in good agreement with those previously reported in reference [20–22].

The particle size distribution of the Al_2O_3 nanoparticles could be obtained by measuring the size of total particles of

TABLE 1: Average particle size of Al_2O_3 nanoparticles.

Laser energy (J/pulse)	Laser fluence (J/cm^2)	Average size (nm)
1	3333	26
3	10000	38
5	16667	53

about 200 particles in the FE-SEM image using the Image J program. The plots of the particle size distribution of the Al_2O_3 nanoparticles are shown in Figure 4. The average particle size of the Al_2O_3 nanoparticles is summarized in Table 1. As seen in Figure 4, the particle size of the Al_2O_3 nanoparticles synthesized in deionized water with laser energies of 1, 3, and 5 J are ranged from 10 to 60, 10 to 70, and 10 to 110 nm, respectively. The average particle size of the Al_2O_3 nanoparticles as given in Table 1 showed that the smallest particle size of the Al_2O_3 nanoparticles was obtained from a laser energy of 1 J and found to be 26 nm with the narrow particle size distribution in the range of 10–60 nm. It is seen that the higher laser energy seemed to promote more collisions between the vapour atoms/ions, to coalesce within the ablated plume and eventually to form larger particles.

It should be noted that the spot size of the laser at the target surface is 0.03 mm^2 . Hence, the laser fluence (J/cm^2) can be determined and the results are also given in Table 1.

3.3. Optical Property of Al_2O_3 Nanoparticle in Deionized Water. Figure 5 shows the opacity of deionized water after

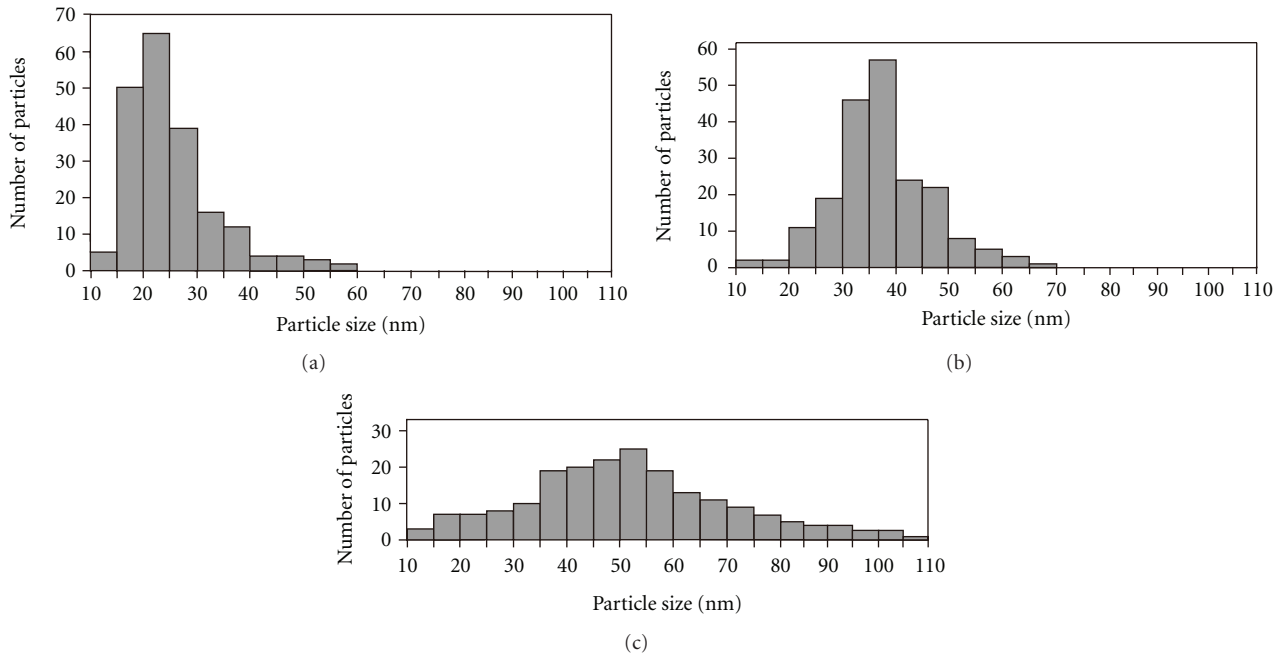


FIGURE 4: Plots of particle size distribution of Al_2O_3 nanoparticles at different energies (a) 1 J, (b) 3 J, and (c) 5 J.

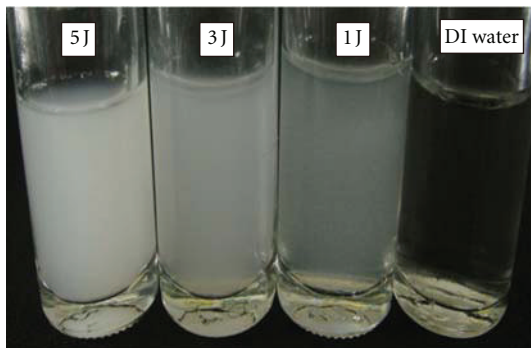


FIGURE 5: Photographs showing the opacity of deionized water before and after laser ablation at different laser energies of 1, 3, and 5 J.

the laser ablation of Al with different laser energies. It is clearly observed that the opacity of deionized water increases with increasing laser energy. It can be concluded that the opacity of deionized water is proportional to the number of Al_2O_3 nanoparticles suspended in deionized water. Hence, the Al_2O_3 nanoparticles obtained from a laser energy of 5 J are higher than those obtained from 3 and 1 J.

Figure 6 shows the absorption spectra of deionized water with suspended Al_2O_3 nanoparticles obtained from laser energies of 1, 3, and 5 J. A strong absorption peak at 210 nm is clearly observed which confirms the presence of Al_2O_3 nanoparticles in deionized water [24, 25] and not those of aluminum [26–28]. As seen in Figure 6, the difference of absorbance is due to the different Al_2O_3 nanoparticle concentrations suspended in deionized water.

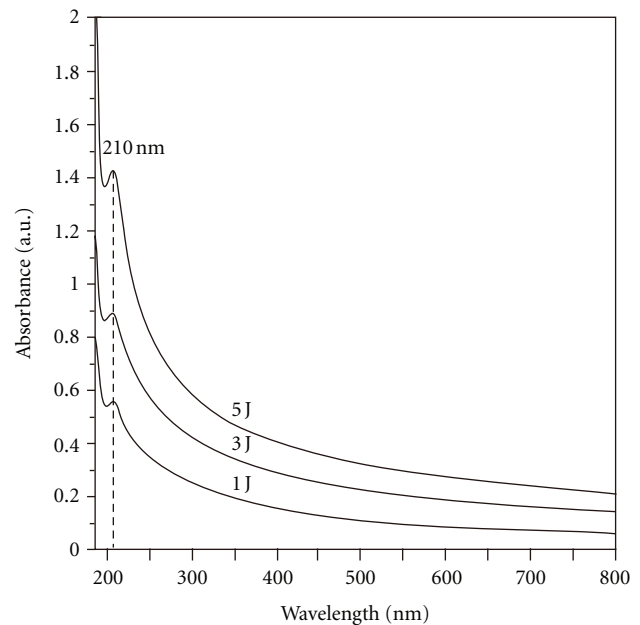


FIGURE 6: Absorption spectra in deionized water with suspended Al_2O_3 nanoparticles prepared from different laser energies of 1, 3, and 5 J.

To confirm the dependence of the absorbance on the Al_2O_3 nanoparticle concentration, all the samples of deionized water with suspended Al_2O_3 nanoparticles were diluted with deionized water to obtain different water concentrations of $C/2$, $C/4$, $C/8$, and $C/16$, where C is the initial concentration. All the diluted deionized water samples were used

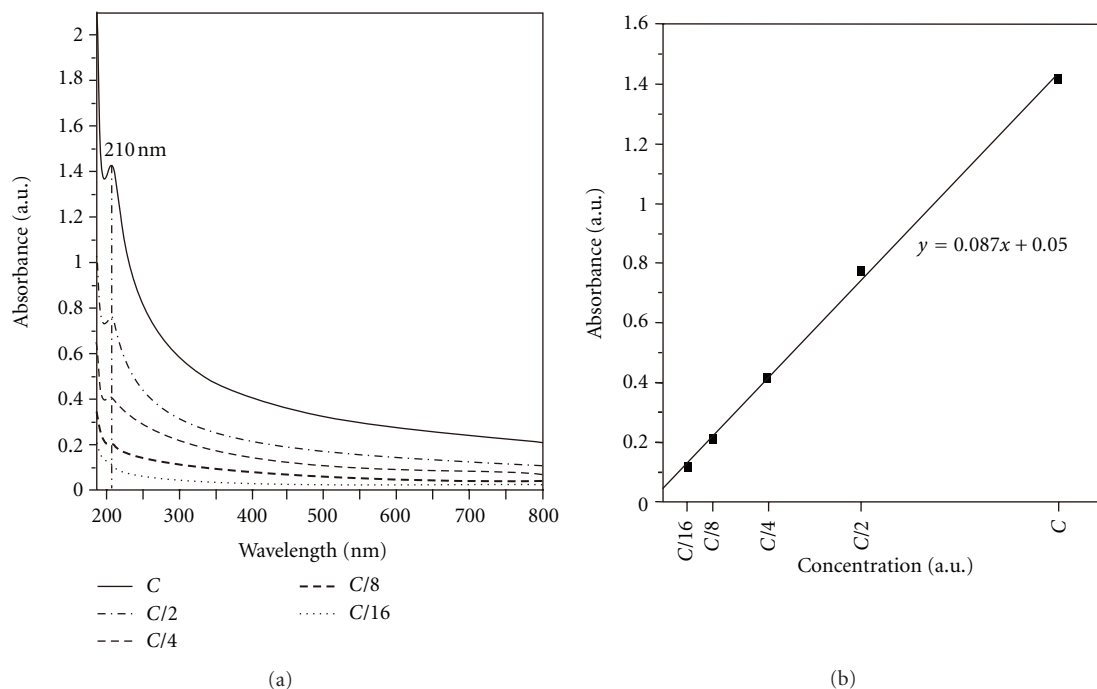


FIGURE 7: (a) The typical absorption spectra of deionized water with different suspended Al_2O_3 nanoparticle concentrations for the laser ablation at an energy of 5 J and (b) linear relationship between the absorbance and the concentration at wavelength 210 nm.

for absorption measurements. Figure 7(a) shows the typical absorption spectra of the deionized water with different Al_2O_3 nanoparticle concentrations obtained from a laser energy of 5 J. It is seen that the absorbance decreases with decreasing concentration. The plot between Al_2O_3 nanoparticle concentration and absorbance is shown in Figure 7(b). Figure 7(b) shows that the absorbance depends linearly on the Al_2O_3 nanoparticle concentration. Similar results were also obtained for laser energies of 1 and 3 J.

4. Conclusion

We have successfully demonstrated that $\gamma\text{-Al}_2\text{O}_3$ nanoparticles can be synthesized from Al powder by pulsed laser ablation in deionized water. Al powder was pressed to obtain the Al pellet and used as a target for laser ablation. The advantage of using compressed Al powder is that we can sieve the Al powder to obtain small particle size for starting materials of laser ablation. Therefore, it is easier to obtain Al_2O_3 nanoparticles compared with those obtained from laser ablation of Al plate. The effect of laser energy on the particle size was investigated. It was found that Al_2O_3 particle size ablated at a low laser energy was smaller than that obtained from high laser energy. However, high laser energy yielded high Al_2O_3 concentration than that of low laser energy.

Acknowledgments

This work had been supported by Thailand Center of Excellent in Physics (ThEP) and King Mongkut's University of

Technology Thonburi under The National Research University Project.

References

- [1] W. Ueda, M. Sadakane, and H. Ogihara, "Nano-structuring of complex metal oxides for catalytic oxidation," *Catalysis Today*, vol. 132, no. 1–4, pp. 2–8, 2008.
- [2] T. Gessner, K. Gottfried, R. Hoffmann et al., "Metal oxide gas sensor for high temperature application," *Microsystem Technologies*, vol. 6, no. 5, pp. 169–174, 2000.
- [3] J. H. Kim, E. K. Kim, C. H. Lee, M. S. Song, Y.-H. Kim, and J. Kim, "Electrical properties of metal-oxide semiconductor nano-particle device," *Physica E*, vol. 26, no. 1–4, pp. 432–435, 2005.
- [4] P. D. Pria, "Evolution and new application of the alumina ceramics in joint replacement," *European Journal of Orthopaedic Surgery and Traumatology*, vol. 17, no. 3, pp. 253–256, 2007.
- [5] H. Farsi and F. Gobal, "Theoretical analysis of the performance of a model supercapacitor consisting of metal oxide nanoparticles," *Journal of Solid State Electrochemistry*, vol. 11, no. 8, pp. 1085–1092, 2007.
- [6] A. C. Dillon, A. H. Mahan, R. Deshpande, P. A. Parilla, K. M. Jones, and S.-H. Lee, "Metal oxide nano-particles for improved electrochromic and lithium-ion battery technologies," *Thin Solid Films*, vol. 516, no. 5, pp. 794–797, 2008.
- [7] L. D. Hart, *Alumina Chemicals: Science and Technology Handbook*, American Ceramic Society, Columbus, Ohio, USA, 1990.
- [8] A. Laachachi, M. Ferriol, M. Cochez, J.-M. Lopez Cuesta, and D. Ruch, "A comparison of the role of boehmite (AlOOH) and alumina (Al_2O_3) in the thermal stability and flammability

- of poly(methyl methacrylate)," *Polymer Degradation and Stability*, vol. 94, no. 9, pp. 1373–1378, 2009.
- [9] I. Lukić, J. Krstić, D. Jovanović, and D. Skala, "Alumina/silica supported K_2CO_3 as a catalyst for biodiesel synthesis from sunflower oil," *Bioresource Technology*, vol. 100, no. 20, pp. 4690–4696, 2009.
- [10] M. Touzin, D. Goeriot, C. Guerret-Piécourt, D. Juvé, and H. J. Fitting, "alumina based ceramics for high-voltage insulation," *Vacuum*, vol. 81, pp. 762–765, 2007.
- [11] A. Keyvani, M. Saremi, and M. Heydarzadeh Sohi, "Micro-structural stability of zirconia-alumina composite coatings during hot corrosion test at 1050°C," *Journal of Alloys and Compounds*, vol. 506, no. 1, pp. 103–108, 2010.
- [12] R. Lach, K. Haberko, M. M. Bućko, M. Szumera, and G. Grabowski, "Ceramic matrix composites in the alumina/5-30vol.% YAG system," *Journal of the European Ceramic Society*, vol. 31, no. 10, pp. 1889–1895, 2011.
- [13] C. B. Reid, J. S. Forrester, H. J. Goodshaw, E. H. Kisi, and G. J. Suaning, "A study in the mechanical milling of alumina powder," *Ceramics International*, vol. 34, no. 6, pp. 1551–1556, 2008.
- [14] F. Mirjalili, M. Hasmaliza, and L. C. Abdullah, "Size-controlled synthesis of nano α -alumina particles through the sol-gel method," *Ceramics International*, vol. 36, no. 4, pp. 1253–1257, 2010.
- [15] R. Kavitha and V. Jayaram, "Deposition and characterization of alumina films produced by combustion flame pyrolysis," *Surface and Coatings Technology*, vol. 201, no. 6, pp. 2491–2499, 2006.
- [16] D. H. Trinh, M. Ottosson, M. Collin, I. Reineck, L. Hultman, and H. Högberg, "Nanocomposite Al_2O_3 - ZrO_2 thin films grown by reactive dual radio-frequency magnetron sputtering," *Thin Solid Films*, vol. 516, no. 15, pp. 4977–4982, 2008.
- [17] L. Qu, C. He, Y. Yang, Y. He, and Z. Liu, "Hydrothermal synthesis of alumina nanotubes templated by anionic surfactant," *Materials Letters*, vol. 59, no. 29-30, pp. 4034–4037, 2005.
- [18] K. Yatsui, T. Yukawa, C. Grigoriu, M. Hirai, and W. Jiang, "Synthesis of ultrafine γ - Al_2O_3 powders by pulsed laser ablation," *Journal of Nanoparticle Research*, vol. 2, no. 1, pp. 75–83, 2000.
- [19] A. Kruusing, *Handbook of Liquids-Assisted Laser Processing*, Elsevier, 2008.
- [20] Z. Yan, R. Bao, Y. Huang, and D. B. Chrisey, "Hollow particles formed on laser-induced bubbles by excimer laser ablation of Al in liquid," *Journal of Physical Chemistry C*, vol. 114, no. 26, pp. 11370–11374, 2010.
- [21] I. L. Liu, P. Shen, and S. Y. Chen, " H^+ - and Al^{2+} -codoped Al_2O_3 nanoparticles with spinel-type related structures by pulsed laser ablation in water," *Journal of Physical Chemistry C*, vol. 114, no. 17, pp. 7751–7757, 2010.
- [22] B. Kumar and R. K. Thareja, "Synthesis of nanoparticles in laser ablation of aluminum in liquid," *Journal of Applied Physics*, vol. 108, no. 6, Article ID 064906, 2010.
- [23] W. H. Gitzen, *Alumina as Ceramic Material*, special publication no. 4, American Ceramic Society, 1970.
- [24] H. Chang and Y. C. Chang, "Fabrication of Al_2O_3 nanofluid by a plasma arc nanoparticles synthesis system," *Journal of Materials Processing Technology*, vol. 207, no. 1–3, pp. 193–199, 2008.
- [25] V. S. Kortov, S. V. Nikiforov, I. I. Milman, and E. V. Moiseykin, "Specific features of luminescence of radiation-colored α - Al_2O_3 single crystals," *Radiation Measurements*, vol. 38, no. 4–6, pp. 451–454, 2004.
- [26] E. Stratakis, V. Zorba, M. Barberoglou, C. Fotakis, and G. A. Shafeev, "Femtosecond laser writing of nanostructures on bulk Al via its ablation in air and liquids," *Applied Surface Science*, vol. 255, no. 10, pp. 5346–5350, 2009.
- [27] G. Viau, V. Collière, L. M. Lacroix, and G. A. Shafeev, "Internal structure of Al hollow nanoparticles generated by laser ablation in liquid ethanol," *Chemical Physics Letters*, vol. 501, no. 4–6, pp. 419–422, 2011.
- [28] E. Stratakis, M. Barberoglou, C. Fotakis, G. Viau, C. Garcia, and G. A. Shafeev, "Generation of Al nanoparticles via ablation of bulk Al in liquids with short laser pulses," *Optics Express*, vol. 17, no. 15, pp. 12650–12659, 2009.